UNIVERSIDAD DE MÁLAGA

ESCUELA TÉCNICA SUPERIOR DE
INGENIERÍA DE TELECOMUNICACIÓN

TRABAJO FIN DE MÁSTER

DYNAMIC MODELING OF GNSS MULTIPATH ERROR FOR CIVIL AVIATION

MÁSTER EN INGENIERÍA DE
TELECOMUNICACIÓN

RAFAEL OLIVA GONZÁLEZ
MÁLAGA, 2023

This master thesis has been developed at the Institute of Communications and Navigation of the German Aerospace Center (DLR) in Munich, under the supervision of Omar García Crespillo.

Este trabajo fin de máster se ha desarrollado en el Instituto de Comunicaciones y Navegación del Centro Aeroespacial Alemán (DLR) en Munich, bajo la supervisión de Omar García Crespillo.

E.T.S. DE INGENIERÍA DE TELECOMUNICACIÓN, UNIVERSIDAD DE MÁLAGA

DYNAMIC MODELING OF GNSS MULTIPATH ERROR FOR CIVIL AVIATION

Author: Rafael Oliva González

Supervisor: Teresa María Martín Guerrero

Department: Communications Engineering

Degree: Master in Telecommunications Engineering

Keywords: Time-correlated error modeling, airborne multipath error, civil aviation.

Abstract

Ensuring safe GNSS localization is essential for critical transportation applications like civil aviation. In order to achieve that, the robust modeling of all GNSS errors is an essential step. Current minimum operational performance standards (MOPS) propose GNSS error models that are sufficient for snapshot positioning (like least squares). However, they do not address completely the stochastic dynamics of the errors over time. Moreover, current standards only provide GNSS error models for single-frequency single-constellation (i.e. GPS L1 band). Recent research has developed high-integrity time-correlated error models for GNSS tropospheric, orbit and satellite clock error sources. Nevertheless, the airborne multipath error has not yet been modeled with this approach.

In this work, we characterize the airborne multipath error for the GPS L1 and L5 bands, and the Galileo E1 and E5a bands using data from real test flights. In order to model multipath with a robust time-correlated error model, its behavior is studied over time through the properties of its autocorrelation function, as well as modeling it conservatively in the frequency domain. The resulting error models are suitable for implementations in safe time-sequential positioning estimators, such as the Kalman filter.

E.T.S. DE INGENIERÍA DE TELECOMUNICACIÓN, UNIVERSIDAD DE MÁLAGA

MODELADO DINÁMICO DEL ERROR MULTICAMINO EN GNSS PARA AVIACIÓN CIVIL

Autor: Rafael Oliva González

Tutor: Teresa María Martín Guerrero

Departamento: Ingeniería de Comunicaciones

Titulación: Máster en Ingeniería de Telecomunicación

Palabras clave: Modelado de errores correlados en el tiempo, error multicamino aéreo, aviación civil.

Resumen

Garantizar una localización segura con GNSS es esencial para aplicaciones de transporte críticas como aviación civil. Para lograrlo, el modelado robusto de todos los errores en las señales GNSS es fundamental. Los MOPS (Minimum Operational Performance Standards) actuales proponen modelos de error que son suficientes para estimadores de posición instantáneos (que no hacen uso de las medidas anteriores). No obstante, no abordan por completo la dinámica estocástica de los errores a lo largo del tiempo. Además, los estándares actuales solo proporcionan modelos de error GNSS para la banda L1 de GPS. Investigaciones recientes han desarrollado modelos de error de alta integridad correlados en el tiempo para diferentes fuentes de error GNSS, como el error troposférico, y el error orbital y de reloj del satélite. Sin embargo, el error multicamino aéreo aún no se ha modelado con esta metodología.

En este trabajo, caracterizamos el error multicamino aéreo para las bandas L1 y L5 de GPS, y las bandas E1 y E5a de Galileo utilizando datos recopilados en vuelos de prueba reales. Con el fin de modelar el multicamino con un modelo robusto de error correlado en el tiempo, estudiamos su comportamiento a lo largo del tiempo a través de las propiedades de su función de autocorrelación, además de modelarlo de forma conservadora en el dominio de la frecuencia. Los modelos de error resultantes son adecuados para su implementación en estimadores seguros de posicionamiento secuencial en el tiempo, como el filtro de Kalman.

To my grandmother Celia

Acknowledgements

I would like to extend my deepest gratitude to Omar García Crespillo, who supervised my work at DLR. This master thesis would not have been possible without his guidance and support. I appreciate all the time he dedicated to our long and fruitful discussions that helped me learn so much during these last 6 months. Furthermore, I am also thankful to my tutor from the University of Málaga, Teresa. Her insight and words of encouragement were invaluable since the beginning.

Special thanks to all the colleagues from my group: Anja, Patrick, Maximilian, Ana and Florian. They were always willing to help me and treated me as one more of the group. I would also like to acknowledge my fellow office colleagues: Lazar, Nikolas and Teodor. Our many conversations always made the office a pleasant environment to share and work together.

Additionally, I want to express my appreciation to Fede and Paco. Coming together from Málaga to Munich to work at DLR allowed us to share many special moments, and it was an experience I will never forget.

I am forever thankful to Maite for her patience and understanding. Her caring support helped me get trough the most difficult moments. Lastly, I am also extremely grateful to my family for their unwavering love, encouragement, and belief in my abilities. They have been a source of strength and motivation throughout this master thesis.

Contents

List of Figures

List of Tables

Acronyms

ACF	Autocorrelation Function
AGDV	Antenna Group Delay Variation
BF	Body frame
CMC	Code-Minus-Carrier
DFT	Discrete Fourier Transform
ECEF	Earth-Centered Earth-Fixed
FFT	Fast Fourier Transform
FOGMP	First Order Gauss Markov Process
GNSS	Global Navigation Satellite System
GPS	Global Positioning System
MAPE	Mean Absolute Percentage Error
MMR	Multi Modal Receiver
MOPS	Minimum Operational Performance Standards
NED	North East Down
PSD	Power Spectral Density
SV	Satellite Vehicle
WGN	White Gaussian Noise
WSS	Wide-Sense Stationary

Nomenclature

Constants

c	Speed of light in a vacuum

Multipath error models

σ_{mp}	Multipath standard deviation
σ_{noise}	Thermal noise standard deviation
σ_{mp}	Smoothed multipath standard deviation
$\sigma_{raw\ mp}$	Raw multipath standard deviation
T	Hatch Filter smoothing time constant

GNSS error sources

β	Instrumental error (carrier-phase)
δt	Clock bias
η	Thermal noise (carrier-phase)
λ	Wavelength
ϕ	Carrier-phase measurement
ρ	Code-phase measurement
ε	Thermal noise (code-phase)
ξ	Antenna error (code-phase)
ζ	Antenna error (carrier-phase)

b	Instrumental error (code-phase)
e	Ephemeris error
G	Geometric range
I	Ionospheric delay
MP	Multipath error (code-phase)
mp	Multipath error (carrier-phase)
N	Integer ambiguities
T	Tropospheric delay

Multipath isolation

CMC	Code-Minus-Carrier

Signal analysis

Δt	Sampling period
ℓ	Lag values
$\mathcal{N}$	Normal distribution
Ω	Discrete-time frequency
f	Frequency
f_s	Sampling frequency
L	Total number of samples
R_{xx}	Autocorrelation of signal x (continuous-time)
r_{xx}	Autocorrelation of signal x (discrete-time)
S_{xx}	Spectral density of signal x

First Order Gauss Markov Process

σ^2	FOGMP variance
τ	FOGMP time correlation constant

Coordinate transformation

$\boldsymbol{C}$	Rotation matrix
$\boldsymbol{u}$	Line of sight vector
ψ	Azimuth angle of the satellite
θ	Elevation angle of the satellite
lat	Latitude
$long$	Longitude
H	Heading angle (from the true north)
P	Pitch angle
R	Roll angle

1. Introduction

This chapter provides the general context of this master thesis, as well as the current technology gap that drives the purpose of this work. In addition, the proposed research objectives are introduced. Finally, a brief overview of the document structure is also presented.

1.1 Background

Over the last decades, Global Navigation Satellite Systems (GNSS) have become increasingly prevalent in many navigation and positioning applications. In the field of civil aviation, GNSS are especially predominant because they can potentially provide worldwide coverage as compared to other traditional navigation aids.

GNSS services for civil aviation are considered safety-critical applications where system integrity plays a crucial role. This includes developing accurate error models inherent to the GNSS measurements. For this reason, standardization bodies like the Radio Technical Commission for Aeronautics (RTCA) continuously release Minimum Operational Performance Standards (MOPS) that describe the error models for GNSS measurements.

Current available standards (MOPS) cover the use of single-constellation single-frequency receiver, in particular, the GPS L1 band. Error models for the GPS L1 band are generally obtained through cumulative distribution function (CDF) overbounding [1][2] and are sufficient for snap-shot positioning, which means that previous measurements are not used to compute the current user's position. However, they do not address completely the stochastic dynamics of the errors over time, making them not enough for safe time-sequential positioning estimators like the Kalman Filter.

1.2 Motivation

Recent research describes robust error modeling for time-correlated errors for the tropospheric error [3], as well as the orbit and satellite clock errors [4]. These type of models address the stochastic dynamics of the errors over time and are suitable to be implemented in a Kalman Filter. The Kalman filter can be a more accurate position estimator and allows the integration of additional sensors like an Inertial Measurement Unit (IMU) [5]. However, airborne multipath error in GNSS measurements has not yet been characterized using a high-integrity time-correlated model.

In this context, we set as the ultimate goal of this thesis to model the airborne multipath error in the code measurements with a dynamic error model using real data from several test flights. This data includes GNSS measurements from GPS L1 and L5 bands, and Galielo E1 and E5a bands. As an example. Figure 1.1 displays the direct GNSS signal with a green color. The orange and red lines represent the reflected GNSS signals, which cause the airborne multipath error.

Figure 1.1: Graphical representation of the airborne multipath error (DLR's ATRA test aircraft).

In the near future, multi-constellation multi-frequency receivers are expected to substitute current civil aviation receivers due to their many advantages over the single-constellation single-frequency receivers. The L5, E1 and E5a individually promise more accurate and reliable positioning than the L1 band. Additionally, the simultaneous use of different constellations and frequency bands provides more availability and the ability to correct the ionospheric error combining GNSS measurements from two frequency bands.

1.3 Objectives

The main two goals of this thesis are:

1. Develop a methodology to isolate the airborne multipath error from other GNSS error sources and characterize its temporal behavior.
2. Derive robust time-correlated error models for airborne multipath using real flight data.

1.4 Structure of the Thesis

This thesis is divided in 8 different chapters. Chapter 2 introduces basic GNSS notions and their application in civil aviation. Chapter 3 presents the theoretical statistical tools used in stochastic error modeling. Chapter 4 explains the methodology used to isolate multipath error from raw GNSS measurements. Chapter 5 describes the proposed methodology to analyze and model the multipath error. Chapter 6 introduces the flight data used to evaluate the methodology. The results of this thesis are presented and discussed in Chapter 7. Lastly, Chapter 8 summarizes the main achievements, final conclusions and possible next steps following this work.

Part I

Preliminaries

2. GNSS Navigation for Civil Aviation

This chapter reviews the fundamental theory about Global Navigation Satellite Systems (GNSS), together with the background knowledge regarding their usage in the civil aviation field. Later sections in this chapter offer insight into the GNSS error sources and their models, as well as some basic GNSS processing concepts. To conclude, Section 2.5 covers the different ways to model the airborne multipath error, also focusing on the current technology gap.

2.1 General GNSS Concepts

The term Global Navigation Satellite Systems (GNSS) encompasses four main constellation of satellites: Global Positioning System (United States), Galileo (European Union), BeiDou (China) and GLONNAS (Russia). The main goal of these technologies is to provide compatible devices the capability of estimating their positions by employing MEO (Medium Earth Orbit) satellites that orbit around the Earth. Currently, GNSS are the predominant navigation system and provide localization service for a wide range of positioning applications.

2.1.1 Principle of Use

In order to operate, satellites orbit around the Earth transmitting radio frequency signals that provide worldwide coverage. These signals contain information about the satellite position and the time the signal was sent, which is extremely precise due to fact that satellites use atomic clocks. Since the travel speed of electromagnetic waves through the atmosphere is, in principle, a known constant, the distance from the user to the satellite can be estimated if we also know the time the signal was received. Lastly, it is necessary that the user's receiver acquires simultaneously GNSS signals from at least four different satellites (from the same constellation). The reason for this is that a 4 equation system with 4 unknown variables needs to be solved to estimate the position of the user at a specific moment. Those four unknown variables are the spatial coordinates: x, y, z and the difference between the system time and the receiver time (clock-bias). Although solving the system of equations results in obtaining the user's position, there are error sources affecting these signals that we have not mentioned in this simplified explanation. Section 2.3 describes in detail the main errors inherent to GNSS measurements and the models associated with them.

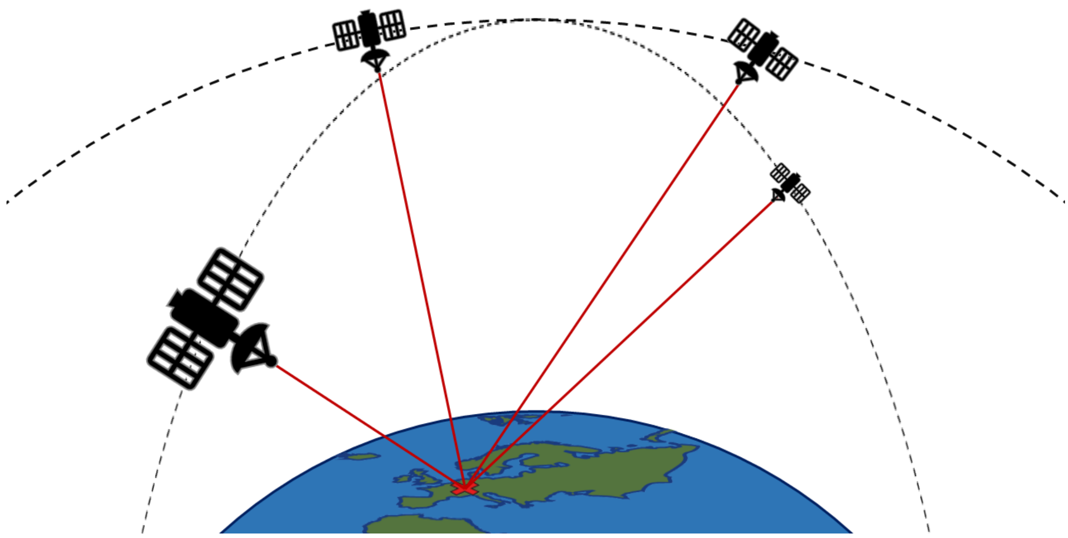

Figure 2.1: Basic positioning scenario with four satellites within line of sight of the user.

2.1.2 GNSS Structure

The GNSS structure is commonly divided into three different segments:

- **Space Segment**: it consists of a constellation of MEO satellites. These satellites transmit ranging signals on at least two frequencies within the microwave radio spectrum.
- **Control Segment**: its main goal is to maintain the system's health by monitoring the broadcast signals. It is also responsible for computing and uploading to the satellites the required navigation data. The control segment is composed of a group of dispersed monitoring stations that communicate with the satellites through ground antennas. The master control station has a backup facility at a different location.

- **User Segment**: It comprises GNSS receiving equipment for both civil and military services. These receivers can be found in ground, sea, air or even space applications [6].

2.1.3 GPS and Galileo Constellations

The main constellations supporting short term safety related applications are GPS and Galileo. In the next subsections, more information about them is provided.

GPS

Global Positioning System (GPS), which was developed by the United States of America, was the first GNSS constellation to be deployed and its first satellite launch was in 1978. GPS was originally designed to have 24 satellites evenly distributed among 6 orbital planes with an altitude of 20,180 km, which corresponds to a Medium Earth Orbit (MEO). Currently, it is composed of 31 operational satellites, also referred to as Space Vehicles (SVs). Their orbital period is 11 hours and 58 minutes, meaning each SV travels two complete orbits each sidereal day, repeating the same ground track each day.

GPS signals are transmitted on 3 radio frequencies on the L band: L1, L2 and L5 bands. The L5 band was added later than the first two with the launch of new satellite models (2010). All the signals have right-hand circular polarization, and their frequencies are derived through multiplying the fundamental frequency by an integer number. This fundamental frequency (f_0), which value is set at 10.23 MHz, is generated by atomic clocks onboard the SVs. Table 2.1 shows the carrier frequency for each band and its relation to the fundamental frequency.

It is also worth noting that Binary Phase Shift Keying (BPSK) is the modulation method used for all signals in every frequency band, except for the L1C signal, which uses Multiplexed Binary Offset Carrier (MBOC) [7]. Furthermore, GPS implements the Code-Division Multiple Access (CDMA) technique to send simultaneously multiple signals in the same frequency band. These signals are sequences of zeros and ones that allow the receiver to determine the time it took for the radio signal to travel from the SV to the user. They are referred to as ranging codes or Pseudo Random Noise (PRN) codes, and they are modulated over the carriers of the different bands. PRN codes can be classified in civilian and military access, the later one reserved for authorised users. Thus, only civilian codes are an open service (free of charge) used for civil navigation worldwide. The main civil ranging codes for the 3 frequency bands are the following: Coarse/Acquisition (C/A) and L1C (L1C-I data + L1C-Q pilot) for L1, L2C (L2 Civil Moderate + L2 Civil Long) for L2, and L5C (L5-I data + L5-Q pilot) for L5.

Band	Carrier frequency	Relation to f_0
L1	1575.420 MHz	154 $\times$ 10.23 MHz
L2	1227.600 MHz	120 $\times$ 10.23 MHz
L5	1176.450 MHz	115 $\times$ 10.23 MHz

Table 2.1: Carrier frequencies values for all the GPS bands and their relation to the fundamental frequency (f_0).

Lastly, the current 'legacy' Navigation Message (NAV) is modulated on the carriers at a rate of 50 bits per second. It contains all the necessary information to allow users to perform the positioning service: ephemeris and time parameters, ionospheric and clock corrections, the almanacs, etc. The complete message comprises 25 frames, each lasting for 30 seconds. Together they form what is known as the master frame. The entire master frame requires 12.5 minutes to be transmitted completely to the GNSS receiver. This modulation of all signals also includes repeating periodically every sequence of bits, which is known as a chipping. For instance, in the C/A code, each sequence contains 1023 bits and is repeated every millisecond. This means the duration of a chip is 1 μs, in other words, a chipping rate of 1.023 Mcps.

Galileo

Galileo's first test satellite was launched in 2005, however, it was not until 2016 that the system became operational. Galileo was developed by the European Space Agency (ESA) and one of its main goals was to eliminate the dependency of European authorities to foreign GNSS technologies, specifically, GPS or GLONASS. Unlike GPS, Galileo has 3 orbital planes with an altitude of 23,222 km, also in the MEO range. As of August of 2023, there are 36 SVs in orbit, of which only 28 are operational. Their orbital period is 14 hours and 5 min.

Galileo was designed to provide different services depending on the user needs:

- **OS**: The Open Service is accessible to users worldwide without any cost. Single frequency receivers provide performance levels that are comparable to those of GPS (C/A). In the future, the OS is expected to provide Navigation Message Authentication, which will allow the computation of the user position using authenticated data extracted from the navigation message.

- **OSNMA**: The Open Service Navigation Message Authentication is a free access service complementing the OS. It delivers authenticated data, assuring users that the received Galileo navigation message has not been modified externally.

- **HAS**: The High Accuracy Service complementing the OS by providing an additional navigation signal and added-value services in a different frequency band. The HAS signal can be encrypted in order to control the access to the Galileo HAS services.

- **PRS**: The Public Regulated Service is intended for security authorities, such as police and military, who rely on a continuous service with controlled access. This service is encrypted and subject to strict governmental control.

- **SAR**: This service provides support to the international COSPAS-SARSAT system for Search and Rescue (SAR). Distress signals will be relayed to the Rescue Coordination Centre and users will be informed that their situation was acknowledged.

- **CAS**: The Commercial Authentication Service complements the OS by delivering controlled access and authentication functionality to users.

Similar to GPS, all satellites in the Galileo constellation utilize the same frequencies for transmitting signals (also differentiated using CDMA) [8]. They all consist of two types of channels: data channels and pilot channels. Both provide ranging codes, but the data channels also have navigation data. On the other hand, pilot channels are data-less signals without bit transitions, which facilitates the tracking of weak signals. Each channel is destined to provide one or more of the services mentioned earlier. They are distributed among 4 different frequency bands: E1, E5a, E5b and E6. Table 2.2 [9] describes the main characteristics of Galileo signals: carrier frequency, channel type, provided service, and modulation. It is also important to mention that MBOC modulation, used for the E1-B and E1-C signals, is implemented the Composite Binary Offset Carrier (CBOC) [10].

Galileo navigation messages are divided in four types: Freely accessible Navigation Message (F/NAV), Integrity Navigation Message (I/NAV), the Commercial Navigation Message (C/NAV) and the Governmental Navigation Message (G/-NAV). They provide information similar to GPS, however, these navigation message types are included or not depending on the channel type. These different channels are divided in five categories: Navigation/Positioning, Integrity, Supplementary, Public Regulated and Search and Rescue.

Band	Carrier frequency	Channel	Modulation	Services
E1	1575.420 MHz	E1-A data	BOC(15,2.5)	PRS
		E1-B data	MBOC(6,1,1/11)	OS, CS, SoL
		E1-C pilot		
E5a	1278.750 MHz	E5a-I data	BPSK(10)	OS
		E5a-Q pilot		
E5b	1176.450 MHz	E5b-I data	BPSK(10)	OS, CS, SoL
		E5b-Q pilot		
E6	1207.104 MHz	E6-A data	BOC(10,15)	PRS
		E6-B data	BPSK(5)	CS
		E6-C pilot		

Table 2.2: Main characteristics of Galileo signals.

2.2 Civil Aviation Navigation

There are multiple ground-based technologies that provide positioning support for aviation: Instrument Landing System (ILS), Very high frequency Omnirange Station (VOR), Distance Measuring Equipment (DME), etc. Nonetheless, since they are stationary equipment, they have a limited range. This range can vary from few kilometers (ILS) to 370 km (VOR/DME). On the other hand, GNSS can provide navigation support to aircrafts nearly anywhere on Earth. For this reason, GNSS are considered the predominant positioning systems in civil aviation, especially in situations where the airplane is outside of the effective range of ground-based technologies.

Only the frequency bands corresponding to the GPS L1/Galileo E1 and GPS L5/Galileo E5a are reserved Aeronautical Radio Navigation Service (ARNS) bands. However, as it was mentioned before, the Galileo constellation and the GPS L5 band became operative several years after GPS L1 and L2 bands. Because of that, the majority of the research effort in the last decades has been focused on characterizing and modeling the L1 band. Therefore, standardization bodies have developed only MOPS for single-frequency, single-constellation (L1 band). These organizations include: the International Civil Aviation Organization (ICAO), the Federal Aviation Administration (FAA) or European Organisation for Civil Aviation Equipment (EUROCAE).

The simultaneous use of different frequency bands provides improved accuracy, availability, and resilience to signal interference, as well as the ability to correct the ionospheric error. In addition, the L5 band from GPS together with the E1 and E5a bands from Galileo individually promise more accurate and reliable positioning estimation for civil aviation than the L1 band. For these reasons, recent research [2] has contributed in the release of standards involving L5, E1 and E5a signals. This also help manufacturers adjust their new products to the current standards and also provide their input. As of today, commercial airplanes are equipped with single-frequency GPS receivers for the L1 band. However, in the near future is expected that multi-frequency receiver models, like the Multi-Modal Receiver (MMR), will substitute current single-frequency receivers, making available the signals from all four bands: L1, L5, E1 and E5a.

In this type of research, oriented to standardization, error modeling plays a crucial role since it allows to define the integrity of the system. In this context, integrity can be described as the ability of one system to warn the user in case that displayed information cannot be trusted due to errors. For that, it is important to accurately characterize the errors involved, to later assess their effect on the resulting estimation of the position. Section 2.3 and Section 2.5 cover in detail the current error models for GNSS measurements, especially for the airborne multipath error, which is the focus of this thesis.

2.3 GNSS Error Sources and Models

In the previous section, we briefly discussed the role of modeling errors affecting GNSS measurements. In this section, we describe the error sources and associated models of GNSS measurements.

2.3.1 GNSS Measurements

The GNSS measurements, obtained by any receiver after correlation, are composed of: the code-phase (also referred to as the pseudorange), and the carrier-phase, and doppler. This last one will not be utilized in the context of this work.

- **Code-phase (ρ)**: the code-phase is simply the raw measurement of a satellite-specific ranging code, which was described previously. It is a binary signal that provides coarse timing information, allowing to estimate the pseudorange. However, it is more significantly more noisy than the carrier-phase.

- **Carrier-phase (ϕ)**: as its name implies, the carrier-phase is the measurement of the carrier signal that the ranging code is modulated over. It is considerable less noisy than the code-phase but it does not provide an accurate estimation of the pseudorange.

An example of real L1 band code-phase measurements can be seen in Figure 2.2.

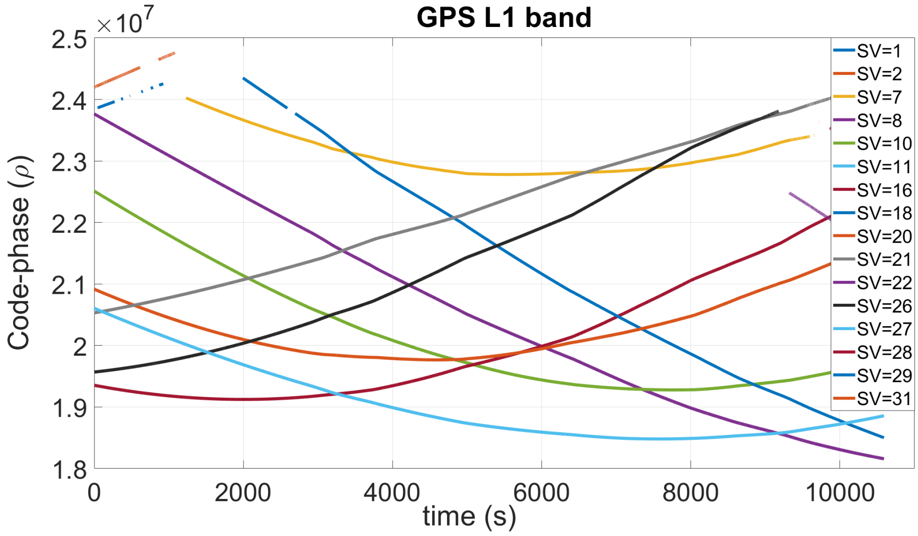

Figure 2.2: Example of a receiver code-phase measurement (in meters) for several GPS satellites in the L1 band.

Code-phase and carrier-phase are typically modeled with the following expressions for a specific frequency i, receiver r and satellite s [11]:

$$\rho^s_{r,i} = G^s_{r,i} + c \cdot (\delta t_r - \delta t^s) + T^s_{r,i} + I^s_{r,i} + e^s_{r,i} + MP^s_{r,i} + \varepsilon^s_{r,i} + b^s_{r,i} + b_{r,i} + \xi_{r,i} + \xi^s_{r,i} \,, \quad (2.1)$$

$$\phi^s_{r,i} = G^s_{r,i} + c \cdot (\delta t_r - \delta t^s) + T^s_{r,i} - I^s_{r,i} + e^s_{r,i} + mp^s_{r,i} + \eta^s_{r,i} + \beta^s_{r,i} + \beta_{r,i} + \zeta_{r,i} + \zeta^s_{r,i} + N^s_{r,i} \cdot \lambda_i \,, \quad (2.2)$$

where $\rho^s_{r,i}$ and $\phi^s_{r,i}$ are the pseudorange and carrier-phase measurement, respectively, $G^s_{r,i}$ represents the geometric range, which is the actual distance from the receiver to the satellite in meters. The term c indicates the speed of light in m/s, and in combination with $c \cdot (\delta t_r - \delta t^s)$ represents the error in meters due to the clock biases of both the satellite and the receiver. All of the error sources in Equations (2.1) and (2.2), as well as their nomenclature are described in the following table:

Nomenclature	Error source	Unit
δt_r	Receiver clock bias	s
δt^s	Satellite clock bias	s
$T^s_{r,i}$	Tropospheric delay	m
$I^s_{r,i}$	Ionospheric delay	m
$e^s_{r,i}$	Ephemeris error	m
$MP^s_{r,i}$ / $mp^s_{r,i}$	Multipath error (code/phase)	m
$\varepsilon^s_{r,i}$ / $\eta^s_{r,i}$	Thermal noise (code/phase)	m
$b^s_{r,i}$ / $\beta^s_{r,i}$	Satellite instrumental errors (code/phase)	m
$b_{r,i}$ / $\beta_{r,i}$	Receiver instrumental errors (code/phase)	m
$\xi^s_{r,i}$ / $\zeta^s_{r,i}$	Satellite antenna errors (code/phase)	m
$\xi_{r,i}$ / $\zeta_{r,i}$	Receiver antenna errors (code/phase)	m
$N^s_{r,i}$	Integer ambiguities	$cycles$

Table 2.3: Error sources terms in the code and carrier phase measurements.

As we can see in Equations (2.1) and (2.2), the tropospheric delay, the ionospheric delay and the ephemeris error impact both measurements in equal magnitude. However, the ionospheric delay affects with different sign in each expression.

2.3.2 Integer Ambiguities

In the context of the carrier-phase measurement, it is essential to understand the meaning of the "integer ambiguities" error term. It refers to the discrepancy between the real number of wave cycles the signal has experienced while traveling and the number of cycles the receiver's has estimated. As shown in Equation

(2.2), it can be represented as an unknown integer number $N^s_{r,i}$ times the wavelength of the signal λ_i.

Although this error can easily reach several hundred meters, in a normal case it is also constant over a continuous tracking of a satellite. It is important to keep this in mind for Section 4.5 in the Methodology part.

2.4 GNSS Processing

This section is dedicated to present two specific concepts that apply when processing GNSS signals. We will first explain what cycle-slips are and how the affect carrier-phase measurements, as well as their relation to integer ambiguities. Lastly, the carrier-smoothing method will also be described, which is used to reduce the code-phase measurement noise.

2.4.1 Cycle-Slips

A cycle-slip occurs when the receiver's PLL skips one or several phase cycles. This causes discontinuities in the carrier-phase measurement that are seen as jumps of integer numbers of wavelengths (λ_i). In other words, the integer ambiguities can no longer be considered constant. As it was mentioned earlier, this aspect will be relevant in Section 4.5.

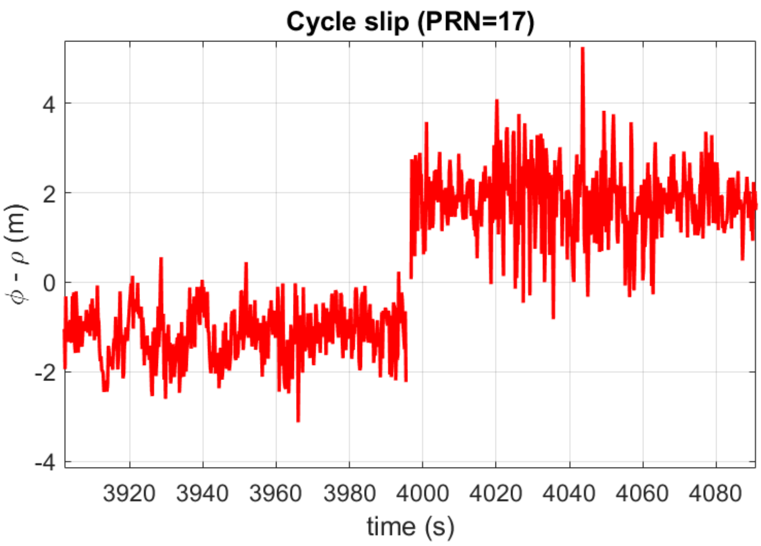

Figure 2.3: Example of a cycle slip around 4000 seconds on GPS satellite 17 (L1 band).

It is also worth noting that cycle-slips are not the same as simple loss of signal, which can be easily detected by the lack of measurement in a given moment. There are different cycle-slip detector implementations that decide what measurements are affected by a cycle-slip. Section 4.2.2 in the Methodology part describes in detail the cycle-slip detector algorithm chosen and its implementation.

2.4.2 Carrier-Smoothing

The noisy yet unambiguous code-phase measurements can be effectively improved and smoothed by combining it with the precise yet ambiguous carrier-phase measurements. This reduces significantly the noise and errors present the in the code-phase measurement. To achieve that, an algorithm denominated the Hatch filter, first introduced in [12], can be used. For a given satellite, frequency, code-phase (ρ) and carrier-phase (ϕ) measurements, the algorithm can be expressed as follows:

$$\overline{\rho}(k) = \begin{cases} \frac{1}{n}\rho(k) + \frac{n-1}{n}\left[\overline{\rho}(k-1) + (\phi(k) - \phi(k-1))\right] & \text{for } n \leq L \ , \\ \\ \frac{1}{L}\rho(k) + \frac{L-1}{L}\left[\overline{\rho}(k-1) + (\phi(k) - \phi(k-1))\right] & \text{for } n \geq L \ , \end{cases} \tag{2.3}$$

where k represents the current epoch number and n represents the number of epochs computed so far. On the other hand, $L = \frac{\mathrm{T}}{\Delta t}$ is a fixed value given by the sampling interval of the data (Δt) in seconds and the smoothing time constant (T) also in seconds. The smoothing time constant dictates the length of time it takes the filter to enter its steady state (to converge). Additionally, the algorithm must be initialised to $\overline{\rho}(k) = \rho(k)$ at the start and every time a loss of signal or a carrier-phase cycle slip occurs.

The carrier-smoothing is commonly applied when processing the code-phase at the user's end because it greatly reduces the noise impact. However, it is important to highlight two of its main disadvantages.

First, the models for smoothed measurements are only valid for when the filter has converged, in other words, when at least T seconds have passed. Paired with the fact that the algorithm restarts for every discontinuity, it can be especially detrimental. Secondly, the Hatch filter can resemble a low pass filter in the frequency domain. This results in the higher frequencies components of the errors being eliminated in the process, which means that the smoothed pseudorange needs to be modeled differently than the measurements without smoothing.

2.5 Current Multipath Error Models

To conclude this chapter, we will explain the current airborne multipath error models. These include the 100s smoothed multipath error model for the L1 band in the current MOPS, as well as recent research regarding high-integrity time-correlated errors.

2.5.1 MOPS Multipath Model

It was mentioned before that contemporary aircrafts are still equipped with single frequency receivers only capable of acquiring signals from the GPS L1 band. Consequently, error models present in the current standards have covered the L1 band in greater detail than other frequency bands. The most relevant multipath error model included in the current MOPS can be found in [1][13][14], and it models multipath error together with the receiver antenna errors, but separately from its thermal noise for the GPS L1 100 second smoothed code-phase measurements. For context, the equivalent to these error terms before the smoothing are theoretically expressed as $MP^s_{r,i}$, $\xi_{r,i}$ and $\varepsilon^s_{r,i}$ respectively in Equation (2.1). This GPS L1 MOPS error model parametrises both of them as zero-mean Gaussian overbounds, and their variance is described as follows:

$$\sigma^2_{\text{air}} = \sigma^2_{\text{noise}}(\theta) + \sigma^2_{\text{mp}}(\theta) \ , \tag{2.4}$$

where θ represents the elevation angle of an specific satellite with respect to the horizon from the aircraft's position, also known as North East Down (NED) frame. The distribution of these parameters' standard deviation is given for two performance classes of receiver/antenna combinations, Airborne Accuracy Designator A and B (AAD-A/AAD-B):

$$\sigma_{\text{noise}}(\theta) = \begin{cases} 0.15 + 0.43 \cdot exp\left(-\frac{\theta}{6.9}\right) & \text{for AAD-A} \ , \\ \\ 0.11 + 0.13 \cdot exp\left(-\frac{\theta}{6.9}\right) & \text{for AAD-B} \ , \end{cases} \tag{2.5}$$

$$\sigma_{\text{mp}}(\theta) = 0.13 + 0.53 \cdot exp\left(-\frac{\theta}{10}\right) \quad \text{for AAD-A and B} \ . \tag{2.6}$$

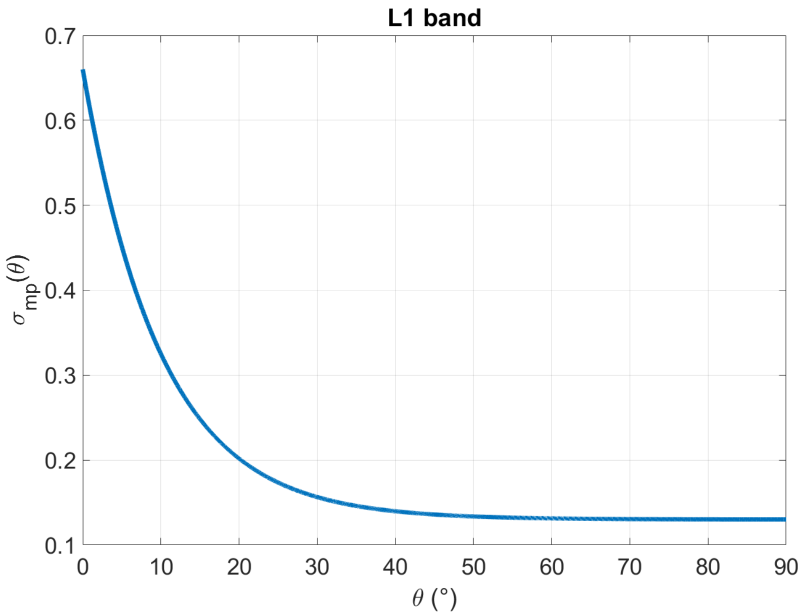

Figure 2.4: Current MOPS model for the standard deviation of 100s smoothed multipath error in the GPS L1 band (Equation (2.6)).

This model was established based on measurements collected during hundreds of flight hours from different airframes. It bounds the errors in the range domain for the worst combination of errors on all measurements, ensuring conservative bounding in the positioning domain. This is sufficient for snapshot positioning, which refers to the real-time estimation of the position being computed for each epoch without taking into account any previous measurements. However, they do not address completely the stochastic dynamics of the error sources. For this purpose, recent research has focused on developing dynamic error models that characterize the stochastic of different error sources over time. The last subsection explains these type of error models.

2.5.2 Multifrequency Multipath Models

Recent work [2] characterized the standard deviation (σ_{mp}) of 100-s smoothed multipath for multiple frequencies and GPS/Galileo constellations [2]. Multipath is modeled together with the thermal noise and the receiver antenna error is removed. This model was derived through the overbounding of the Cumulative Distribution Function (CDF) for the GPS L1 and L5 bands and Galileo E1 and E5 bands. The result of the model can be described in the following equation [2]:

$$\sigma_{mp}(\theta) = \begin{cases} 0.14 + 0.07 \cdot exp\left(-\frac{\theta}{40}\right) & \text{for L1/E1 ,} \\ \\ 0.11 + 0.05 \cdot exp\left(-\frac{\theta}{30}\right) & \text{for L5/E5a ,} \end{cases} \tag{2.7}$$

where $\theta \in [0°, 90°]$ is the elevation of the satellite with respect to the NED frame. For better comprehension, Equation (2.7) is also represented graphically in Figure 2.5.

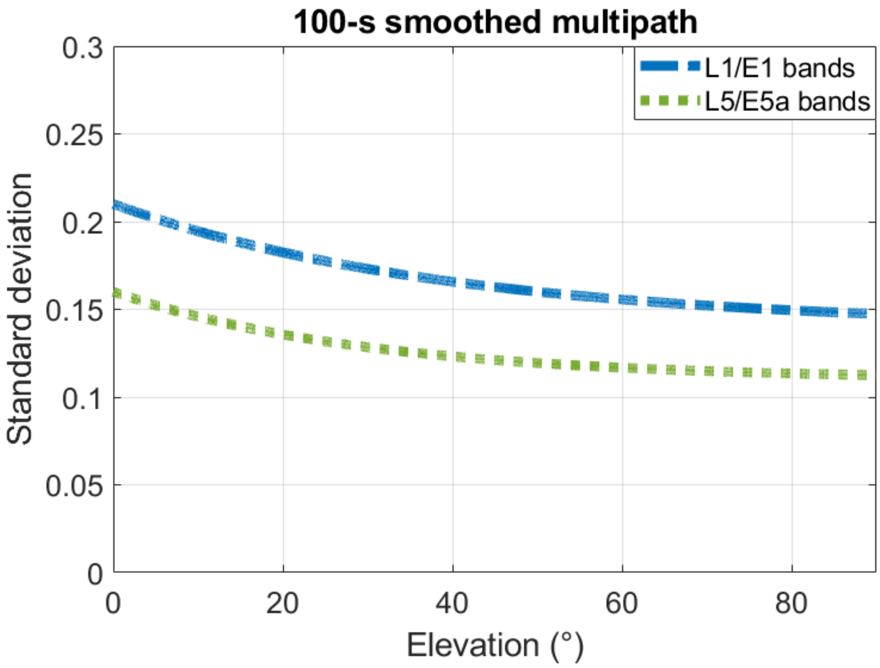

Figure 2.5: Standard deviation of 100-s smoothed multipath depending on the elevation (NED frame) for GPS and Galileo civil aviation bands according as described in Equation (2.7).

2.5.3 Dynamic Error Models

High-integrity time-correlated error models aim not only to safely bound the probability distribution of errors, but also to describe the stochastic dynamics of the errors. These error models are suitable for implementations in safe time-sequential positioning estimators, such as the Kalman filter, which is widely used in aeronautical applications. They are based on overbounding in the frequency domain the Power Spectral Density (PSD) of the error. It is proven in [15] that doing so ensures also bounding in the position domain if the PSD is obtained applying the Wiener–Khinchin–Einstein theorem. This theorem states that the PSD of a wide-sense-stationary random process can be estimated by calculating the Fourier Transform of its autocorrelation.

Recent work has characterized the Tropospheric error [3], as well as the Orbit and Clock error [4] using high-integrity time-correlated error models. However, the airborne multipath error has not yet been covered with this approach. Current MOPS [1] only provide a reference value of 25 seconds for the correlation time of multipath (without smoothing) in the GPS L1 band. It implies that if multipath error was to be modeled using a First Order Gauss Markov Process overbound, this reference value of 25 s would be its time-correlation constant (τ). In this context, we set as the goal of this thesis to model the multipath with a high-integrity time-correlated error model.

3. Stochastic Error Modeling

This chapter introduces different statistical tools and models that are commonly used to characterize time series. These include: the Autocorrelation Function, the Power Spectral Density and the First Order Gauss-Markov Process.

3.1 Autocorrelation Function

The autocorrelation is a statistical measure used to quantify the similarity between a time series and a delayed version of itself. The specific values of this delay are known as lags. It is a fundamental concept in time series analysis that helps us understand the degree of dependence or correlation between observations at different time points. The AutoCorrelation Function (ACF) of a continuous-time signal $x(t)$ can be defined as:

$$R_{xx}(t, \ell) = \int_{-\infty}^{\infty} x(t+\ell)x^*(t)\, dt \ , \tag{3.1}$$

where ℓ represents the lag, and $x^*(t)$ is the complex conjugate of $x(t)$.

A Wide-Sense-Stationary (WSS) random process is required to have a mean and autocorrelation function which only depend on the difference between the two instants being evaluated (ℓ). Another requirement is that the second moment of the process is finite for all times. In the case $x(t)$ can be considered a WSS random process, its ACF could be written as [16]:

$$R_{xx}(\ell) = \int_{-\infty}^{\infty} x(t+\ell)x^*(t)\, dt \ , \tag{3.2}$$

Since empirical data is discrete and finite, our ability is confined to estimating the autocorrelation sequence, which is the discrete version of the ACF. Two autocorrelation estimators are widely used: biased and unbiased, both of which are consistent. In the case of the unbiased version of the ACF, the variance can significantly increase for higher order lags. On the contrary, the biased estimator introduces statistical bias, but it has relatively lower variance. Because of this, the biased ACF is more commonly used for obtaining further estimations (like the Power Spectral Density). That being said, the biased estimation of the ACF for a discrete-time (k) WSS random process $x[k]$ can be expressed as follows:

$$\hat{r}_{xx}[\ell] = \frac{1}{L} \sum_{k=1}^{L} x[k+\ell] x^*[k] \ , \tag{3.3}$$

where ℓ is the temporal lag or delay and L is the number of available samples of the random process. Theoretically, ℓ is defined in the interval $[-\infty, \infty]$, however, it is more practical to limit its interval to $\ell \in [-L, L]$.

3.2 Power Spectral Density

The Power Spectral Density is the distribution of power contained in a signal across its different frequency components. There are several ways to estimate it: periodogram [17], Bartlett's method [18], Welch's method [19], etc. However, this subsection only focuses on the estimation through the Wiener-Khinchin-Einstein theorem. The reason for this is that, in the context of the Kalman Filter, it can be proven that overbounding the PSD of an WSS error in the frequency domain applying the Wiener-Khinchin-Einstein theorem guarantees that the error is bounded in the position domain [3]. Therefore, for the purpose of this thesis we only use this method to estimate the PSD of the multipath error.

The Wiener-Khinchin-Einstein theorem states that if a random process is WSS, its autocorrelation function and its Power Spectral Density (PSD) are Fourier pairs. This means that the spectral density of the random process $x(t)$, which is WSS and time-continuous, can be obtained performing the Fourier Transform to its autocorrelation function:

$$S_{xx}(f) = \int_{-\infty}^{\infty} R_{xx}(\ell) e^{-2\pi j f \ell} \, d\ell \ , \tag{3.4}$$

where once again ℓ represents the temporal lag or delay used to obtain the ACF, and f is the frequency in hertzs. Conversely, the autocorrelation function could also be obtained by performing the Inverse Fourier Transform to the spectral density:

$$R_{xx}(\ell) = \int_{-\infty}^{\infty} S_{xx}(f) e^{2\pi j f \ell} \, df \ . \tag{3.5}$$

For the discrete-time case, the PSD of the WSS random process $x[k]$ is similarly obtained applying the Discrete Fourier Transform to its ACF sequence:

$$S_{xx}(\Omega) = \frac{1}{2\pi} \sum_{n=-\infty}^{\infty} r_{xx}[n] e^{-j\Omega n} \ , \tag{3.6}$$

with the discrete-time frequency $\Omega = 2\pi \frac{f}{f_s}$ defined in $[-\pi, \pi]$ due to the periodic nature of the DFT and the Nyquist-Shannon sampling theorem. The term f represents the discrete frequency in Hz and f_s the sampling frequency (also in Hz) used to sample $x[k]$.

There are also some aspects that need to be taken into account when estimating the PSD of real signals. Among the most important ones we find aliasing and spectral leakage. Aliasing can occur when the signal has higher frequency components than the sampling frequency (fixed in some cases), causing in the overlapping of the discrete spectrum. On the other hand, spectral leakage takes place when non-periodic signal is transformed using the DFT. Since the DFT is periodic in the frequency domain, it implicitly assumes that the signal is also periodic in the time domain. This repetition introduces discontinuities at the beginning and end of the signal, which result in sharp transitions. In the frequency domain, these sharp transitions lead to the spreading of energy across neighboring frequency bins [20].

To solve both problems, a windowing is applied to the ACF before performing the DFT [21]. Windowing progressively reduces the value of the signal close to the beginning and end in the time domain, avoiding overlap of the higher frequency components, as well as smoothing the sharp transitions that cause spectral leakage. However, the main drawback of applying a window is that the original signal, to which we want to estimate the PSD, is being slightly altered.

For this work, we have chosen the Hamming window function. It is widely used, simple to implement and according to [21] it is one of the window functions with least spectral leakage. The following expression corresponds to the Hamming window in the discrete time-domain:

$$w[k] = 0.54 - 0.46 \cos\left(2\pi \frac{k}{L}\right) \ , \tag{3.7}$$

where L is the number of samples of the signal we want to apply the window to. Figure 3.1 shows the behavior of the Hamming window in the time domain.

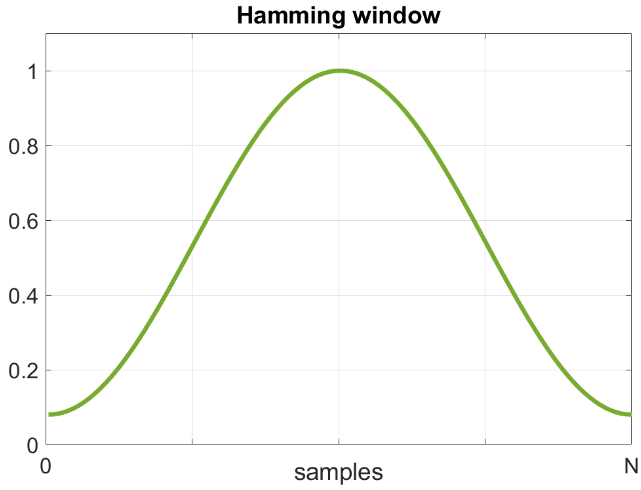

Figure 3.1: Hamming window function for a signal with L samples.

Thus, the final expression derived from Equation (3.6) we will use to estimate the PSD in W/Hz can be written as:

$$\hat{S}_{xx}(f) = \frac{1}{f_s} \sum_{n=-\infty}^{\infty} \left(r_{xx}[n] \cdot w[n]\right) e^{-2\pi j \frac{f}{f_s} n} \,, \tag{3.8}$$

Note that Equation (3.8) is normalized with respect to the sampling frequency f_s. Since the magnitude being represented is power density (W/Hz) in the frequency domain, this ensures it is divided by the interval in which it was obtained.

3.3 First Order Gauss-Markov Process

For snapshot positioning estimators, the pseudorange overbounding models are based on Gaussian distributions due to its simplicity and unique properties [22]. On the other hand, when deriving conservative time-correlated models for bounding empirical errors, the first order Gauss-Markov model can be considered an extension of the Gaussian model for time-correlated process [15].

The First Order Gauss-Markov Process (FOGMP), also known as Ornstein-Uhlenbeck process, is a type of stochastic process widely used in various fields because of its similar characteristics to real physical error processes. It has relatively simple theoretical expression, since it can be defined with just two parameters: its variance and time-correlation constant. In addition, the FOGMPs are stationary processes, meaning it is simpler to manipulate them mathematically. Thus, FOGMPs can be easily implemented in safe time-sequential positioning estimators, such as the Kalman Filter via state-augmentation [23][24].

The theoretical relation used to describe a continuous-time FOGMP $g(t)$, with a variance σ^2 and a time-correlation constant τ, can be written as:

$$\frac{\partial g(t)}{\partial t} = \frac{1}{\tau} g(t) + u(t) \ , \tag{3.9}$$

where $u(t)$ represents a continuous zero-mean White Gaussian Noise (WGN) with variance $\sigma_u^2 = \frac{2\sigma^2}{\tau}$.

The autocorrelation function of a generic FOGMP can also be expressed as follows:

$$R_{gg}(\ell) = \sigma^2 e^{-\frac{|\ell|}{\tau}} \ , \tag{3.10}$$

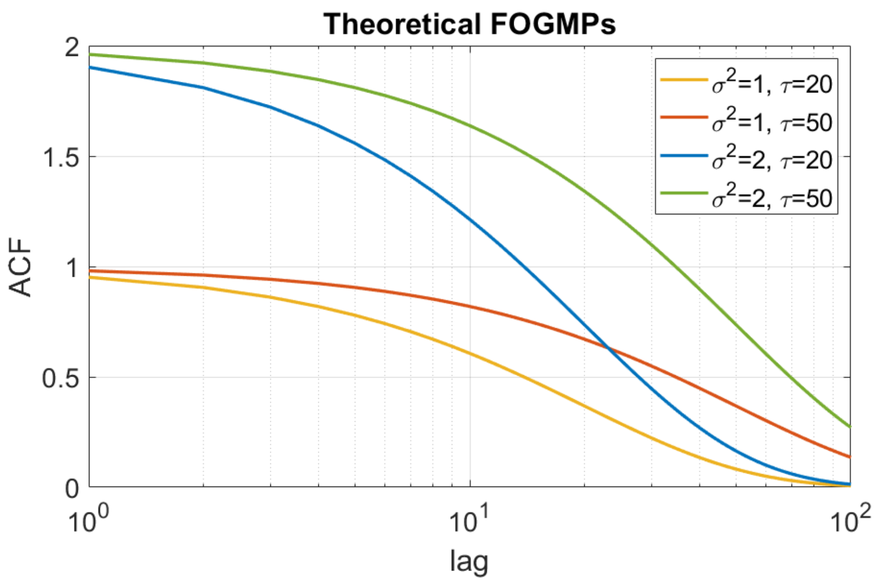

Figure 3.2: Autocorrelation function depending on the lag (ℓ) for different continous-time theoretical FOGMPs (Equation (3.10)).

Figure 3.2 shows the Autocorrelation Function (ACF) of several simulated FOGMPs. As we can see, it provides an intuitive representation of the degree of correlation of the process over time. Nonetheless, using the overbounding the ACF of an error process does not guarantee that the error is also bounded in the position domain. However, as we stated earlier, it can be proven that only by overbounding its Power Spectral Density (PSD) in the frequency domain, the WSS error process is guaranteed to be bounded in the position domain as well [3][25].

On the other hand, real data is always subject to a sampling frequency (f_s), and therefore, discrete. Due to this, we are more interested in the discrete expressions describing a FOGMP. Applying standard continuous to discrete transformations [26], we can obtain the discrete-time FOGMP expression:

$$g[k] = e^{-\frac{\Delta t}{\tau}} g[k-1] + u[k] \ , \tag{3.11}$$

where $\Delta t = \frac{1}{f_s}$ is the sampling time and $u[k]$ is also a WGN, but now discrete and with a variance $\sigma_u^2 = \sigma^2 \left(1 - e^{-\frac{2\Delta t}{\tau}}\right)$. If we rewrite Equation (3.11) we can obtain a more intuitive expression as:

$$g[k] = \alpha \cdot g[k-1] + \sqrt{\sigma^2(1-\alpha^2)} \cdot u_n[k] \ , \tag{3.12}$$

where $\alpha = e^{-\frac{\Delta t}{\tau}}$ and $u_n \sim \mathcal{N}(0,1)$.

Using the Wiener-Khinchin-Einstein theorem reflected in Equation (3.6), the PSD of a discrete-time FOGMP can be obtained with the next Equation:

$$S_{gg}(\Omega) = \frac{1}{2\pi} \sum_{n=-\infty}^{\infty} r_{gg}[n] e^{-j\Omega n} \ , \tag{3.13}$$

with the discrete angular frequency Ω defined once again only in $[-\pi, \pi]$. The theoretical expression of the power spectral density of a discrete-time FOGMP when its number of samples tends to infinity can be obtained [27] and expressed as:

$$S_{gg}(\Omega) = \frac{1}{\pi} \cdot \frac{\sigma^2(1-\alpha^2)}{1+\alpha^2 - 2\alpha\cos(\Omega\Delta t)} \ , \tag{3.14}$$

with $\Omega \in \left[0, \frac{\pi}{\Delta t}\right]$.

Note that the term $\frac{1}{\pi} = \frac{\cancel{2}}{\cancel{2}\pi}$ in Equation (3.14) is accomplishing two things. First, it conserves the total power of the FOGMP since only the positive half of its symmetrical spectrum is being considered. Secondly, it is normalizing the expression with the frequency interval in which it was originally defined.

If we take into account that the sampling interval is the inverse of the sampling frequency ($\frac{1}{\Delta t} = f_s$). Equation (3.14) can be written in terms of frequency (Hz), and not angular frequency (rad/s) as:

$$S_{gg}(f) = 2\,\Delta t \cdot \frac{\sigma^2(1-\alpha^2)}{1+\alpha^2-2\alpha\cos(2\pi f\Delta t)}\ , \tag{3.15}$$

where $f \in \left[0, \frac{f_s}{2}\right]$.

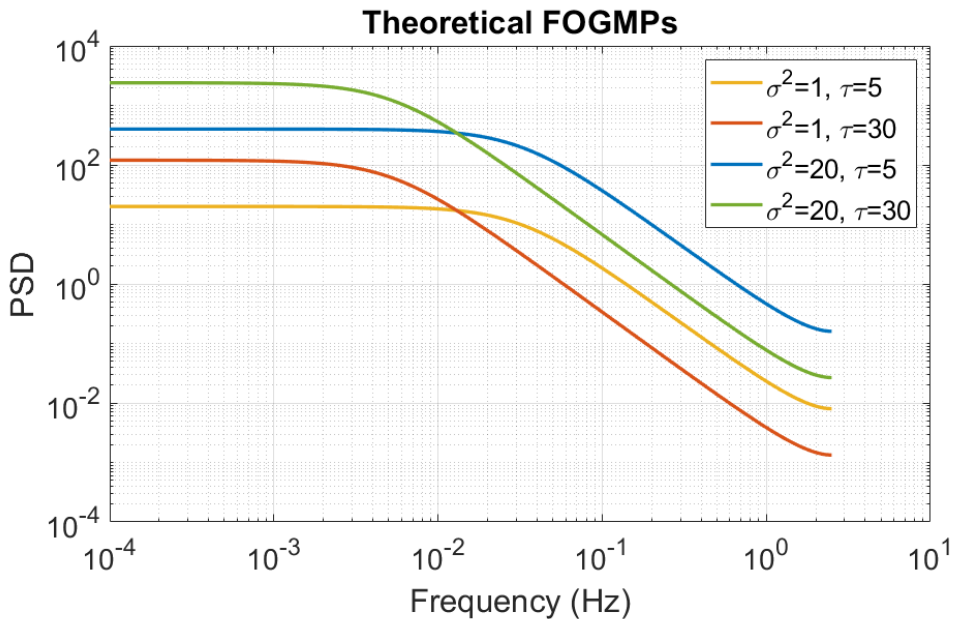

Figure 3.3: Power Spectral Density for different discrete-time theoretical FOGMPs with $\Delta t = 0.2\ s$.

Figure 3.3 shows the PSD behavior of several theoretical FOGMPs in the discrete-time domain. It represents graphically Equation (3.15) with $\Delta t = 0.2\ s$, which means it is only defined until $\frac{f_s}{2} = 2.5\ Hz$. As we can see σ^2 only affects the initial value. Meanwhile, τ affects both the initial value and the beginning of the slope portion. The bigger the value of τ is, the sooner this slope takes place. However, in a logarithmic scale for both axis, the value of this slope is always the same and therefore unaffected by any parameter.

Equation (3.15) can also be obtained when the number of samples of the FOGMP is not considered to tend to infinite. It can be written as follows [28]:

$$S_{gg}(f) = 2\,\sigma^2 \Delta t \cdot \textbf{\textit{Re}} \left(\frac{L-(L-1)Z+Z^{L+1}}{L(1-Z)^2} - 1 \right) \,, \tag{3.16}$$

where $Z = exp\left(-\frac{\Delta t}{\tau} - j2\pi f\right)$ and L is the number of samples of the FOGMP.

The difference between Equation (3.15) and Equation (3.16) can be seen in the next Figure 3.4. For convenience we will referred to this expressions as theoretical infinite FOGMP and theoretical finite FOGMP respectively.

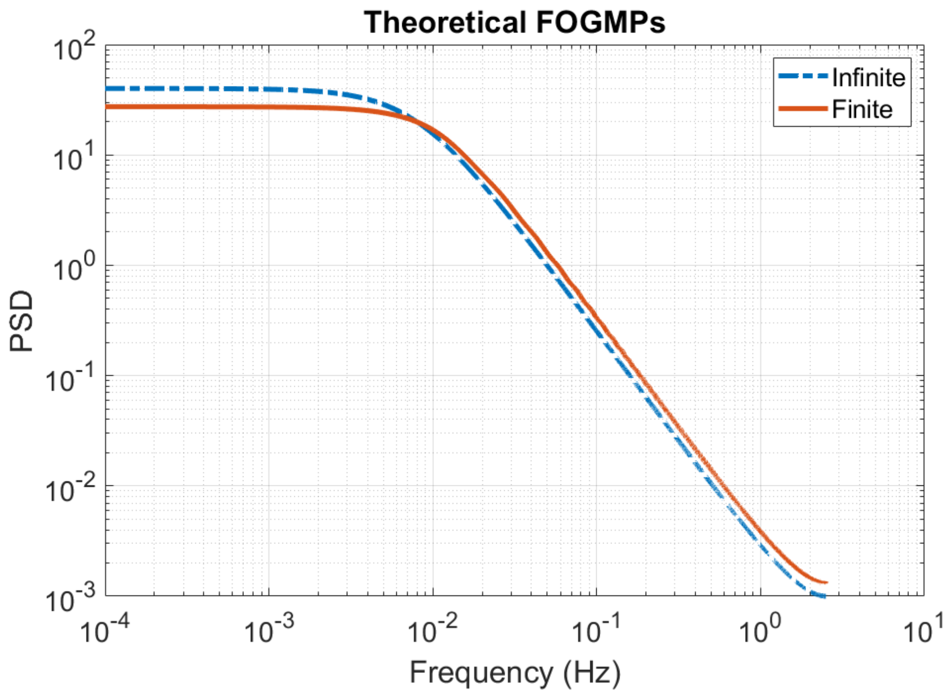

Figure 3.4: Difference between infinite and finite ($L = 300$) theoretical expressions for a FOGMP.

In order to plot Figure 3.4, the chosen parameters of both FOGMPs are: $\sigma^2 = 0.5$, $\tau = 20\ s$ and $\Delta t = 0.2\ s$. In the case of the theoretical finite FOGMP, the number of samples (L) is set to 300. It is important to mention that the theoretical infinite FOGMP will be used when referring to the overbounding function. Meanwhile, the finite FOGMP will be used exclusively in next section to compare it with a simulated FOGMP.

3.4 PSD Estimate Considerations

Lastly, we have also considered relevant to determine the effect of not having enough samples to accurately estimate the PSD of the real signal. Failing to recognize that a segment of data is too short for this purpose will result in an erroneous PSD being included in the modeling process. Figure 3.5 intuitively represents an example of this effect when estimating the PSD (applying the Equation (3.8)) a simulated FOGMP of length $L = 10000$, $\Delta t = 0.2$, $\sigma^2 = 1$ and $\tau = 20s$. For comparison, the PSD estimate is also calculated for the same data segment while only using the first $50\% \times L$ samples, $20\% \times L$ samples, etc. In this case, it is clear that using any less than the first $20\% \times L$ samples leads to an inaccurate estimation of the PSD, where the segment of data is too short, to the point that the effect of the Hamming window becomes more prevalent that the signal itself.

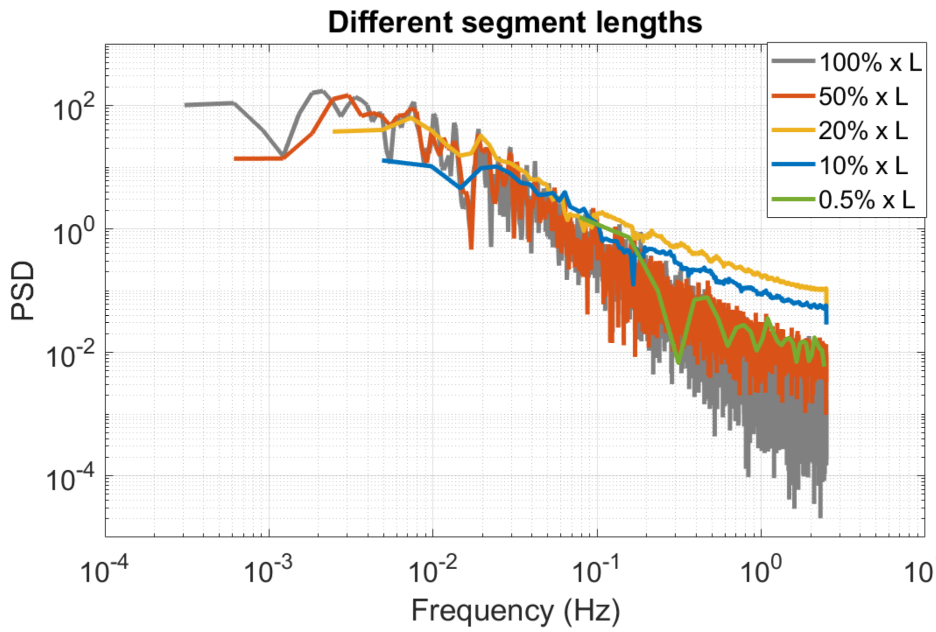

Figure 3.5: PSD of simulated FOGMP when using its first P% x L samples.

Now, in order to more rigorously assess this effect on the PSD estimate, a parametric simulation is performed. The idea is to compare the PSDs of both the theoretical finite FOGMP and a generated FOGMP through a Monte-Carlo simulation, which consists on averaging the PSDs of one thousand FOGMPs. We decided to use the Mean Absolute Percentage Error (MAPE) to measure the error between them because we believe it gives a more intuitive metric than that of the Mean Squared Error (MSE), for example. To obtain Figure 3.6, $\sigma^2 = 1$ and

$\Delta t = 0.2$ were set as fixed values for both the theoretical finite FOGMP and the simulated FOGMP, while their time-correlation constants and number of samples took a range of values.

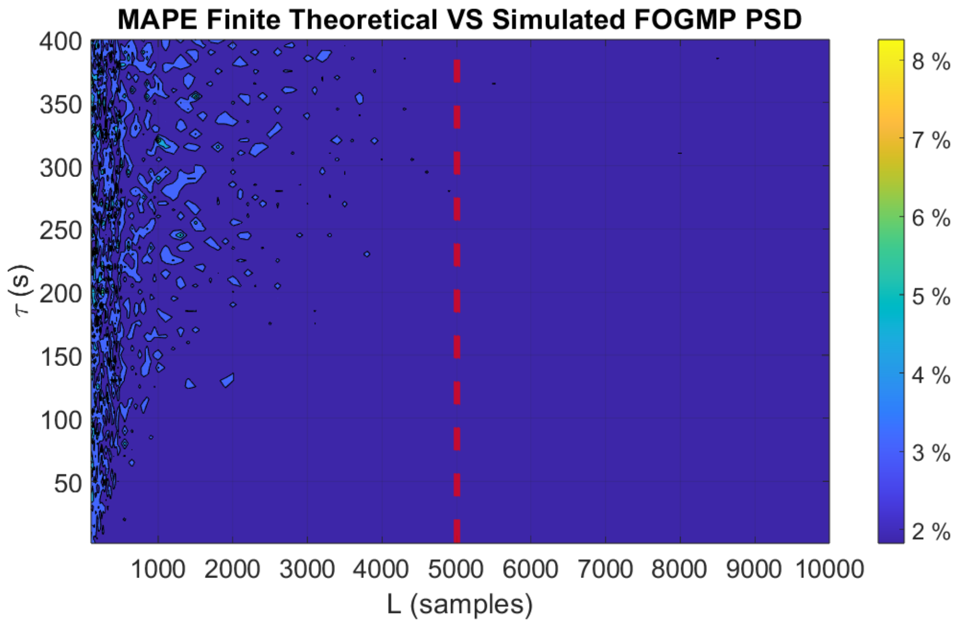

Figure 3.6: MAPE of the theoretical finite FOGMP vs Monte-Carlo simulated FOGMP.

As we can see, using 5000 samples for the Monte-Carlo simulated FOGMP guarantees the error to be at the minimum achievable value 2% for all values of τ.

Part II

Methodology

4. Multipath Isolation

Chapter 2 presented the expressions that describe the GNSS measurements. Looking at them, we can see that airborne multipath is one of the error sources that impact GNSS. However, it is not possible to directly model it, since we first need to define what we will consider as multipath and determine the procedure to isolate it from the rest of the errors.

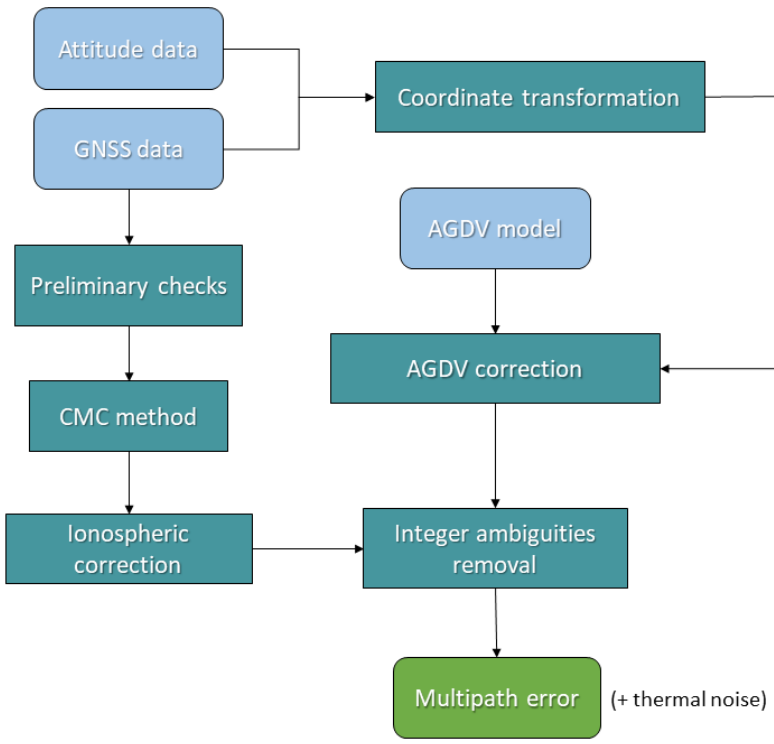

Figure 4.1: Conceptual diagram of the multipath isolation process.

This chapter describes the methodology to isolate multipath from other GNSS error sources. An overview of the methodology can be seen in Figure 4.1. The following sections explain each of the main processes depicted in the diagram: Preliminary Checks, Code-Minus-Carrier Method, Antenna Group Delay Variation (AGDV) correction and Integer Ambiguities Removal.

4.1 Multipath Definition

As we already mentioned before, there are several different approaches to model multipath error. This thesis models the multipath ($MP^s_{r,i}$) together with the thermal noise ($\varepsilon^s_{r,i}$), but excluding the receiver antenna error ($\xi_{r,i}$). With this in mind, we proceed to describe in detail the isolation methodology we used.

4.2 Preliminary Checks

Prior to processing the data, faulty measurements need to be discarded. These can be caused by cycle-slips or when the data is simply corrupted. Falling to discard them will result in an erroneous model. This section describes the two techniques used to detect and avoid these type of incorrect measurements.

4.2.1 Sanity Check

It is important to ensure the data is healthy and it does not contain incorrect GNSS measurements. One example of corrupt data are negative values of pseudorange. Since distances must always be positive, these measurements should be discarded. Another example of incorrect data are time jumps. These are discontinuities in the vector containing the timestamp each of the measurements. For instance, if the sampling interval is 0.2 seconds and the difference between two consecutive timestamps is 0.4 seconds, it can be assumed that one measurement was lost. In this case, we consider each time jump to split the data into two continuous segments.

4.2.2 Cycle-Slip Detector

As it was explained earlier in Section 2.4.1, when a cycle-slips occurs, the value of the integer ambiguities changes. Since the method to compensate integer ambiguities relies on them being constant over continuous tracking of a satellite, it is important to consider every measurement associated to a cycle-slip as a discontinuity. In the case of MATLAB, this can be achieved by simply changing that specific value to NaN (Not a Number), which is the same value used when no measurement was received in a certain epoch (timestamp). However, first we need to determine what measurements are affected by cycle-slips through a cycle-slip detector. There are several methods to implement a cycle-slip detector. In our case, we decided to use the single frequency cycle-slip detector described in [9]. The reason for this is that we were obtaining better results than with the double frequency one, which is more sensitive and sometimes yields false positives. This can be a disadvantage because it results in a significant reduction of the number of continuous long data segments, limiting the amount of useful data we can analyse.

The way this specific single frequency cycle-slip implementation works is by first calculating the difference between the carrier-phase and the code-phase. Then, a nth-degree polynomial fitting is done over a sliding window of L samples (e.g. $L = 200$ at 1 Hz). If at one specific epoch, the discrepancy between $(\phi - \rho)$ and the polynomial fit is higher than a pre-established threshold, that epoch is marked as a cycle slip. It is also important to note that this algorithm needs to be restarted every time a cycle slip is encountered.

4.3 Code-Minus-Carrier Method

Once the preliminary data checks are performed, we can begin the actual process to isolate the airborne multipath error. Our starting point are the Equations (2.1) and (2.2) used currently to describe raw GNSS measurements and that are here repeated for convenience:

$$\rho^s_{r,i} = G^s_{r,i} + c \cdot (\delta t_r - \delta t^s) + T^s_{r,i} + I^s_{r,i} + e^s_{r,i} + MP^s_{r,i} + \varepsilon^s_{r,i} + b^s_{r,i} + b_{r,i} + \xi_{r,i} + \xi^s_{r,i} \ , \tag{2.1}$$

$$\phi^s_{r,i} = G^s_{r,i} + c \cdot (\delta t_r - \delta t^s) + T^s_{r,i} - I^s_{r,i} + e^s_{r,i} + mp^s_{r,i} + \eta^s_{r,i} + \beta^s_{r,i} + \beta_{r,i} + \zeta_{r,i} + \zeta^s_{r,i} + N^s_{r,i} \cdot \lambda_i \ . \tag{2.2}$$

The first step is to subtract the carrier-phase to the code-phase [29], which leads to the CMC (Code-Minus-Carrier) observable:

$$\begin{aligned} CMC^s_{r,i} =& \rho^s_{r,i} - \phi^s_{r,i} = \\ =& 2 \cdot I^s_{r,i} + \left(MP^s_{r,i} + \varepsilon^s_{r,i} + b^s_{r,i} + b_{r,i} + \xi_{r,i} + \xi^s_{r,i}\right) \\ & - \left(mp^s_{r,i} + \eta^s_{r,i} + \beta^s_{r,i} + \beta_{r,i} + \zeta_{r,i} + \zeta^s_{r,i} + N^s_{r,i} \cdot \lambda_i\right) \ . \end{aligned} \tag{4.1}$$

As we can see, several terms are canceled: the geometric range ($G^s_{r,i}$), the error due to clock biases ($c \cdot (\delta t_r - \delta t^s)$), the tropospheric delay ($T^s_{r,i}$), and the ephemeris error ($e^s_{r,i}$). Nevertheless, the ionospheric delay ($I^s_{r,i}$) is now doubled. It is possible to compensate it if we have at our disposal GNSS measurements from at least two different frequency bands (from the same constellation).

The following expression shows how the ionospheric delay can be estimated combining the dual-frequency carrier-phase measurements:

$$I^s_{r,i} = \tfrac{f_j^2}{f_i^2-f_j^2} \cdot \left(\phi^s_{r,i} - \phi^s_{r,j}\right) = \tfrac{f_j^2}{f_i^2-f_j^2} \cdot \left(N^s_{r,i} \cdot \lambda_i - N^s_{r,j} \cdot \lambda_j\right) - \tfrac{f_j^2}{f_i^2-f_j^2} \cdot \left(E_i - E_j\right) \ , \tag{4.2}$$

with

$$\begin{aligned} E_i - E_j = &\left(mp^s_{r,i} + \eta^s_{r,i} + \beta^s_{r,i} + \beta_{r,i} + \zeta_{r,i} + \zeta^s_{r,i}\right) \\ &- \left(mp^s_{r,j} + \eta^s_{r,j} + \beta^s_{r,j} + \beta_{r,j} + \zeta_{r,j} + \zeta^s_{r,j}\right) \ , \end{aligned} \tag{4.3}$$

where i stands for the main frequency band, to which we want to estimate ionospheric delay to, and j for the secondary band needed for that purpose. Additionally, f represents the carrier frequency used in that band (in Hz).

In Equation (4.3), the terms E_i and E_j encompass various errors inherent to the carrier-phase measurements. The difference between E_i and E_j can be considered negligible since these errors are orders of magnitude smaller than those of the code-phase measurements. Note that by using this ionospheric divergence estimation, we will also add the integer ambiguities difference of both frequency bands. This is not so critical if we take into account that they are constant over a continuous tracking of a satellite, and thus can be removed, as we will see later on.

Having estimated the ionospheric delay ($I^s_{r,i}$) from Equation (4.2), only remains to subtract it twice to Equation (4.1). This leads to the next expression, generally referred to as the $CMC\ Divergence\ Free$ or CMC_{DF}:

$$CMC_{DF^s_{r,i,j}} = CMC^s_{r,i} - 2 \cdot I^s_{r,i} = \rho^s_{r,i} - \phi^s_{r,i} - 2 \cdot I^s_{r,i} \ , \tag{4.4}$$

and expanding its terms we obtain:

$$\begin{aligned} CMC_{DF^s_{r,i,j}} = &\left(MP^s_{r,i} + \varepsilon^s_{r,i} + b^s_{r,i} + b_{r,i} + \xi_{r,i} + \xi^s_{r,i}\right) \\ &- \left(mp^s_{r,i} + \eta^s_{r,i} + \beta^s_{r,i} + \beta_{r,i} + \zeta_{r,i} + \zeta^s_{r,i} + N^s_{r,i} \cdot \lambda_i\right) \\ &- 2 \cdot \frac{f_j^2}{f_i^2 - f_j^2} \left[\left(N^s_{r,i} \cdot \lambda_i - N^s_{r,j} \cdot \lambda_j\right) - \underbrace{\left(E_i - E_j\right)}_{\approx\, 0}\right] \ . \end{aligned} \tag{4.5}$$

As we just mentioned, the majority of the carrier-phase related errors are several orders of magnitude smaller than the ones of the code-phase. For instance, the carrier-phase multipath ($mp^s_{r,i}$) and noise ($\eta^s_{r,i}$) have a typical value in the range of millimeters. Meanwhile, when it comes to the code-phase measurement, multipath error ($MP^s_{r,i}$) combined with thermal noise ($\varepsilon^s_{r,i}$) can reach up to several meters [9][30].

Therefore, the carrier-phase measurements multipath and noise can be considered negligible, as well as its receiver ($\zeta_{r,i}$) and satellite ($\zeta^s_{r,i}$) antenna errors, which are even smaller in magnitude. This approximation also includes ignoring the difference coming from the ionospheric delay estimation ($E_i - E_j$) in Equation (4.3). However, the integer ambiguities ($N^s_{r,i} \cdot \lambda_i$ and $N^s_{r,j} \cdot \lambda_j$) and the instrumental errors ($\beta^s_{r,i}$ and $\beta_{r,i}$) are an exception to that. On the one hand, the integer ambiguities cannot be ignored because they can have a magnitude of hundreds of meters. On the other hand, instrumental errors in the carrier-phase measurements could be considered negligible, but it is possible to easily compensate them. In Section 4.5, the process to remove both errors will be explained in detail.

Lastly, we will also ignore the satellite antenna error associated to the code-phase measurement ($\xi^s_{r,i}$). This error introduces group delays in the signal and recent work has demonstrated that it exhibits variations depending on the nadir angle [31]. Nevertheless, it is worth noting that this error term is considerably smaller in magnitude compared to both the multipath error and the errors introduced by the receiver antenna. For this reason, we decided to exclude it as well from the multipath definition.

After all these assumptions, Equation (4.5) can be rewritten as:

$$
\begin{aligned}
CMC_{DF^s_{r,i,j}} \approx & \left(MP^s_{r,i} + \varepsilon^s_{r,i} + b^s_{r,i} + b_{r,i} + \xi_{r,i}\right) - \left(\beta^s_{r,i} + \beta_{r,i} + N^s_{r,i} \cdot \lambda_i\right) \\
& - 2 \cdot \frac{f_j^2}{f_i^2 - f_j^2} - \left(N^s_{r,i} \cdot \lambda_i - N^s_{r,j} \cdot \lambda_j\right) \ .
\end{aligned} \tag{4.6}
$$

At this point, the remaining steps for isolating multipath and thermal noise are the removal of the receiver antenna errors and the integer ambiguities.

4.4 Antenna Group Delay Variation

In [32], it is shown that receiver antenna errors encompass differential group delay, phase center variation, gain, and cross-polarization isolation. However, group delay variation is the error that affects the code-phase measurements with the most severity, easily reaching values of few meters. In other words, that means that its magnitude is comparable to that of code multipath. Since our goal is to isolate it, correcting antenna group delay variation (AGDV) will have a big impact in the result of the multipath isolation.

In simple terms, AGDV can be defined as the difference in time delay each frequency component experiences while travelling through the receiver's antenna. This effect is caused by the non-linear frequency response of the antenna. Additionally, it is important to understand that this error is dependent on the elevation and azimuth angles of arrival of the signal.

The focus of this section is to describe the procedure to compensate the AGDV affecting the code measurement [2].

4.4.1 Coordinate Transformation

As we stated earlier, AGDV depends on the elevation and azimuth angle of arrival of the signal. For this reason, the first step for correcting this error is to obtain the value of both these angles. The methodology we follow in this section is described in [33].

Our starting point are the next input data: the aircraft's position, and the position of each satellite. Initially, these are given in the Earth Fixed Earth Centered (ECEF) coordinate system. Because we are only interested in the relative position between airplane and satellite, it is more convenient to work with a local navigation frame. Therefore, we will reduce the complexity of further calculations by transforming them to North East Down (NED) first.

We will start by calculating the Line of Sight column vector ($\boldsymbol{u}$) between the aircraft and every satellite involved, defined as:

$$\boldsymbol{u}_{\text{ECEF}} = \boldsymbol{s}_{\text{ECEF}} - \boldsymbol{r}_{\text{ECEF}} = \begin{bmatrix} x_{\boldsymbol{s}_{\text{ECEF}}} \\ y_{\boldsymbol{s}_{\text{ECEF}}} \\ z_{\boldsymbol{s}_{\text{ECEF}}} \end{bmatrix} - \begin{bmatrix} x_{\boldsymbol{r}_{\text{ECEF}}} \\ y_{\boldsymbol{r}_{\text{ECEF}}} \\ z_{\boldsymbol{r}_{\text{ECEF}}} \end{bmatrix} , \tag{4.7}$$

where s_{ECEF} is the position of a specific satellite and $\mathbf{r}_{\text{ECEF}}$ is the position of the aircraft's receiver, both in the ECEF coordinate frame. The receiver's position will be considered the coordinate origin in the NED system.

Next, we need to transform the $\boldsymbol{u}_{\text{ECEF}}$ column vector to the NED coordinate frame:

$$\boldsymbol{u}_{\text{NED}} = \begin{bmatrix} x_{\boldsymbol{u}_{\text{NED}}} \\ y_{\boldsymbol{u}_{\text{NED}}} \\ z_{\boldsymbol{u}_{\text{NED}}} \end{bmatrix} = \boldsymbol{C}_{\text{ECEF}}^{\text{NED}} \cdot \boldsymbol{u}_{\text{ECEF}} \ . \tag{4.8}$$

The transformation matrix $\boldsymbol{C}_{\text{ECEF}}^{\text{NED}}$ from ECEF coordinate frame to NED can be described as follows [33]:

$$\boldsymbol{C}_{\text{ECEF}}^{\text{NED}} = \begin{bmatrix} -\sin(lat)\cdot\cos(long) & -\sin(lat)\cdot\sin(long) & \cos(lat) \\ -\sin(long) & \cos(long) & 0 \\ -\cos(lat)\cdot\cos(lon) & -\cos(lat)\cdot\sin(long) & -\sin(lat) \end{bmatrix} , \tag{4.9}$$

where lat and $long$ refer to the latitude and the longitude of the aircraft, respectively.

In addition, we have to normalize $\boldsymbol{u}_{\text{NED}}$ to obtain the unitary Line of Sight vector $\hat{\boldsymbol{u}}_{\text{NED}}$:

$$\hat{\boldsymbol{u}}_{\text{NED}} = \frac{\boldsymbol{u}_{\text{NED}}}{|\boldsymbol{u}_{\text{NED}}|} \ . \tag{4.10}$$

At this point, we could already calculate the elevation and azimuth angles of the satellites with respect to the airplane's antenna. However, the NED coordinates always describe a plane parallel to the surface of the Earth. This means that any rotation that the aircraft performs when maneuvering will not be reflected in the NED coordinate frame. Consequently, the elevation and azimuth angles will be incorrect if we calculate them in the NED frame instead of the actual antenna frame.

For this reason, we decided to perform another coordinate transformation, which will take into account the aircraft's attitude. The concept of attitude is covered in detail in Appendix A. Regarding this transformation, it will allow us to obtain the real elevation and azimuth angles of each satellite with respect to the antenna (body frame), and not the NED frame. Figure 4.2 intuitively shows the difference in elevation between both coordinate systems.

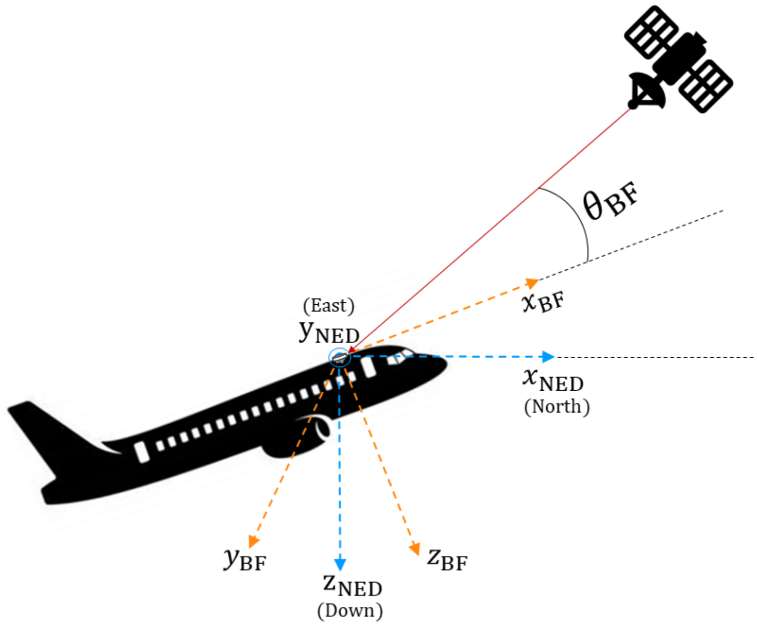

Figure 4.2: Example of the difference between the satellite elevation with respect to the antenna/body frame and the NED frame.

We proceed now to perform the coordinate transformation to the unitary LOS vector obtained in Equation (4.10):

$$\hat{\boldsymbol{u}}_{\text{BF}} = \begin{bmatrix} x_{\hat{\boldsymbol{u}}_{\text{BF}}} \\ y_{\hat{\boldsymbol{u}}_{\text{BF}}} \\ z_{\hat{\boldsymbol{u}}_{\text{BF}}} \end{bmatrix} = \boldsymbol{C}^{\text{BF}}_{\text{NED}} \cdot \hat{\boldsymbol{u}}_{\text{NED}} \ , \tag{4.11}$$

where the transformation matrix C^{BF}_{NED} from the NED coordinate system to the Body Frame (BF) is composed of 3 Euler rotations. Each of them referring to one attitude parameter: heading (H), pitch (P) and roll (R), as we can see in the following expression, also defined in [33]:

$$\boldsymbol{C}^{\text{BF}}_{\text{NED}} = \begin{bmatrix} 1 & 0 & 0 \\ 0 & \cos(\text{R}) & \sin(\text{R}) \\ 0 & -\sin(\text{R}) & \cos(\text{R}) \end{bmatrix} \cdot \begin{bmatrix} \cos(\text{P}) & 0 & -\sin(\text{P}) \\ 0 & 1 & 0 \\ \sin(\text{P}) & 0 & \cos(\text{P}) \end{bmatrix} \cdot \begin{bmatrix} \cos(\text{H}) & \sin(\text{H}) & 0 \\ -\sin(\text{H}) & \cos(\text{H}) & 0 \\ 0 & 0 & 1 \end{bmatrix} \ . \tag{4.12}$$

Finally, both the elevation (θ_{BF}) and azimuth (ψ_{BF}) angles of a specific satellite with respect to the antenna frame can be obtained through the next relation:

$$
\begin{aligned}
\theta_{\mathsf{BF}} &= \arctan\left(\frac{-z_{\hat{\boldsymbol{u}}_{\mathsf{BF}}}}{\sqrt{x^2_{\hat{\boldsymbol{u}}_{\mathsf{BF}}} + y^2_{\hat{\boldsymbol{u}}_{\mathsf{BF}}}}}\right) , \\
\psi_{\mathsf{BF}} &= \arctan\left(\frac{y_{\hat{\boldsymbol{u}}_{\mathsf{BF}}}}{x_{\hat{\boldsymbol{u}}_{\mathsf{BF}}}}\right) .
\end{aligned}
\tag{4.13}
$$

4.4.2 AGDV Model

The last step to correct the AGDV is to use a model of the aircraft's antenna. This model needs to characterize the direct effect of the AGDV error in the code-phase measurements. As we stated before, AGDV depends on the elevation and azimuth angles of arrival of the received signal. Because of this, we can simply input the result from Equation (4.13) in the antenna model to obtain the AGDV error affecting the code measurement for those specific values of elevation and azimuth. In the end, we subtract the estimated AGDV error, $\xi_{r,i}(\theta_{\mathsf{BF}}, \psi_{\mathsf{BF}})$, to the CMC_{DF} approximation in Equation (4.6). The resulting $CMC\ AGDV\ Corrected$ or CMC_{AC} can be expressed as follows:

$$
\begin{aligned}
CMC_{AC^s_{r,i,j}} =& CMC_{DF^s_{r,i,j}} - \xi_{r,i}(\theta_{\mathsf{BF}}, \psi_{\mathsf{BF}}) = \left(MP^s_{r,i} + \varepsilon^s_{r,i} + b^s_{r,i} + b_{r,i}\right) \\
&- \left(\beta^s_{r,i} + \beta_{r,i} + N^s_{r,i} \cdot \lambda_i\right) - 2 \cdot \frac{f_j^2}{f_i^2 - f_j^2} - \left(N^s_{r,i} \cdot \lambda_i - N^s_{r,j} \cdot \lambda_j\right) .
\end{aligned}
\tag{4.14}
$$

4.5 Integer Ambiguities Removal

After obtaining the expression in Equation (4.14), it only remains to eliminate the integer ambiguities and instrumental error terms present in it so as to isolate the multipath error together with the thermal noise.

Previously, it was mentioned that this integer ambiguities removal method relies on the instrumental errors and the integer ambiguities to be constant. Since both can be considered constant over a continuous tracking of a satellite, we can simply subtract its own mean. Nevertheless, a continuous tracking of a satellite by definition cannot contain any loss of lock or cycle-slip. For this reason, we first have to split the CMC_{AC} data into uninterrupted segments where those discontinuities are absent. Additionally, these segments need to be longer than a set parameter M, otherwise the estimated mean of that segment may not be representative. However, this leads to a trade-off, because the bigger M is, the harder it will be for continuous segments to qualify as longer than it. This in turn reduces the amount of data available to process and analyse.

Lastly, we want to emphasize that this approach assumes that the multipath error is a zero mean stochastic process, which holds true in most scenarios. Having said that, we can theoretically express this last step as follows:

$$CMC_{MP^s_{r,i,j}} = CMC_{ACs^s_{r,i,j}} - \frac{1}{K}\sum_{k=1}^{K} CMC_{AC^s_{r,i,j}} \,, \tag{4.15}$$

where only continuous segments of length $K \geq M$ are being computed. Furthermore, it can be proven that the remaining error terms in Equation 4.15 are:

$$CMC_{MP^s_{r,i,j}} = MP^s_{r,i} + \varepsilon^s_{r,i} \,. \tag{4.16}$$

After removing all the integer ambiguities terms and the instrumental errors associated to both code-phase and carrier-phase measurements, the CMC method is consummated. As a result, we have isolated the multipath error ($MP^s_{r,i}$) and the thermal noise ($\varepsilon^s_{r,i}$) inherent to the code measurement. From now on, when talking about modelling multipath we will be referring to $CMC_{MP^s_{r,i,j}}$ in Equation (4.16). Figure 4.3 shows an example of the isolated multipath's behavior in the time domain.

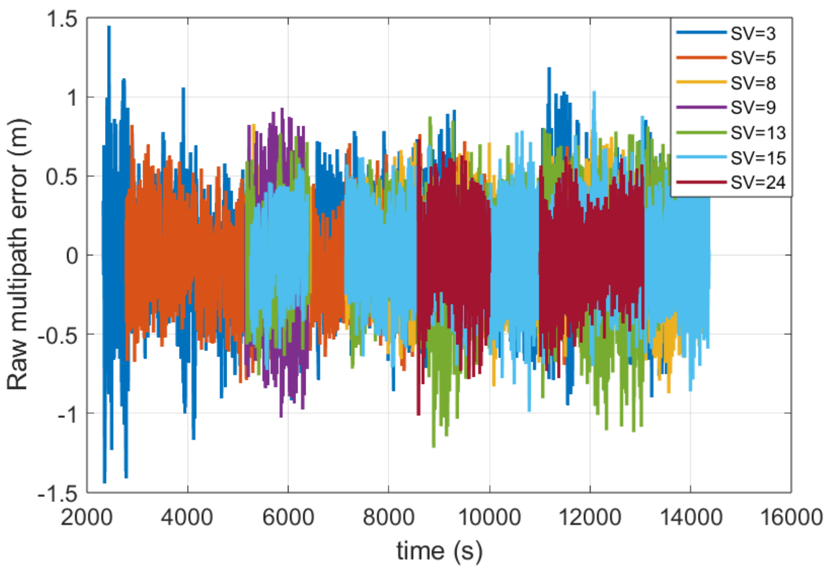

Figure 4.3: Example of Galileo E1 band isolated airborne multipath error from different satellites (Equation (4.16)).

5. Multipath Analysis and Modeling

After isolating the multipath from the rest of the errors in Chapter 4, the next step is to analyse the data and derive a high-integrity time-correlated error model. In order to achieve that, we have chosen a specific methodology consisting of several processes.

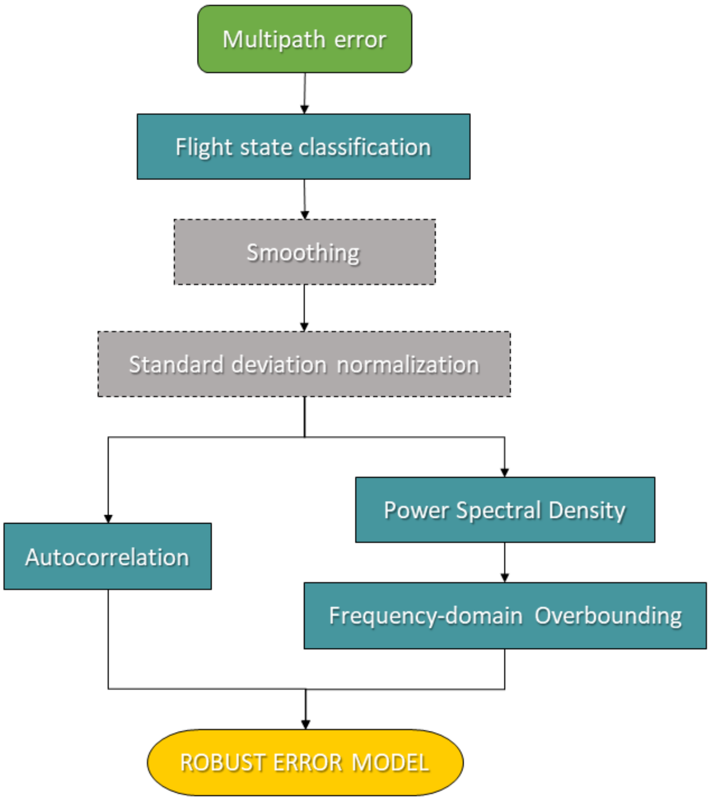

Figure 5.1: Conceptual diagram of the multipath analysis and modeling process.

Figure 5.1 displays the entire modeling process, as well as all the smaller processes that it can be divided into. As we can see, all the processes are represented with the same darker turquoise color. However, Smoothing and Standard Deviation Normalization have a grey color to indicate they can be independently included or not in the modeling process so as to obtain different multipath models. Table 5.1 shows all possible combinations resulting in four different multipath models, which will be applied to measurements from GPS's L1 and L5 band as well as Galileo's E1 and E5a bands. The reasoning behind their choice will be covered in detail in their respective sections.

Multipath processing options	
Unsmoothed Unnormalized	Unsmoothed Normalized
Smoothed Unnormalized	Smoothed Normalized

Table 5.1: Proposed options for processing mulipath error.

Another relevant aspect to consider is the non-stationary nature of the multipath error. As it was described previously in Chapter 3, the frequency domain overbounding of the error is a key step in the modeling process. However, it is proven that the error overbound in the position domain is only guaranteed if the error itself is WSS. For this reason, we have decided to include some processes in this methodology that aim to mitigate the non-stationary aspects of multipath: flight state classification and standard deviation normalization.

5.1 Flight State Classification

Since the data used in these thesis is obtained from real test flights, we have considered important to not include in the analysis parts of the flight where the aircraft is close to the ground. Not doing so would mean we would be including ground multipath in the modeling process, which has two main implications. On one hand, our goal is to model the airborne multipath error (and thermal noise), therefore not removing the effect of ground multipath would result in the incorrect modeling of it. On the other hand, ground multipath could worsen the already existent non-stationary nature of airborne multipath.

For these reasons, we have decided to exclude all flight data where the aircraft is below a certain altitude. The chosen minimum altitude threshold for this thesis is 3050 meters (10000 feet) since it is considered as the standard minimum altitude where a flight can stop the climbing phase and begin the cruise phase (where the majority of the flight will take place). We also performed sensitivity tests to confirm that slightly varying this parameter did not have much impact on the results. Consequently, all the flight data epochs will be classified in two possible states: cruise state (above threshold) and take-off/landing state (below threshold). We will only include data from the cruise state in the analysis and modeling. Figure 5.2 shows an example of the aircraft's altitude throughout one of the test flights in relation with the established altitude threshold of 3050 m.

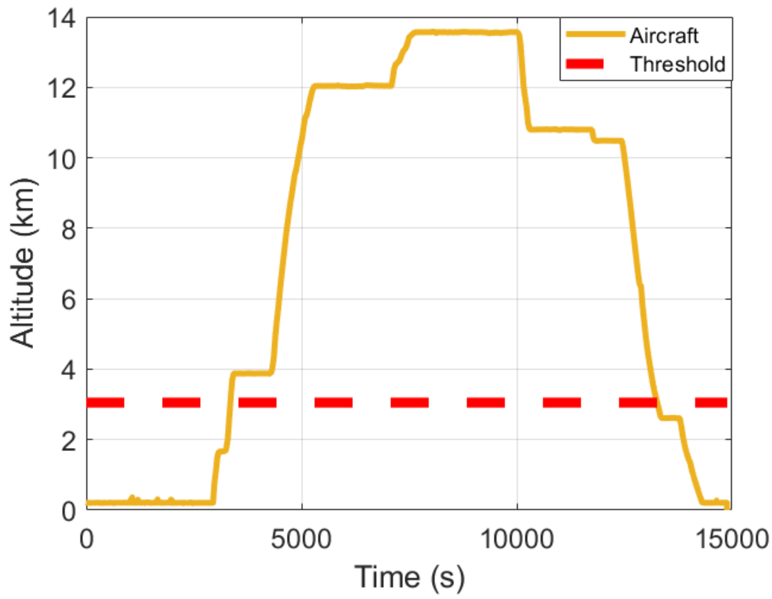

Figure 5.2: Aircraft's altitude in relation to the minimum altitude threshold (3050 m).

5.2 Smoothing

Aeronautical applications typically rely on carrier-smoothing to reduce the noise affecting code-phase measurements, which allows the end user to estimate their position more accurately. Hence, we decided to model not only the raw (unsmoothed) multipah, but also the smoothed multipath. Although the smoothing process eliminates high frequency components for both multipath and noise, which modifies some of its characteristics, it is useful to model its effect on the end user. Therefore, the smoothing will be a part of the modeling process only when characterizing smoothed multipath, both unnormalized and normalized as we will see in the next section.

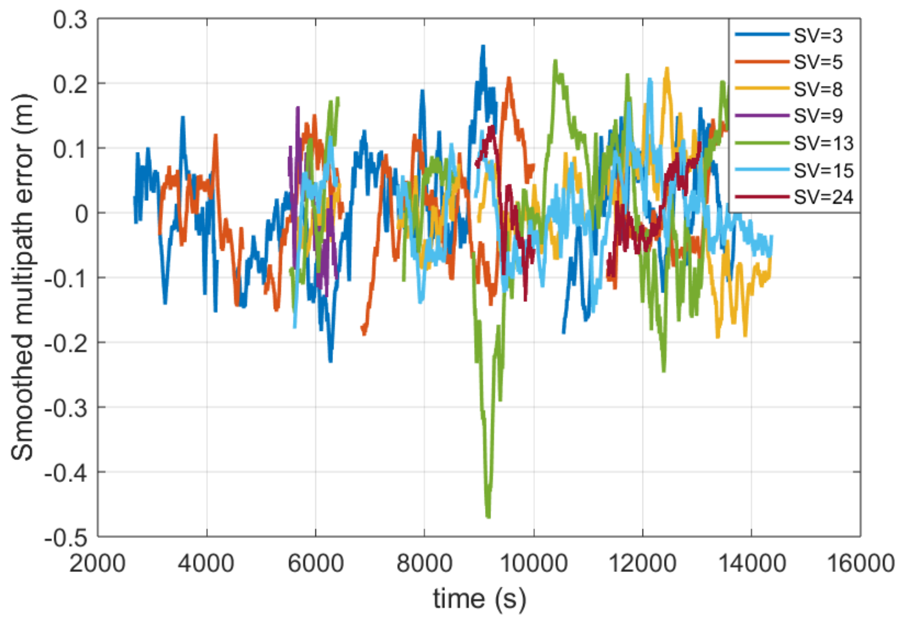

Figure 5.3: Example of Galileo E1 band 100-s carrier-smoothed multipath error from different satellites.

To perform the carrier-smoothing, a recursive averaging filter known as Hatch filter is applied to the measurements. For this purpose, we will use the variation of the Hatch Filter algorithm presented in Equation (5.1). It was adopted in the standards [13][14] and it is more convenient than the original Hatch filter algorithm because it is applied directly to the raw multipath from Equation (4.16) and not the code-phase. As a result, it is not necessary to process again all the data from the beginning when computing the smoothed multipath instead of the from raw multipath. The following expression describes the aforementioned variation of the Hatch filter algorithm:

$$\overline{CMC}(k) = \begin{cases} \frac{1}{n}CMC(k) + \frac{n-1}{n}\left[\overline{CMC}(k-1)\right] & \text{for } n \leq L\,, \\ \\ \frac{1}{L}CMC(k) + \frac{L-1}{L}\left[\overline{CMC}(k-1)\right] & \text{for } n \geq L\,, \end{cases} \tag{5.1}$$

where k represents the current epoch number and n represents the number of epochs computed so far. On the other hand, $L = \frac{\mathrm{T}}{\Delta t}$ is a fixed value given by the sampling interval of the data (Δt) in seconds and the smoothing time constant (T) also in seconds. The smoothing time constant dictates the length of time it takes the filter to enter its steady state (to converge). Additionally, the algorithm must be initialised to $\overline{CMC}(k) = CMC(k)$ at the start and every time a loss of signal or a carrier-phase cycle slip occurs. Figure 5.3 illustrates an example of the smoothed multipath's behavior in the time domain. For the sake of comparison, the raw (unsmoothed) multipath error from which this example of smoothed multipath was obtained can be found in Figure 4.3.

The larger T is, the more precise the smoothed pseudorange is. However, the ionospheric divergence effect between the code and carrier also increases with T [34]. In the case of this work, we have chosen the smoothing time constant T to be 100 seconds for two reasons. Firstly, the FAA reported 100 seconds as the LAAS recommendation value [35], which makes this value commonly employed. Secondly, this allows us to use the standard deviation model for 100-s smoothed multipath developed in [2], which was obtained using the same data as this thesis.

Finally, it is important to mention that the filter steady state is reached after 3.6 times the smoothing time constant [36]. Therefore, we will only analyze smoothed multipath after the filter has continuously processed data for 360 seconds.

5.3 Standard Deviation Normalization

It was mentioned earlier in this chapter that the airborne multipath error has an inherent non-stationary nature. Its main non-stationary aspect is the fact that multipath's standard deviation is dependent on the satellite elevation angle. More specifically, the lower the angle of elevation of the satellite is, the higher its standard deviation is. For this purpose, the elevation of the satellite is generally computed with respect to the horizon (NED frame). This allows to capture the influence of carrier-to-noise ratio $\left(\frac{C}{N_0}\right)$ which directly affects the thermal noise, and therefore, our model. Since the elevation in the NED frame is directly proportional to the distance from the satellite to the user, the carrier-to-noise ratio will decrease the lower the elevation angle is.

On the other hand, the multipath error is dependent on the angle of arrival with respect to the aircraft's body frame and not with respect to the NED frame. However, most of the time commercial aircrafts fly straight and level, which means the satellite elevation is very similar with respect to the body frame and with respect to the NED frame. Taking both aspects into account, is generally considered more relevant to capture the influence of the carrier-to-noise ratio. Therefore, most multipath standard deviation models are obtained depending on the elevation with respect to the horizon (NED frame).

That being said, we set to normalize both the raw multipath and smoothed multipath with their respective standard deviations so as to detrend its dependence to the satellite elevation, reducing its non-stationary nature. We will start with the smoothed multipath.

5.3.1 Smoothed Multipath Normalization

In order to normalize the obtained 100-s smoothed multipath for the L1, L5, E1 and E5a bands, we make use of the model introduced in Section 2.5.2. The elevation of each satellite with respect to the NED frame in every epoch (timestamp) can be obtained using the procedure already explained in Section 4.4.1, but without performing the last Euler angle transformation ($\boldsymbol{C}_{\text{NED}}^{\text{BF}}$). Once we have θ associated with each multipath sample we can substitute it in Equation (2.7) and simply divide the smoothed multipath value by the obtained $\sigma_{mp}(\theta)$.

5.3.2 Raw Multipath Normalization

Most available models are designed for the 100-s smoothed multipath. Because of this, we opted to develop our own model of the standard deviation of raw multipath using all the flights available from the DUFMAN project data for the L1, L5, E1 and E5a bands individually.

First, we obtain the elevation of every specific satellite with respect to the NED frame for every timestamp associated to a measurement sample. Then, we the raw multipath samples are sorted in elevations bins of 5° starting in 0° and ending in 90°. The reason we chose this bin size is the fact that it is the minimum bin size that guarantees enough samples to compute the standard deviation (especially in the first and last bins).

Since we aim to estimate the standard deviation of empirical data, it is also important to ensure the multipath samples can be considered independent between them. With that objective in mind, we only use samples that are at least 25 seconds apart from each other. This value is adopted following the raw multipath correlation time proposed in recent MOPS [1] for the GPS L1 band. In other words, we assume that raw multipath can be considered uncorrelated after the correlation time has passed. Figure 5.4 shows the number of raw multipath samples for the GPS L5 band after ensuring they are at least 25 seconds apart from each other.

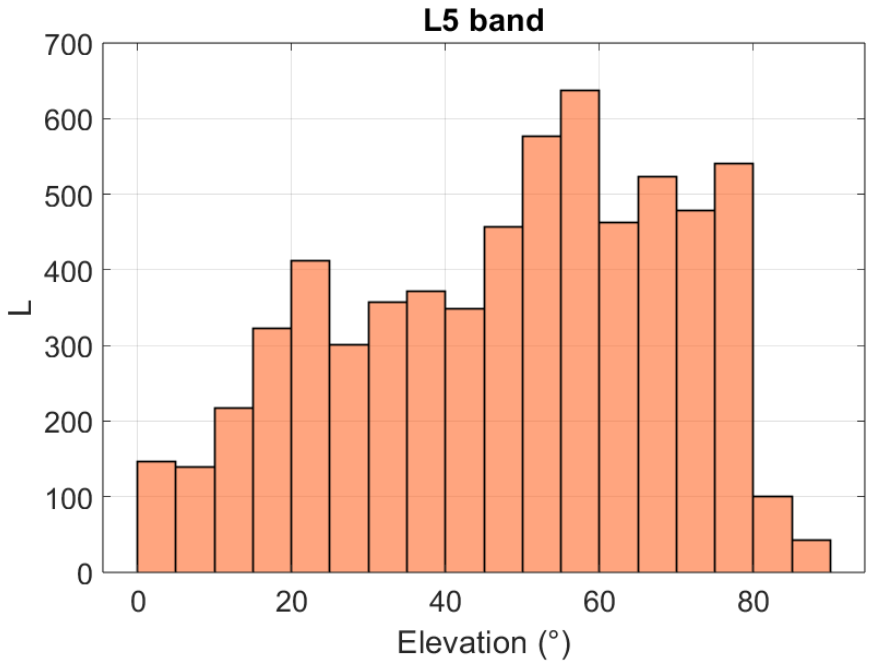

Figure 5.4: Number of independent samples (L) of L5 band raw multipath for every elevation bin.

Furthermore, we also have to take into account the effect that having a limited number of samples has on estimating the standard deviation of each bin. For the purpose of ensuring statistical representation of the true spread of the data, we apply an inflation factor. Based on the methodology used to derive the previous model for 100-s smoothed multipath standard deviation (Section 2.5.2), the inflation factor (F) is defined as [2]:

$$F = \sqrt{\frac{L-1}{\chi^2_{L-1}}}\,, \tag{5.2}$$

where L is the number of independent samples in the specific bin and χ^2_{L-1} is the value for which the Chi-squared distribution has the probability $(1-\alpha)$. The reason for using this formula is the fact that variance estimate obtained from a limited number of samples follows a Chi-squared distribution with $L-1$ degrees of freedom [2]. In our case we decided to choose $\alpha = 0.05$ for a 95% confidence bound, similar to the one used in [2]. After that, we compute the standard deviation for each elevation bin and multiply it by the inflation factor.

Since it is widely assumed that the σ_{mp} follows an exponential model as we can see in Figure 2.4 and Figure 2.5, we will also adopt this model for the raw multipath. The idea is to fit the same exponential model for the computed standard deviation of each frequency band:

$$\sigma_{raw\ mp} = a_1 + a_2 \cdot exp\left(-\frac{\theta}{a_3}\right) \ , \tag{5.3}$$

where $\theta \in [0°, 90°]$ is the elevation of the satellite with respect to the NED frame and a_1, a_2 and a_3 are the parameters to fit the model. In Figure 5.5 we can see the result of applying this methodology to the raw multipath of GPS's L1 band.

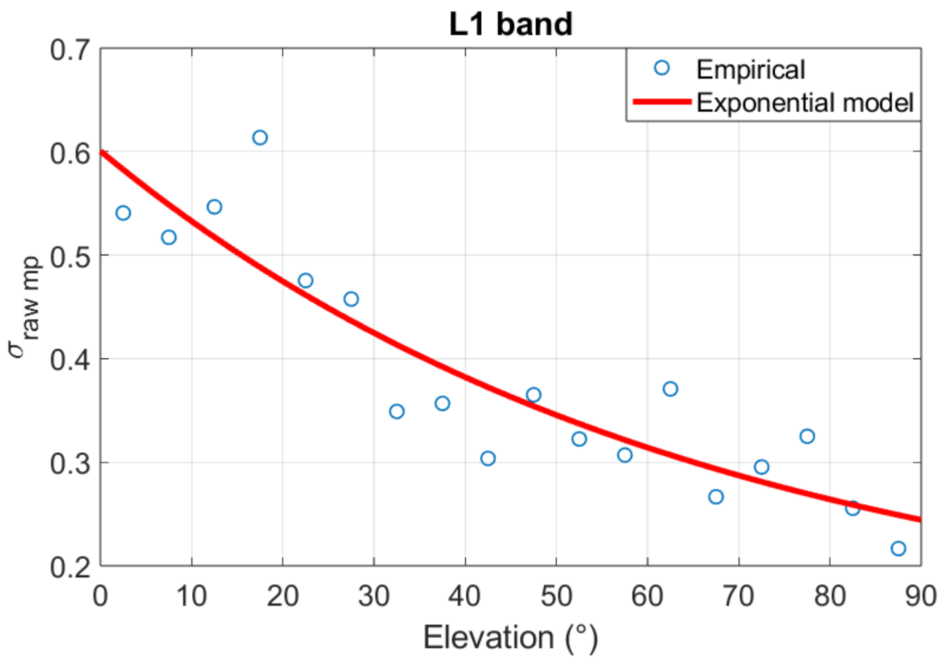

Figure 5.5: Computed standard deviation for L1 band raw multipath and its exponential model fit from Equation (5.3).

Once we have the exponential model fit for each frequency band (L1, L5, E1 and E5a), we can evaluate the computed θ for every timestamp and normalize each respective raw multipath sample (divide it by its corresponding $\sigma_{raw\ mp}$ value).

5.4 Autocorrelation and Power Spectral Density

Chapter 3 provided the theoretical basis of the correlation and frequency analysis. However, there are some important considerations when dealing with real data. First, we define the biased ACF of multipath as the expression in Equation (3.3), which will be obtained using the function *xcorr* from MATLAB. Second, we compute the PSD, defined in Equation (3.8), by applying MATLAB's *fft* function to the resulting ACF of multipath.

Although the final result of the entire modeling process is the Frequency Domain Overbounding of the multipath error derived from its PSD, the ACF can also provide insight on how the process correlation behaves in the time domain (multipath correlation time). To facilitate this analysis, we will use the normalized ACF only when examining the multipath correlation characteristics in the time domain. However, it is important to clarify that the normalized ACF is not used for the computation of the PSD.

Finally, we opted for only including continuous multipath data segments longer than 5000 samples in the analysis and modeling. The reason for this is the effect of having a limited number of samples to estimate the PSD, and the choice of minimum length was justified in Section 3.4. In the case of having a sampling interval $\Delta t = 0.2\ s$, the continuous multipath segments have a minimum length of $0.2\ s \times 5000 = 1000\ s$.

5.5 Frequency Domain Overbounding

Overbounding, as its name implies, consists in finding a model that is under all circumstances bigger than the magnitude we want to bound, in our case, the airborne code-phase multipath error. At the same time, the overbound model should have the minimum distance possible to the multipath error, to avoid extra conservatism.

Overbounding the error in the time (autocorrelation) domain does not guarantee it will be bounded in the position domain [15]. However, it has been proven that overbounding the error in the frequency domain does indeed ensure the position domain bounding [37]. Once we have the overbounding model that characterizes the error is obtained, it can be implemented in a Kalman Filter. This overbounding model should be as simple as possible to facilitate its incorporation in the Kalman Filter equations.

Similarly to recent work regarding high integrity time-correlated error models

[3][4][15][25], we chose to also use the theoretical First Order Gauss Markov Process (FOGMP) as the frequency domain overbounding model, which is stationary and easily parameterized as discussed in Section 3.3. In this work, we have found that the theoretical FOGMP can adjust the multipath error behavior in the frequency domain in most cases. Nevertheless, we decided to add a third parameter to the model besides the variance (σ^2) and the time-correlation constant (τ) of the FOGMP. Adding a base level of constant white noise allows us to more tightly bound the multipath error in some instances where using only the FOGMP results in an overly conservative bound. It also allows for a more consistent implementation in the measurement model of Kalman filters [37]. To better understand this difference, Figure 5.6 displays the PSD of two identical FOGMPs with the following parameters: $\Delta t = 0.2$, $\sigma^2 = 1$ and $\tau = 20s$. However, a constant value of W/Hz (white noise) is added on top of only one of the FOGMPs. In Chapter 7 we will see that the addition of a white noise will be especially useful when bounding the L5 and E5a unsmoothed multipath.

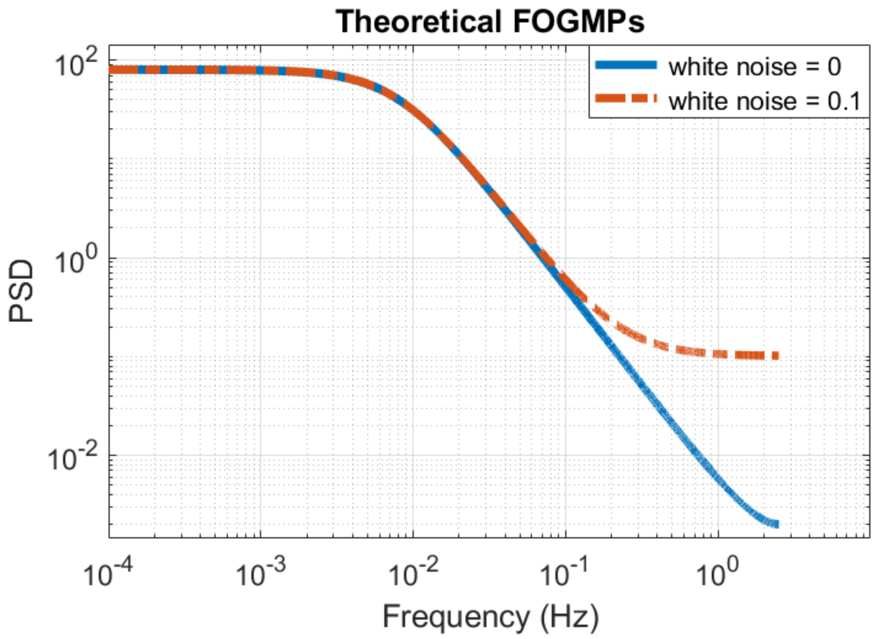

Figure 5.6: PSD comparison between two identical theoretical FOGMPs when adding a base level of constant white noise to one of them.

The final outcome of the frequency domain overbounding process is finding the value of the 3 parameters of the FOGMP model (σ^2, τ) and white noise that overbound each of the mulitpath types defined in Table 5.1 for each frequency band (L1, E1, L5 and E5a). This results in 16 different multipath overbounding models: L1 Unsmoothed Normalized, E5a Smoothed Unnormalized, etc.

To find the optimal overbound, a triple loop is performed, sweeping each parameter and obtaining the corresponding theoretical FOGMP PSD for that specific combination of σ^2, τ, and white noise values. Then, the Mean Squared Error (MSE) is computed between the overbound and each processed multipath segment PSD. Next, all the resulting MSE are added up together to form a total MSE. The optimal combination of the 3 parameter values is that for which the overbound is always bigger than all the multipath segments PSD and the total MSE is minimum.

Part III

Evaluations and Results

6. Flight Data

This thesis focuses on the development of new airborne GNSS models. One essential element is therefore the usage of data in representative operational scenarios. This chapter gives an overview of the data used in this work which was obtained from real tests flights.

6.1 Test Flights

The purpose of these test flights was to provide empirical data to develop multipath models for civil aviation GPS L5 band and Galileo E1 and E5a bands and they belong to the European Commission's DUFMAN project. For that purpose, several test flights equipped with a Multi-Model Receiver (MMR) were conducted to gather GNSS data. Unlike the standard L1 single-frequency receivers currently used in civil aviation, the experimental MMR is a multi-frequency receiver capable of operating simultaneously with signals from L1, L5, E1 and E5a bands.

Figure 6.1: Example of the Airbus A320 model (DLR's ATRA test aircraft).

The thesis evaluates the proposed methodology with real flight data from the DUFMAN project. It encompasses a total of 10 test flights, each of them using one of these 4 Airbus aircraft models: A320, A321, A330 and A350. All of these flights were conducted throughout the year 2019 and most of them have a approximate duration of 2.5/3 hours. Table (6.1) lists all the aircraft model types and the test flights performed with each of them.

<table>
<tr><th>A320</th><th>A321</th><th>A330</th><th>A350</th></tr>
<tr><td rowspan="2">F0502</td><td rowspan="2">F0324</td><td rowspan="2">F0314</td><td>F0638</td></tr>
<tr><td>F0640</td></tr>
<tr><td rowspan="2">F0503</td><td rowspan="2">F0325</td><td rowspan="2">F0315</td><td>F0641</td></tr>
<tr><td>F0642</td></tr>
</table>

Table 6.1: All test flights which data is available for this thesis and their respective aircraft model type.

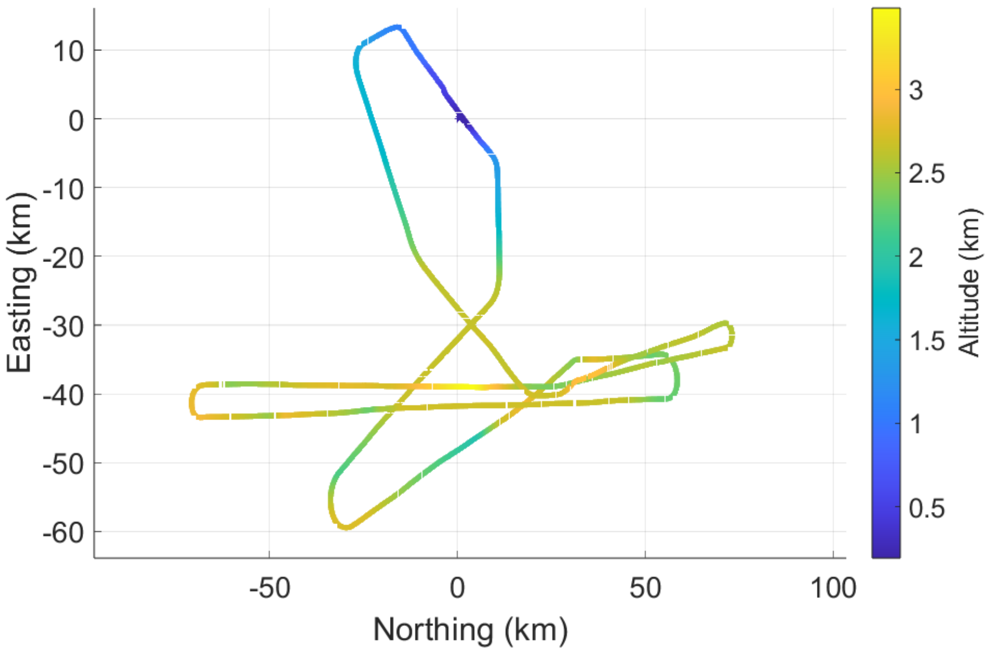

Figure 6.2: Flight F0640 position in the NED coordinate frame with respect to the take-off/landing point.

As an example, Figure 6.2 shows the flight F0640 position in local frame using the take-off/landing point as the origin of coordinates (0,0). Its altitude with respect to the ground is also represented color coded.

For every flight, GNSS data and aircraft attitude data is available:

6.1.1 GNSS Data

All the GNSS data was obtained from an aircraft MMR using a sampling frequency (f_s) of 5 Hz, and a correlator with 0.1 chips spacing and 20 Hz of bandwidth. Now, we will focus on explaining all the relevant information recorded.

- **GPS time**: in order to know when each measurement was taken it is necessary to have timestamps. In the case of this data, these are given in GPS, which provide the gps week, and the second of the week respectively. Although the timestamps are in GPS time format, it is important to clarify that all the data (including Galileo measurements) share these timestamps.
- **Code-phase**: code-phase raw measurements (pseudoranges) for all the visible and tracked satellites in the GPS L1 and L5 bands, as well as Galileo E1 and E5 bands. Each row represents one epoch and every column is a different SV.
- **Carrier-phase**: carrier-phase raw measurements also for all the satellites tracked in the L1, L5, E1 and E5 bands.
- **Satellite positions**: computed from the ephemeris data (navigation message), it provides the position in the ECEF coordinate frame for each SV of the GPS and Galileo constellations. Together with the receiver position and the airplane's attitude, it is used to calculate the elevation of each satellite with respect to the body frame in Section 4.4.
- **Receiver position**: it represents the aircraft's position also in the ECEF coordinate frame for each epoch. It was computed using the Position-Velocity-Time (PVT) algorithm.

6.1.2 Attitude Data

The information regarding the airplane's attitude was obtained from aeronautic equipment installed inside the aircraft based on its inertial reference system. This data was sampled at a frequency of 8 Hz and it provides the following information:

- **Timestamps**: contrary to the GNSS data, the attitude data timestamps are synchronized with GPS but are not given in the GPS time format. Instead, the day of the year (1 to 365) is provided along with the time of the day (HH:MM:SS) when each row of measurements was obtained. The seconds have decimal places with a precision of 125 milliseconds due to the sampling frequency.

- **Heading**: it provides the angle between the direction the aircraft is headed and the true north. It is given in degrees and varies between [0°, 360°].
- **Pitch**: is the angle in degrees between the aircraft's longitudinal axis and the horizon for each epoch. Its value range is [-90°, 90°].
- **Roll**: represents the angle of rotation around the longitudinal axis, causing the wings to tilt. The aircraft's roll is also given in degrees and with a value range [-90°, 90°].

6.2 Antenna Model

In Section 4.4.2, a specific antenna model was used to remove the AGDV from the CMC multipath component. This model is based on JAVAD AIRANT antenna and it is not an outcome of this thesis [32][38]. In order to develop it, measurements of the JAVAD AIRANT antenna were performed inside DLR's anechoic chamber (Figure 6.3 [38]).

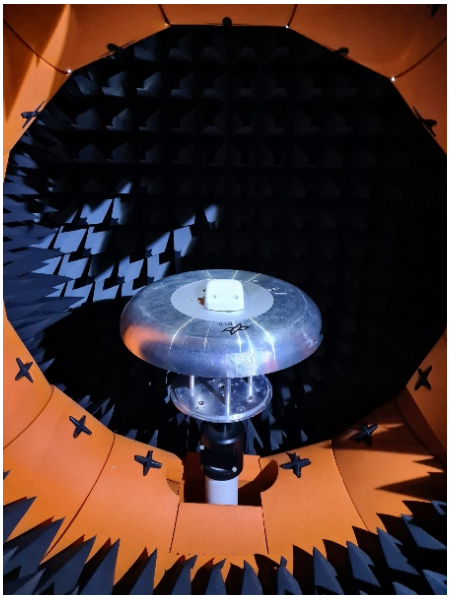

Figure 6.3: JAVAD AIRANT antenna being modeled inside DLR's anechoic chamber.

The result of this antenna model is a look-up table containing the AGDV error in the code-phase for the L1, E1 and L5/E5a bands depending on the elevation and azimuth angles of arrival of the signal to the antenna. The AGDV values are available for increments of 2° for the elevation angle $\theta \in$ [0°, 90°] and the azimuth angle $\psi \in$ [0°, 360°]. In this work, we have decided to perform a 2D interpolation to determine the AGDV value for a specific elevation and azimuth angles.

6.3 Preprocessing

The GNSS data and the attitude data have different starting and finishing times, as well as a different sampling frequency. Because of this, the attitude data had to be preprocessed. First, the attitude timestamps were converted into GPS time format. Then, the attitude data was interpolated to match the timestamps corresponding to the GNSS data.

The attitude data has a higher sampling frequency than the GNSS data. Furthermore, the attitude data changes at a relatively slow rate compared to its sampling frequency (8 Hz). Paired with the fact that the GNSS data was not modified at any moment of the preprocessing, its effect on the fidelity of the data can be considered negligible.

7. Results and Discussions

This chapter presents the outcome of this thesis after the proposed methodology was applied to the data shown in Chapter 6. These results include the Autocorrelation Functions and the Power Spectral Densities of the different multipath processing options, as well as the final overbounding model for each of them.

7.1 Analysis

This section compares the different results depending on the factors involved in the multipath processing options: constellation/frequency band, smoothing and normalization. It is worth noting that each individual line (identified by a specific color) represented in any figure of this chapter corresponds to one time series of multipath from a certain satellite and a certain test flight.

7.1.1 GPS vs Galileo

Autocorrelation Analysis

It was mentioned in Section 2.5.3 that current MOPS give a reference value of 25 seconds for the correlation time of the GPS L1 band raw multipath (Unsmoothed Unnormalized). If a threshold of ± 0.2 for the normalized ACF is considered as a limit of weak correlation (tipical in statistics), this claim also holds true for our results. As we can see in Figure 7.1a, the majority of the L1 Unsmoothed Unnormalized multipath segments ACFs drop below 0.2 after 25 seconds have passed.

On the other hand, the Galileo E1 band Unsmoothed Unnormalized multipath exhibits a longer correlation time in Figure 7.1b. Using the same ACF threshold as before, its correlation time appears to be closer to 50 seconds. In the case of the L5 and E5a Unsmoothed Unnormalized multipath, the obtained results indicate that they both posses a correlation time of 200 seconds approximately.

(a)

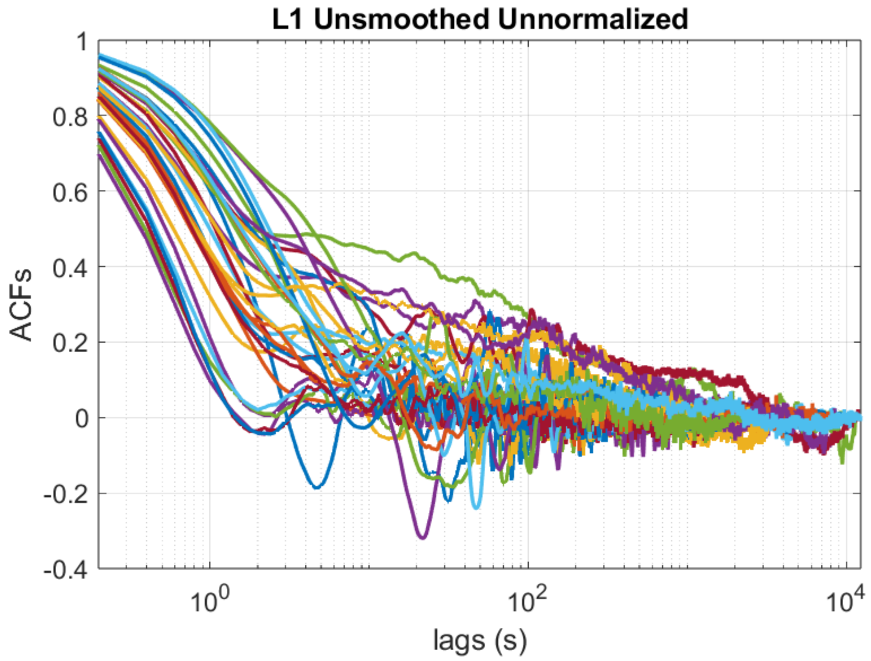

(b)

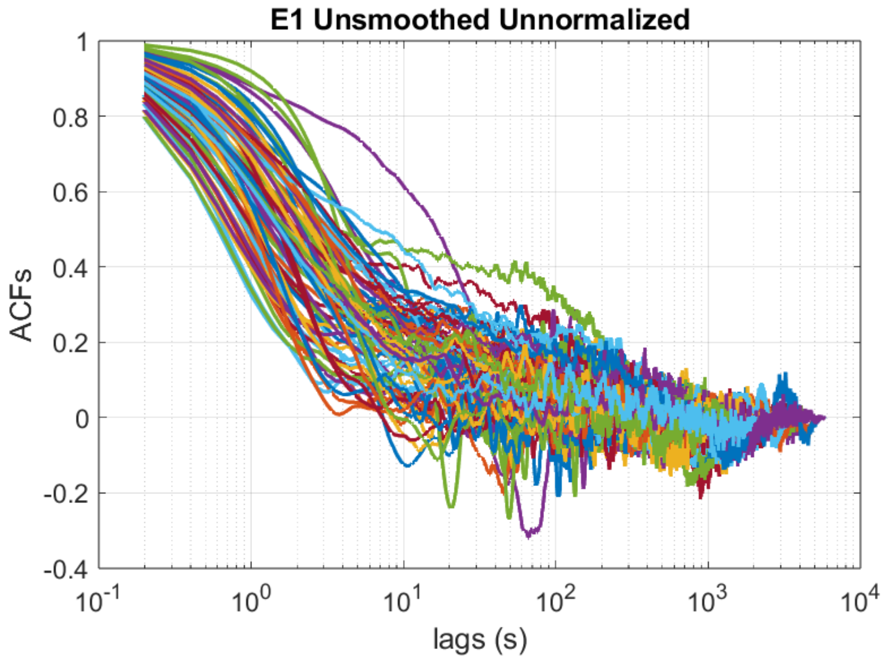

Figure 7.1: Normalized ACF of L1 band (a) and E1 band (b) Unsmoothed Unnormalized continuous multipath segments from all flights.

Power Spectral Densities

(a)

(b)

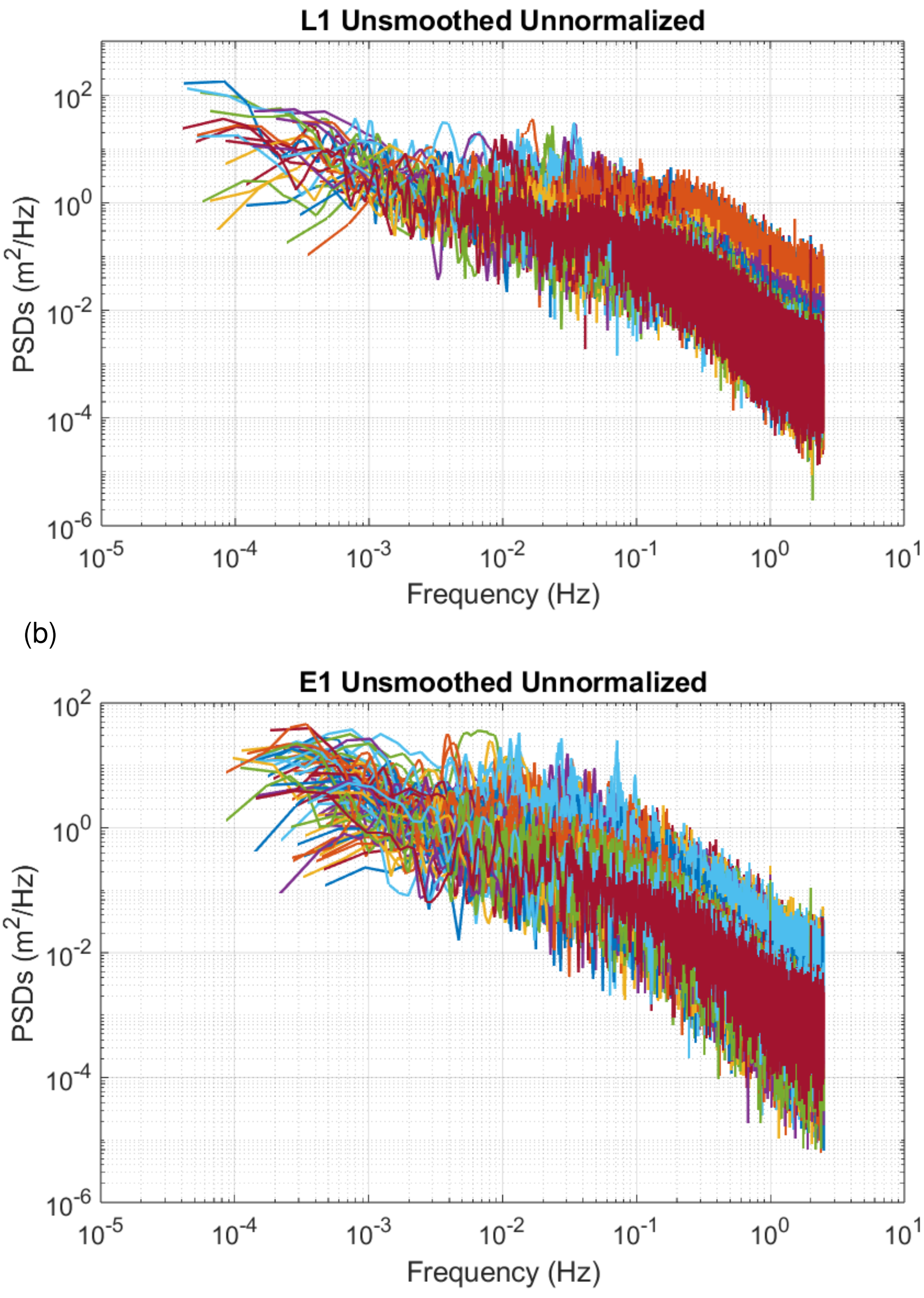

Figure 7.2: PSD of L1 band (a) and E1 band (b) Unsmoothed Unnormalized continuous multipath segments from all flights.

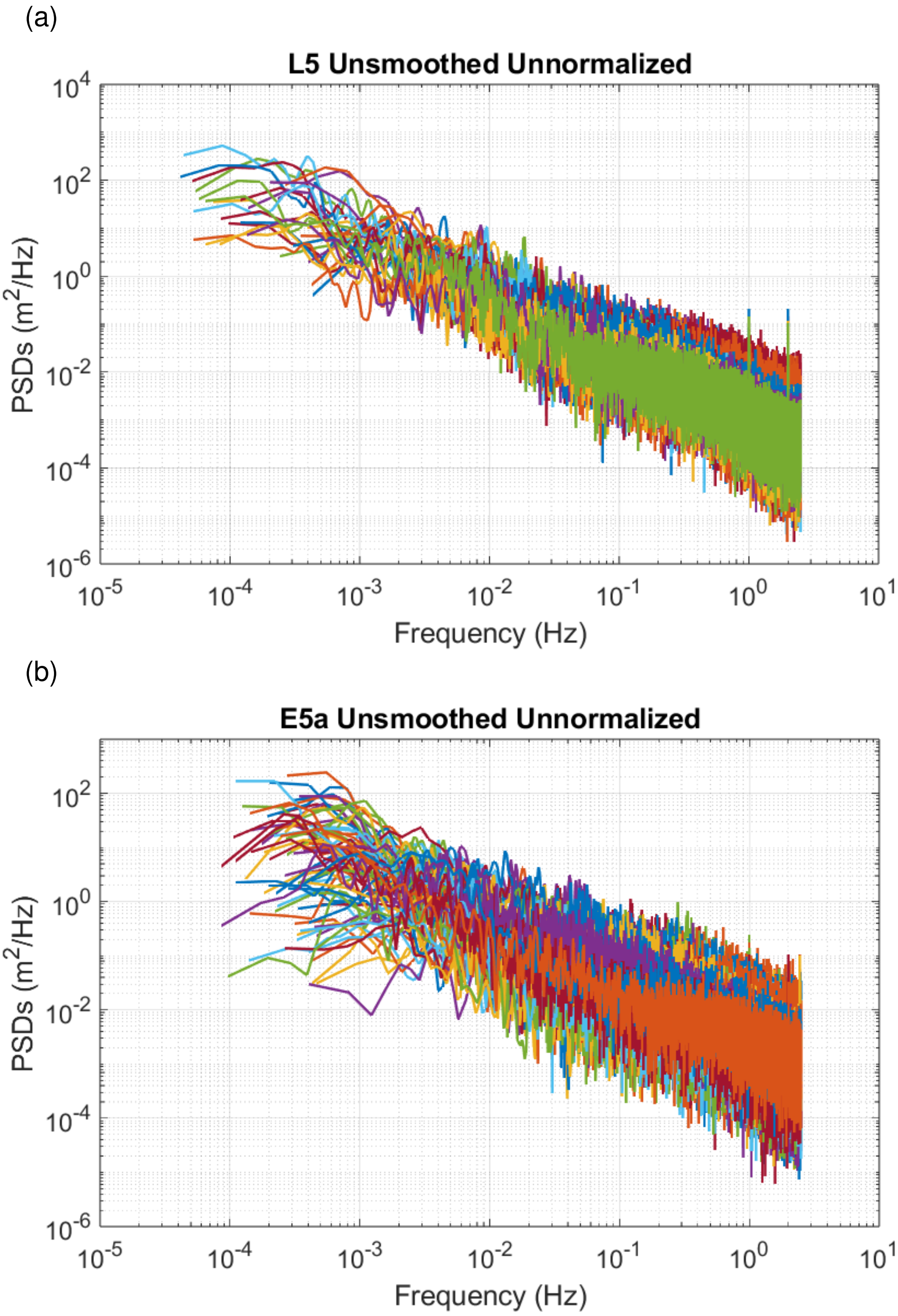

Figure 7.3: PSD of L5 band (a) and E5a band (b) Unsmoothed Unnormalized continuous multipath segments from all flights.

As we can see in Figure 7.2b, the PSD curves of Galileo E1 band raw multipath (Unsmoothed Unnormalized) are slightly below the PSD values of the GPS L1 band raw multipath in Figure 7.2a. The PSDs of Galileo E5a band raw multipath also appear to be below the ones of the GPS L5 band (Figure 7.3). However, in this case the difference between them is smaller.

These results can be considered reasonable since code-phase measurements from Galileo bands are more resistant to multipath than than GPS bands due to each constellation using different frequency modulations [39]. This effect is less prevalent when comparing the E5a and L5 bands. Nevertheless, later in this chapter, the final overbounding models will provide a more objective metric to compare them.

Comparing and Figure 7.2 and Figure 7.3, it can be seen that the PSD slope of the L5 and E5a Unsmoothed Unnormalized multipath is less pronounced than the L1 and E1 Unsmoothed Unnormalized multipath. As we will see in the next section, these are the only two instances where the PSD slope does not match that of a FOGMP.

7.1.2 Raw vs Smoothed

Autocorrelation Analysis

Figure 7.4 and Figure 7.5 compare the autocorrelation sequence of Unsmoothed Unnormalized multipath of L1 and E1 bands with their respective smoothed versions. Looking at both figures we can see that the correlation time is greatly increased when smoothing is performed. Furthermore, it can be seen that the noise effect is significantly reduced when applying the carrier-smoothing to the raw multipath.

The reason for the increase of the correlation time is intrinsically tied to the smoothing process. As we know, carrier-smoothing is a recursive algorithm that uses previous measurements to average the current one. This introduces a correlation between the multipath samples.

(a)

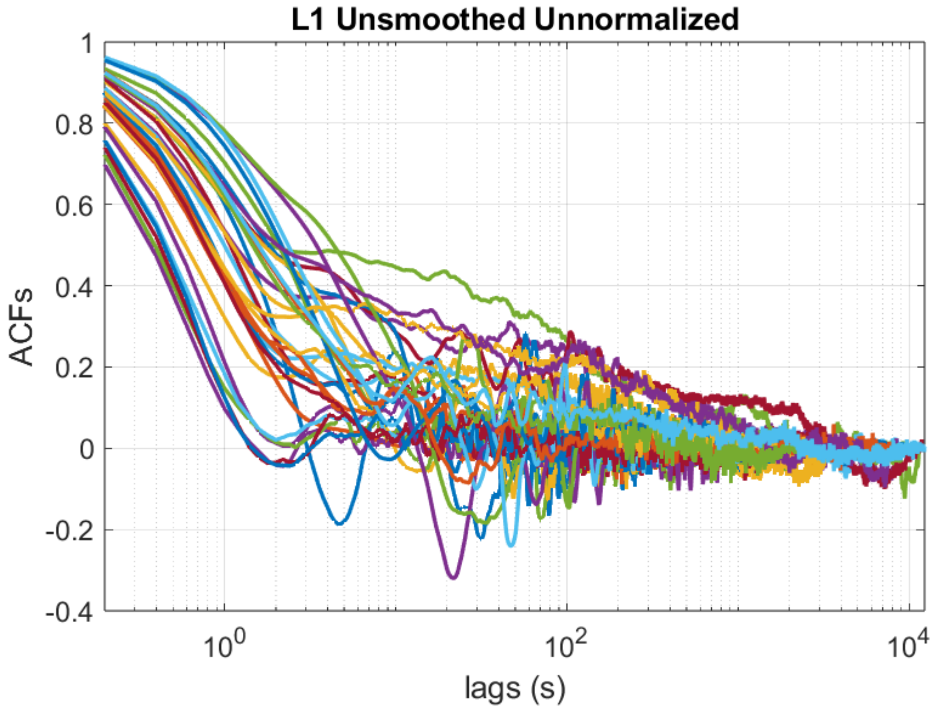

(b)

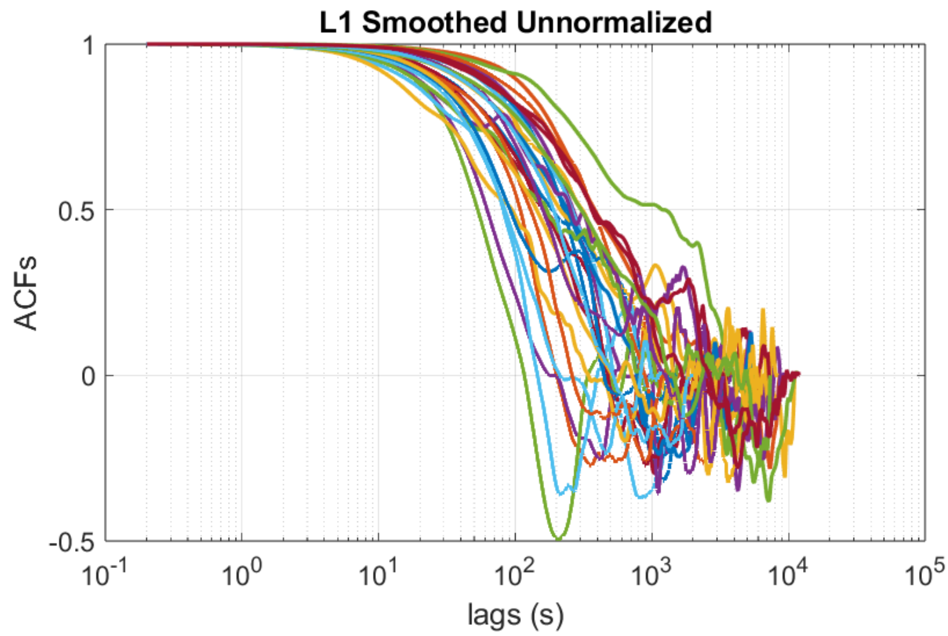

Figure 7.4: Normalized ACF of L1 Unsmoothed Unnormalized (a) and Smoothed Unnormalized (b) continuous multipath segments from all flights.

(a)

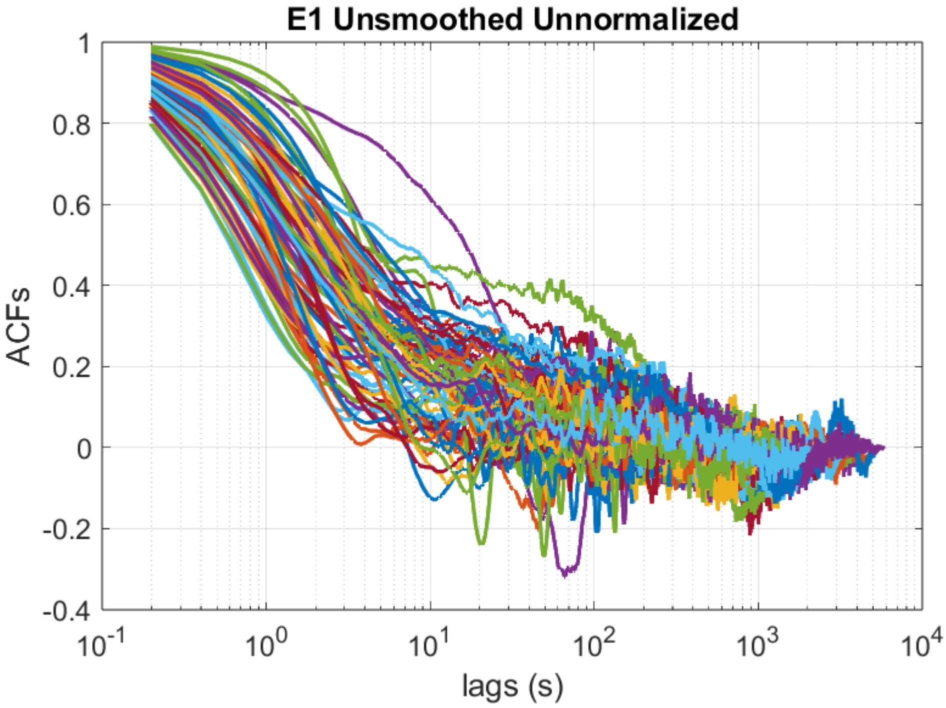

(b)

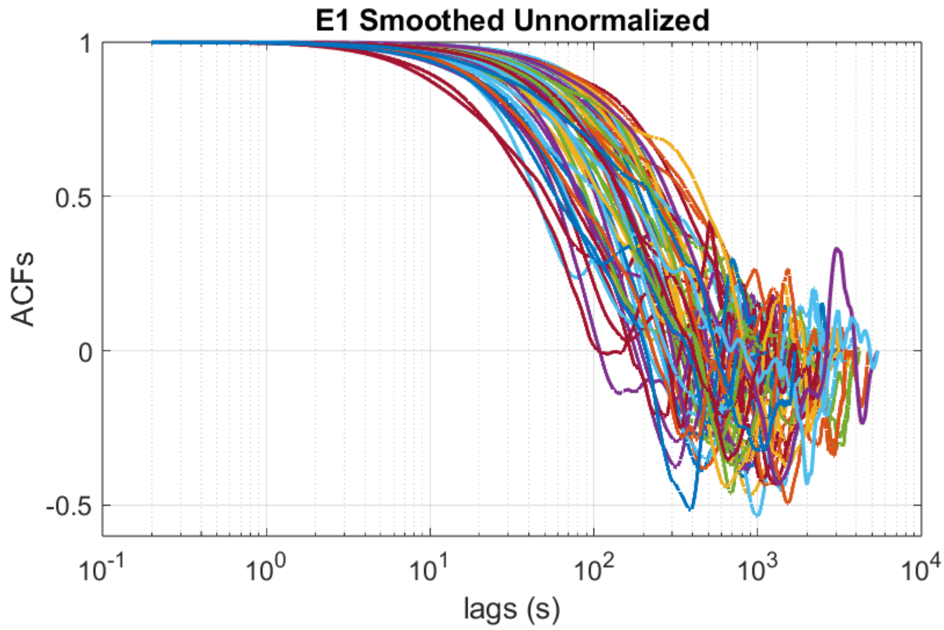

Figure 7.5: Normalized ACF of E1 Unsmoothed Unnormalized (a) and Smoothed Unnormalized (b) continuous multipath segments from all flights.

Power Spectral Densities

(a)

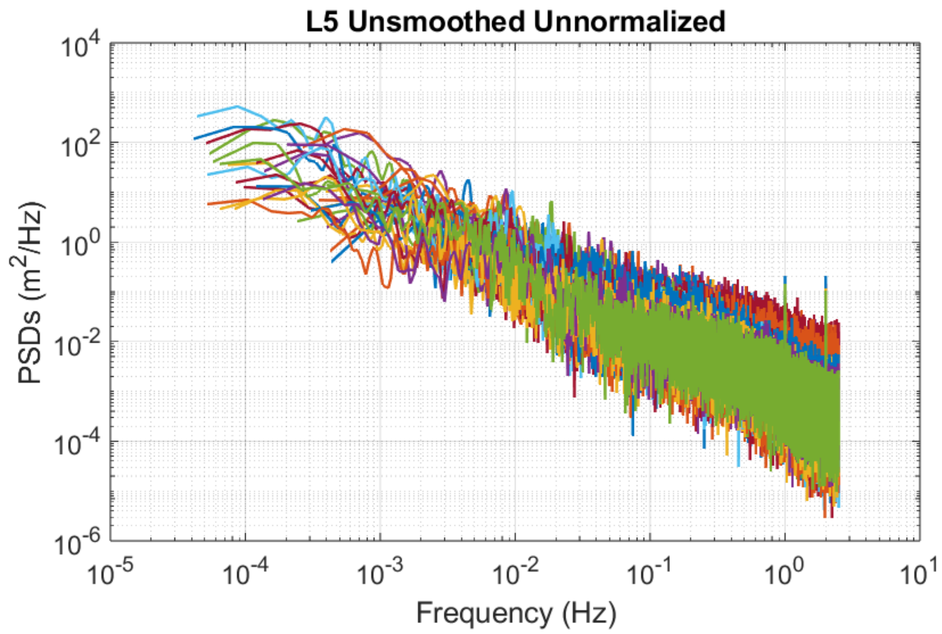

(b)

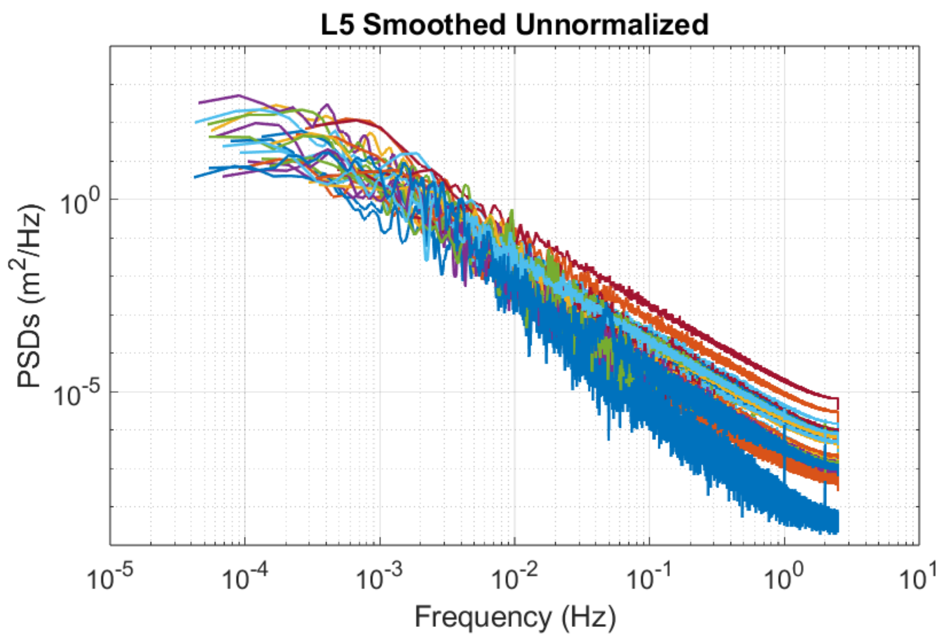

Figure 7.6: PSD of L5 Unsmoothed Unnormalized (a) and Smoothed Unnormalized (b) multipath segments from all flights.

(a)

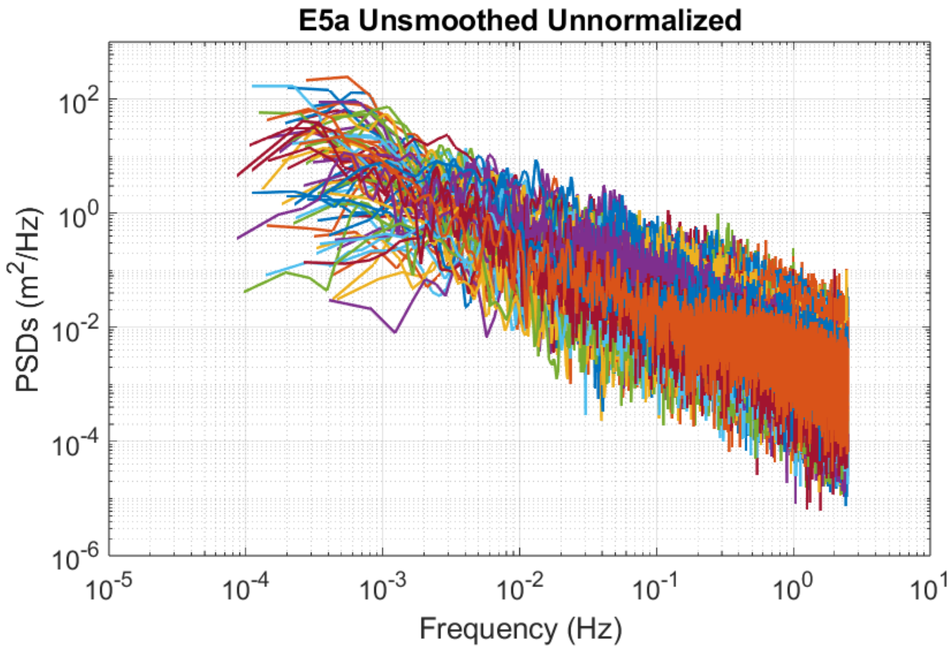

(b)

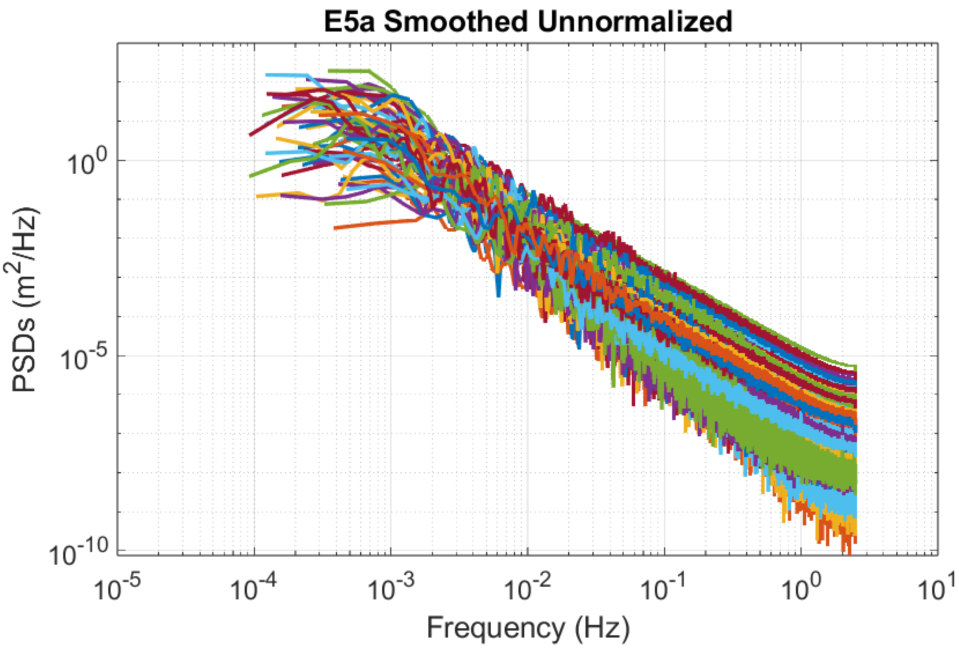

Figure 7.7: PSD of E5a Unsmoothed Unnormalized (a) and Smoothed Unnormalized (b) multipath segments from all flights.

7.1.3 Unnormalized vs Normalized

Autocorrelation Analysis

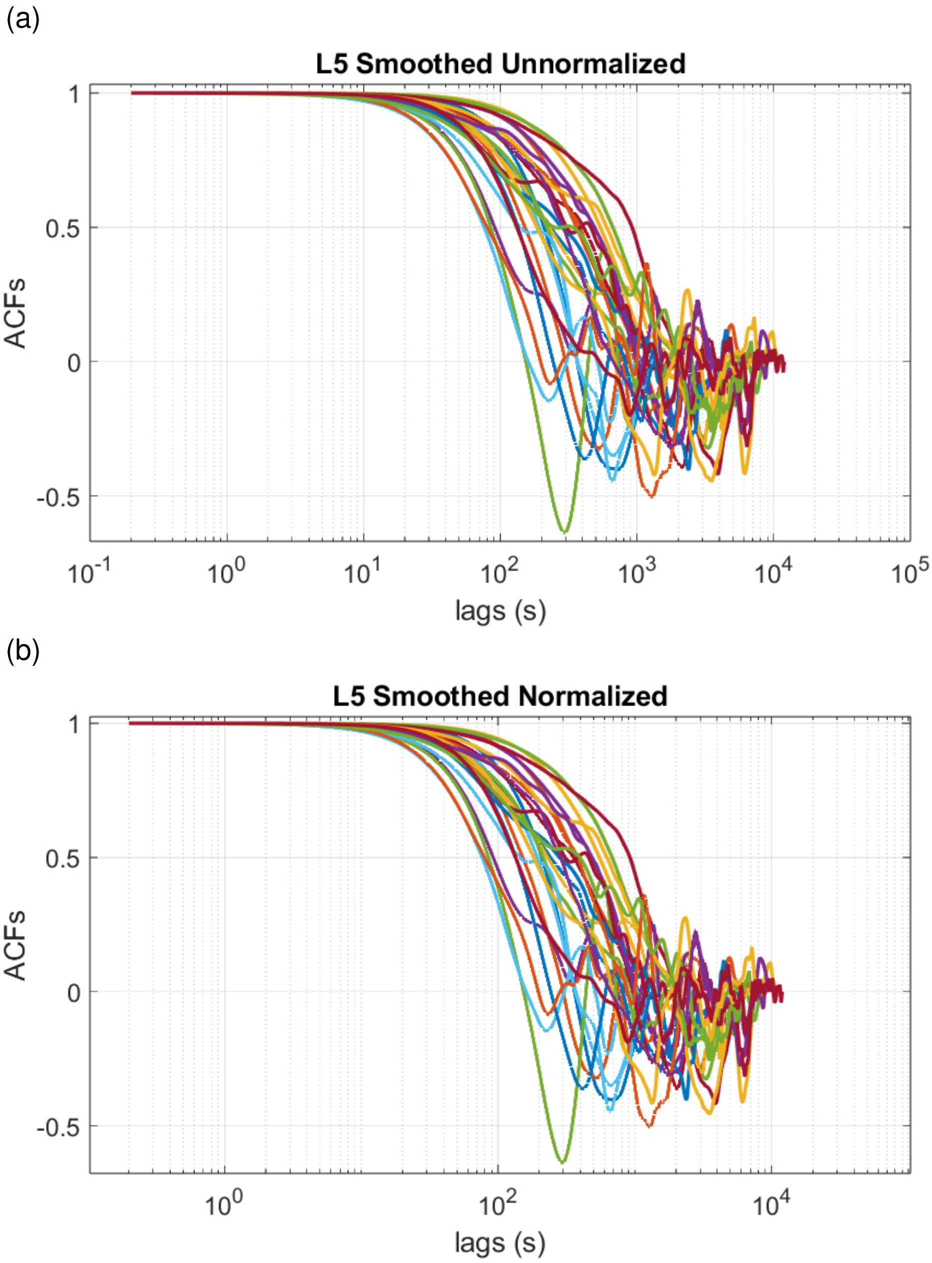

Figure 7.8: Normalized ACF of L5 Smoothed Unnormalized (a) and Smoothed Normalized (b) continuous multipath segments from all flights.

(a)

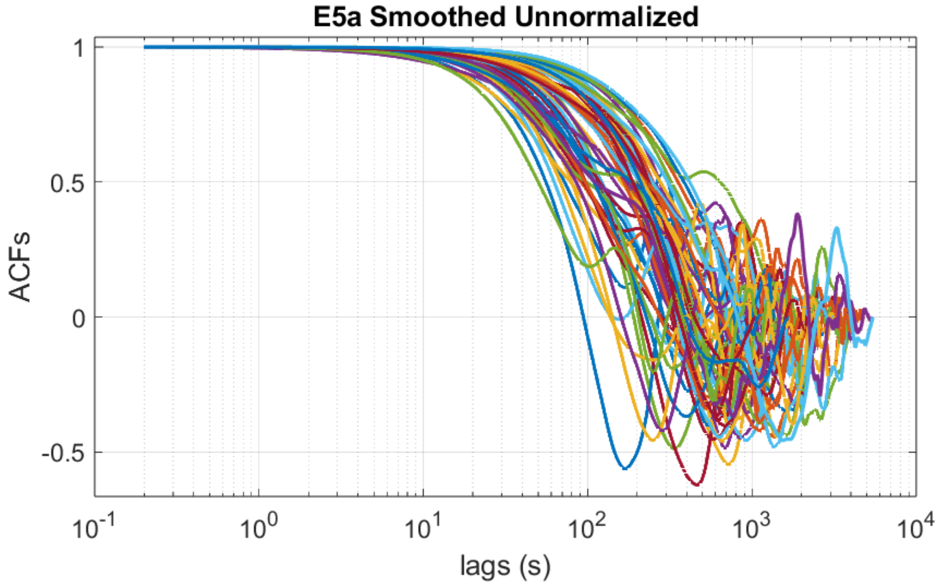

(b)

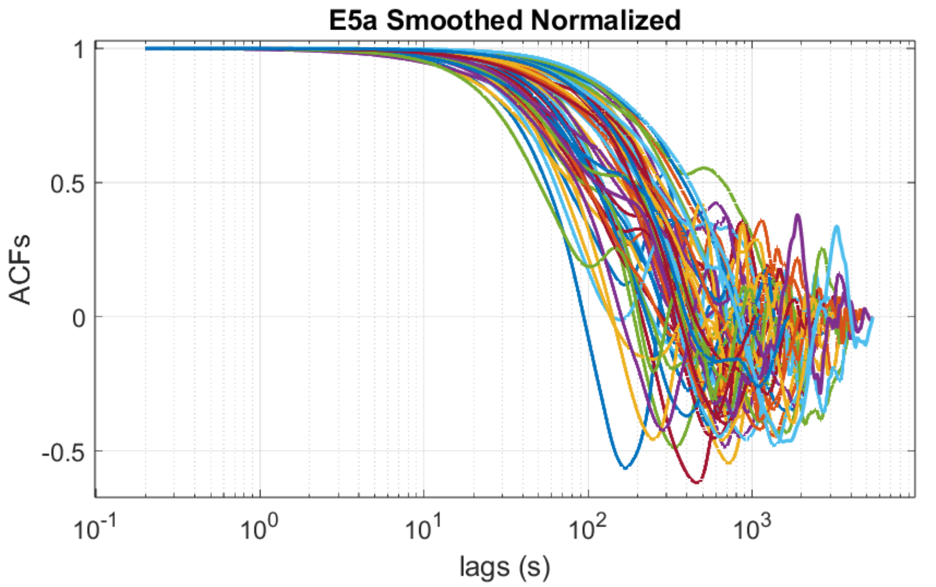

Figure 7.9: Normalized ACF of E5a Smoothed Unnormalized (a) and Smoothed Normalized (b) continuous multipath segments from all flights.

Figure 7.8 and Figure 7.9 show that process of normalizing multipath does not have a significant effect on the normalized ACF.

Power Spectral Densities

(a)

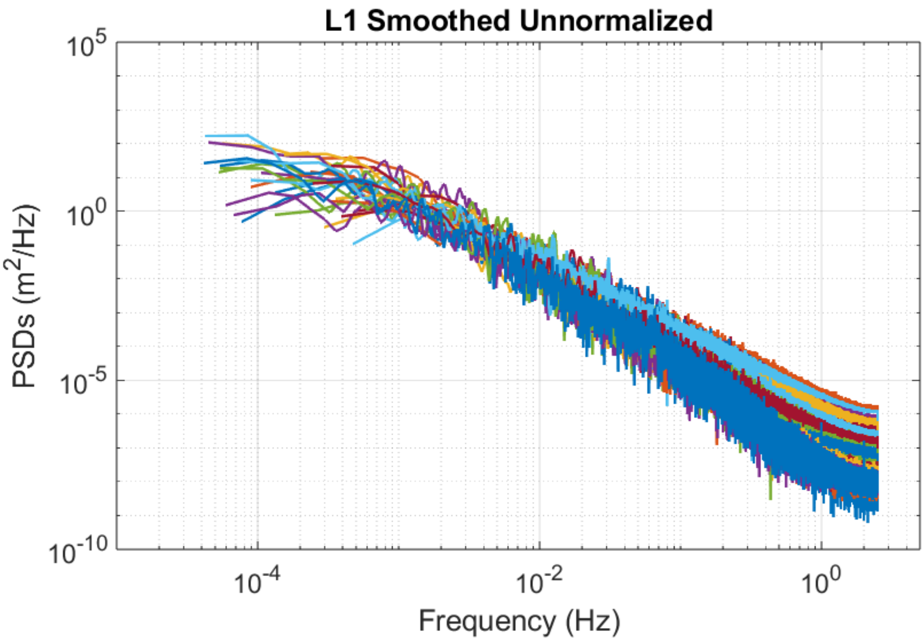

(b)

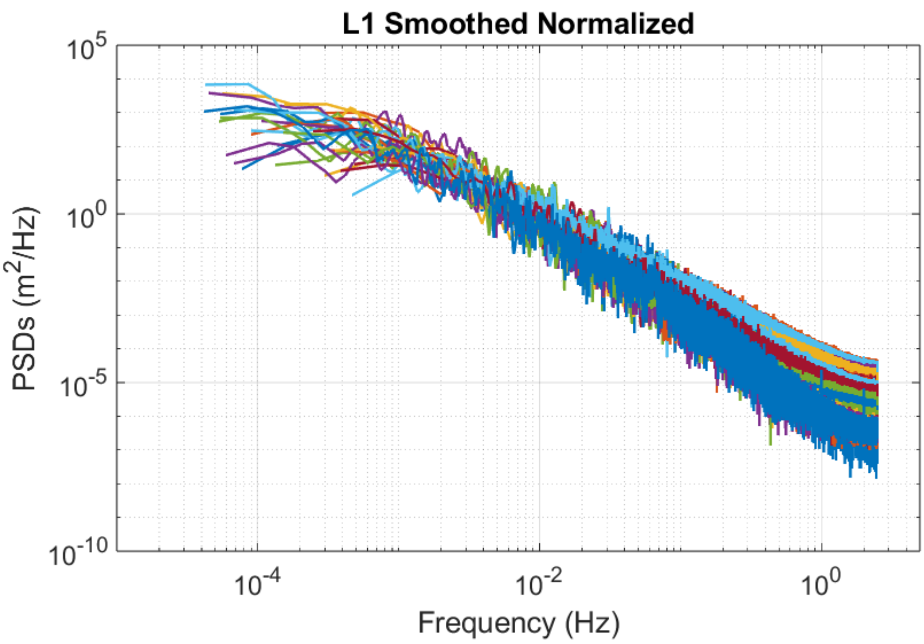

Figure 7.10: PSD of L1 Smoothed Unnormalized (a) and Smoothed Normalized (b) multipath segments from all flights.

(a)

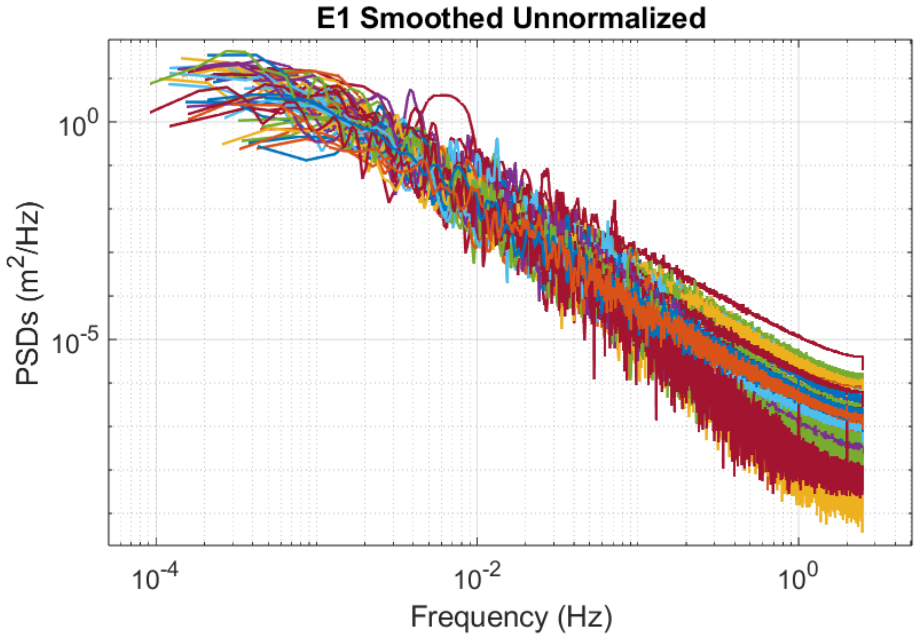

(b)

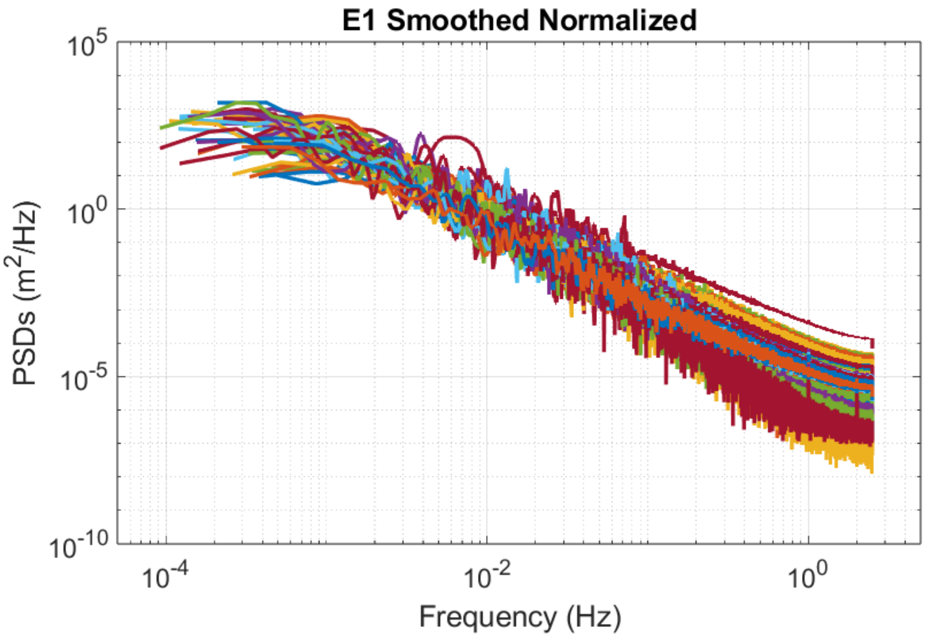

Figure 7.11: PSD of E1 Smoothed Unnormalized (a) and Smoothed Normalized (b) multipath segments from all flights.

Looking at Figure 7.10 and Figure 7.11 we can see that the normalization of multipath significantly increases the level of the PSDs. On the contrary, their behaviors are only slightly affected.

Section 2.5.2 and Section 5.3.2 presented the models of the standard deviation for smoothed multipath (σ_{mp}) and raw multipath ($\sigma_{raw\ mp}$), respectively. According to both models, the standard deviation of multipath for all frequency bands (L1, L5, E1 and E5a) is always below 1. For this reason, the amplitude of the multipath error is increased when normalizing it with its standard deviation. This leads to the observed increase of the PSD values.

7.2 Final Models

After applying the overbounding model described in Section 5.5 to the PSD of all 16 multipath processing options, the resulting parameter combination of σ^2, τ (in seconds) and white noise (σ^2_{WN}) in m^2/Hz, can be summarized in the following tables:

L1	Unsmoothed Unnormalized	Unsmoothed Normalized	Smoothed Unnormalized	Smoothed Normalized
σ^2	23	114	0.2	6
τ	2	2	219	303
σ^2_{WN}	0	0	0	0

Table 7.1: Final overbounding parameters of the proposed FOGMP model for GPS L1 band multipath.

E1	Unsmoothed Unnormalized	Unsmoothed Normalized	Smoothed Unnormalized	Smoothed Normalized
σ^2	6	65	0.2	6
τ	2	2	54	66
σ^2_{WN}	0	0	0	0

Table 7.2: Final overbounding parameters of the proposed FOGMP model for Galileo E1 band multipath.

L5	Unsmoothed Unnormalized	Unsmoothed Normalized	Smoothed Unnormalized	Smoothed Normalized
σ^2	4	22	0.5	25
τ	33	98	263	351
σ^2_{WN}	0.5	6	0	0

Table 7.3: Final overbounding parameters of the proposed FOGMP model for GPS L5 band multipath.

E5a	Unsmoothed Unnormalized	Unsmoothed Normalized	Smoothed Unnormalized	Smoothed Normalized
σ^2	2	22	0.5	28
τ	31	63	122	197
σ^2_{WN}	0.9	16	0	0

Table 7.4: Final overbounding parameters of the proposed FOGMP model for GPS E5a band.

There are only 4 out of the 16 multipath models that have a white noise value different than zero: L5 Unsmoothed Unnormalized and L5 Unsmoothed Normalized as seen in Table 7.3, and E5a Unsmoothed Unnormalized and E5a Unsmoothed Normalized as seen in Table 7.4. The reason for this is that their PSD slopes are less pronounced than the slope of a theoretical FOGMP, as it can be seen in Figure 7.16 and Figure 7.18.

In this situation, we could have simply used a FOGMP model without white noise to overbound these multipath processing options, causing an overestimation of the error. However, we decided to add the white noise parameter to more closely overbound the multipath error in these instances. Although the rest of the multipath models do not need the white noise parameter for the overbounding, we opted to unify all into one single model for the sake of simplicity.

Figure 7.12 and Figure 7.13 present two examples of the final overbounding models for the L1 band. Similarly, Figure 7.14 and Figure Figure 7.15 show two out of the four final overbounding models for the E1 band. Lastly, two examples of the final overbounding models for smoothed multipath in the L5 and E5a band can be seen in Figure 7.17 and Figure 7.19, respectively.

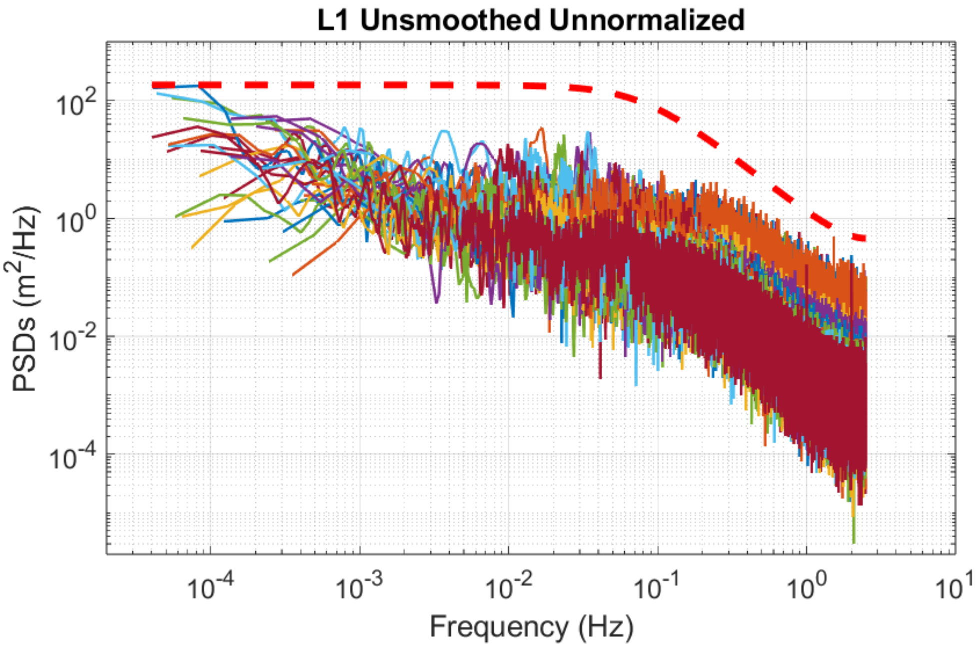

Figure 7.12: Final PSD overbound model with $\sigma^2 = 23$, $\tau = 2$ s, white noise $= 0$ for the L1 Unsmoothed Unnormalized multipath.

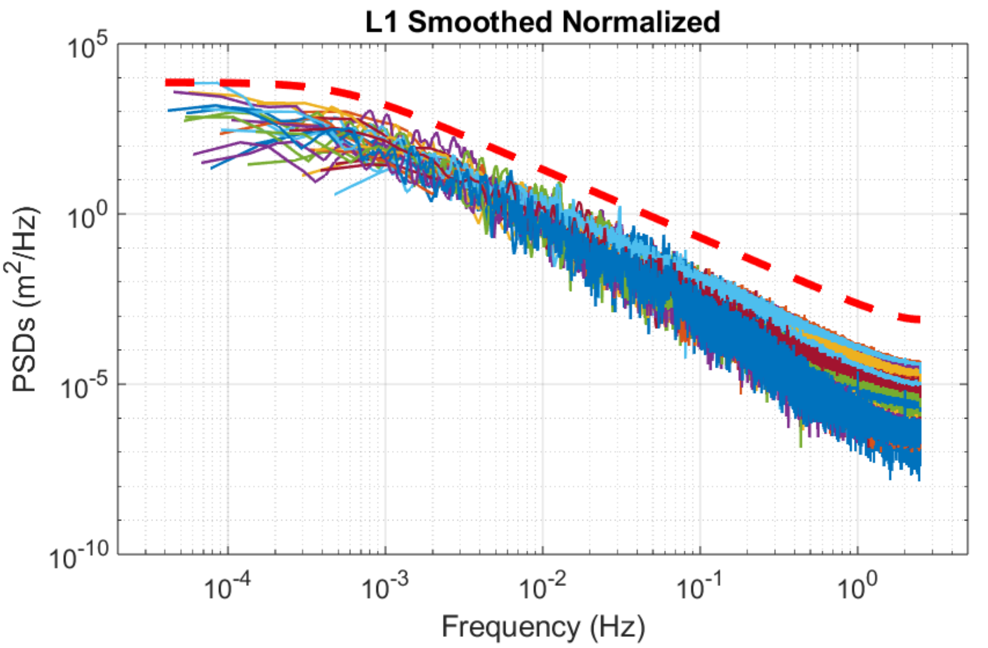

Figure 7.13: Final PSD overbound model with $\sigma^2 = 6$, $\tau = 303$ s, white noise $= 0$ for the L1 Smoothed Normalized multipath.

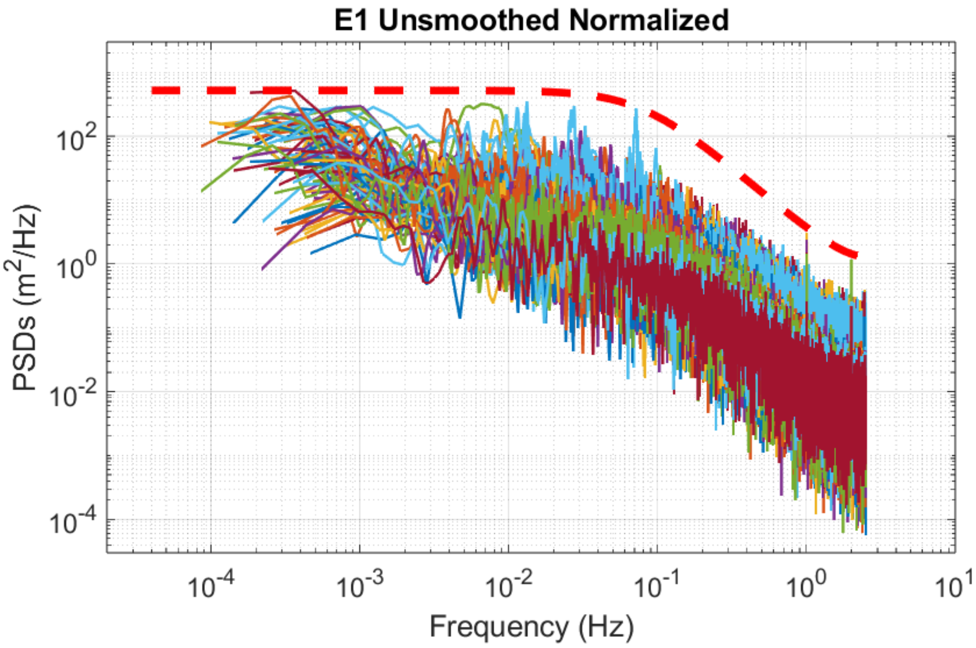

Figure 7.14: Final PSD overbound model with $\sigma^2 = 65$, $\tau = 2$ s, white noise $= 0$ for the E1 Unsmoothed Normalized multipath.

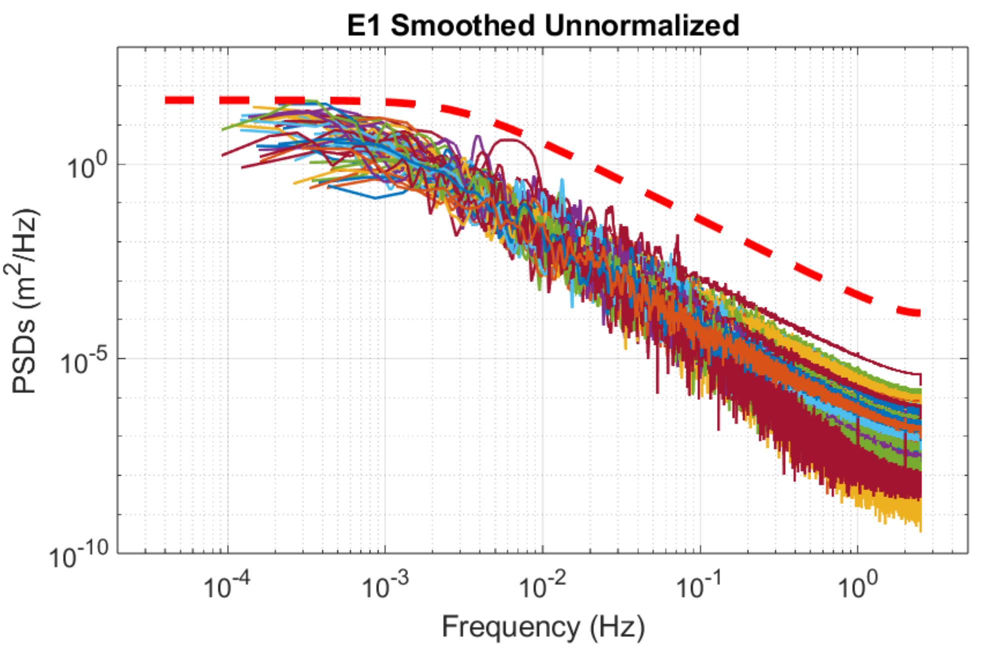

Figure 7.15: Final PSD overbound model with $\sigma^2 = 0.2$, $\tau = 54$ s, white noise $= 0$ for the E1 Smoothed Unnormalized multipath.

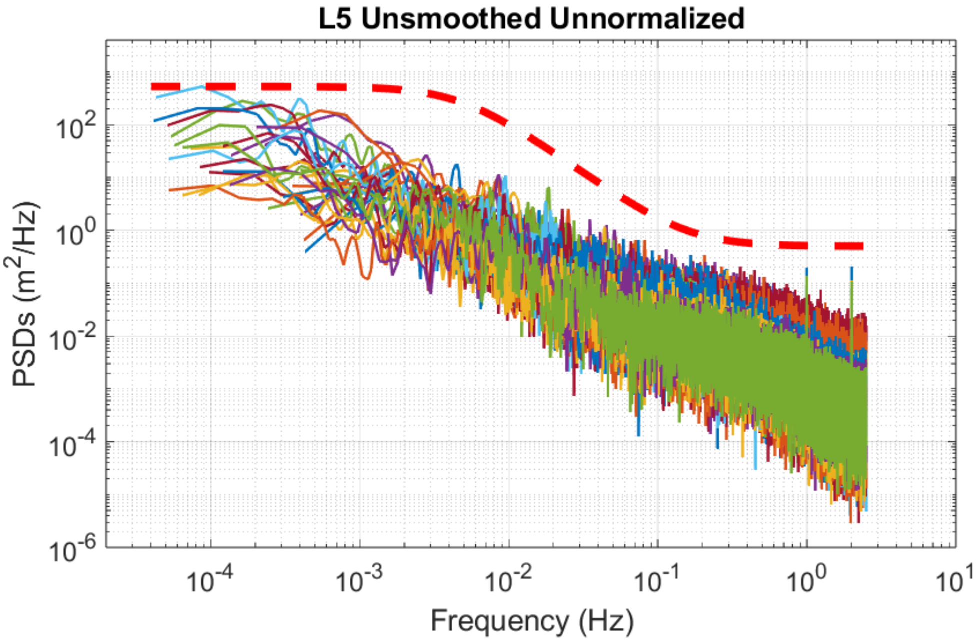

Figure 7.16: Final PSD overbound model with $\sigma^2 = 4$, $\tau = 33$ s, white noise $= 0.5$ m^2/Hz for the L5 Unsmoothed Unnormalized multipath.

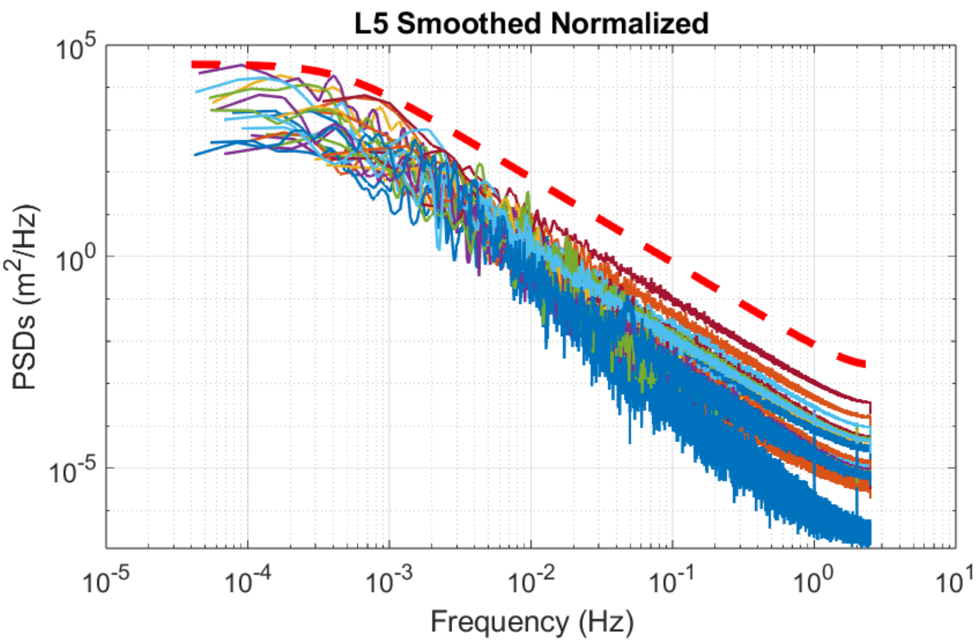

Figure 7.17: Final PSD overbound model with $\sigma^2 = 25$, $\tau = 351$ s, white noise $= 0$ for the L5 Smoothed Normalized multipath.

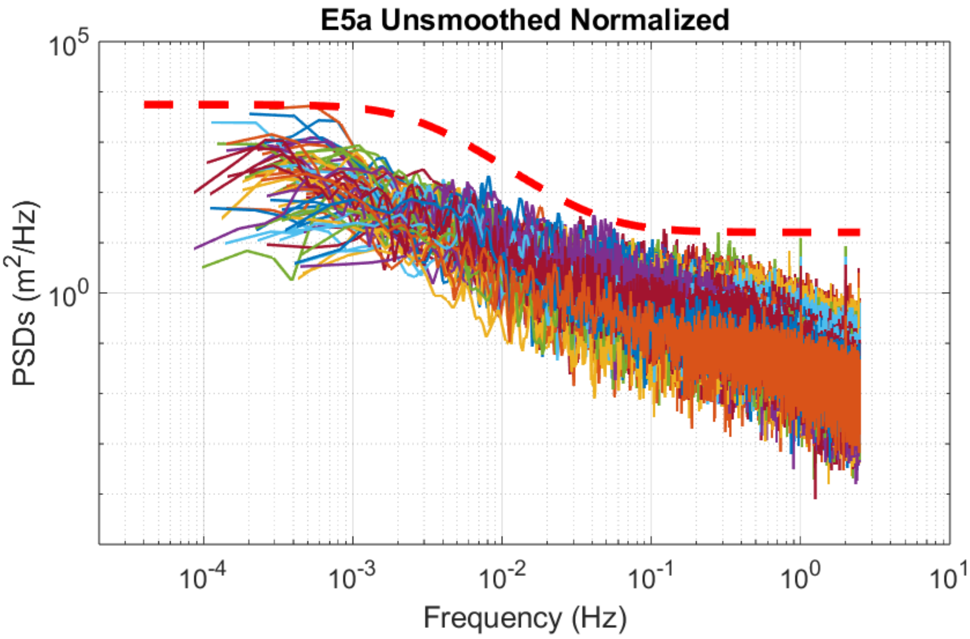

Figure 7.18: Final PSD overbound model with $\sigma^2 = 22$, $\tau = 63$ s, white noise $= 16$ m^2/Hz for the E5a Unsmoothed Normalized multipath.

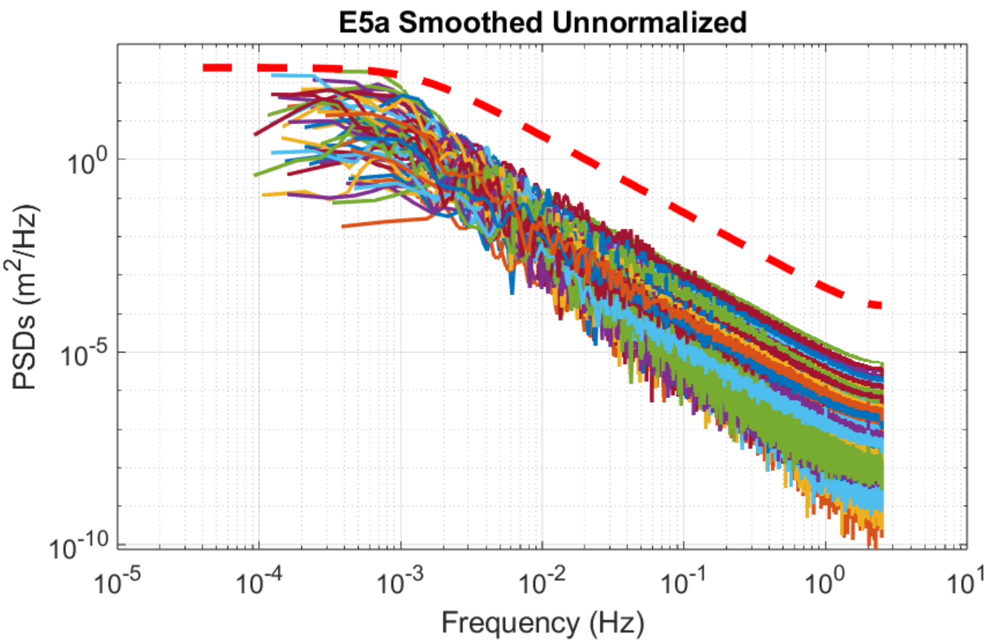

Figure 7.19: Final PSD overbound model with $\sigma^2 = 0.5$, $\tau = 122$ s, white noise $= 0$ for the E5a Smoothed Unnormalized multipath.

Part IV

Closing

8. Conclusions and Outlook

This chapter is dedicated to summarize the main achievements of this master thesis and present the key conclusions derived from the obtained results. In addition, the last section provides potential future research to continue with this line of work.

8.1 Achievements

Before the achievements of this thesis are discussed, it is important to outline again all the research contributions developed by other parties that served as a basis for this work:

- **Raw data format**: the GNSS data of each flight was preprocessed by DLR to have a MATLAB file format (Section 6.1.1).
- **AGDV model**: it was developed in [38][32] and allowed us to correct the AGDV error from the JAVAD AIRANT antenna (Section 6.2).
- σ_{mp} **model**: it was developed in [2] and it allowed us to normalize the 100-s smoothed multipath for the L1, E1, L5 and E5a bands (Section 2.5.2).
- **Overbounding theory**: the bounding criteria in the frequency domain was proven in [3][25] for high-integrity time-correlated error models (Section 3.2 and Section 3.3).

The following list includes all the achievements obtained as a result of this master thesis:

1) **Multipath error isolation**: in this work, we have presented a methodology to isolate the multipath error together with the thermal noise but excluding the receiver antenna error (Chapter 4). This methodology was then used to process flight data and extract the multipath error.

2) **$\boldsymbol{\sigma_{raw\ mp}}$ model**: combining the multipath error data extracted from all flights, we developed a standard deviation model of the raw multipath error for the GPS L1 and L5 bands and the Galileo E1 and E5a bands. This model ($\sigma_{raw\ mp}$) depends on the elevation of the satellite with respect to the aircraft in the NED frame (Section 5.3.2).

3) **Multipath error modeling**: all the raw multipath (L1, E1, L5 and E5a bands) was processed to also obtain the 100 seconds carrier-smooth multipath error. Subsequently, both the raw multipath and smoothed multipath were normalized with their respective standard deviation models ($\sigma_{raw\ mp}$ and σ_{mp}). Lastly, the ACF and PSD were computed for the continuous segments of all 16 multipath processing options from all flights (Chapter 5).

4) **Overbound model**: a model to overbound the airborne multipath error in the frequency domain was provided. This model is based on a FOGMP with an added constant level of white noise. The final parameter combination of the model for each multipath type is also presented in this work (Section 7.2).

8.2 Conclusions

For the first time and as a result of this thesis, the GNSS airborne code multipath error (and the thermal noise) was characterized using a high-integrity time-correlated error model. This model was derived from real test flights and includes the raw multipath and the 100-s smoothed multipath (unnormalized and normalized) for the GPS L1 and L5 band, as well as the Galileo E1 and E5a bands.

We hope that this work contributes to provide useful insight for future research and standardization efforts regarding dynamic error modeling using GNSS multi-constellation multi-frequency receivers for civil aviation, which promise to substitute current single-constellation single-frequency (GPS L1 band) receivers.

8.3 Future Work

There are several study aspects that were not included within the scope of this thesis due to time constrains. The following points highlight some potential directions to continue this work.

- **Implement the final models in a Kalman filter**: the final overbound models (σ^2, τ and white noise) can be implemented in a Kalman Filter, as shown in [5]. This would allow to verify the fidelity of the proposed dynamic model for multipath error and compare its performance with current models.

- **Assessment of the non-stationary effect on the overbound**: in theory, overbounding in the frequency domain only guarantees the overbound in the position domain if the error is a WSS process. Although the multipath error exhibits non-stationary traits, our experience points to the possibility that this non-stationarity is not severe enough to affect the validity of the multipath error overbound. Nevertheless, normalized multipath was also modeled in case this assumption is not true so as to minimize its non-stationary nature.

- **Different overbound model**: other overbounding models were experimented with during the development of this thesis. For instance, the sum of two different FOGMP promised to provide tighter bounding of the multipath error, especially when dealing with the L5 and E5a unsmoothed multipath. However, this also proved to be considerably more complex to implement.

- **Carrier-phase multipath models**: derive time-correlated models also for carrier-phase measurements.

Part V

Appendixes

A. Aircraft's Attitude

In flight dynamics, the attitude of an aircraft is described by three parameters: heading, pitch, and roll. These parameters represent the orientation of the aircraft through the rotation of its own axes, as it can be seen in Figure A.1.

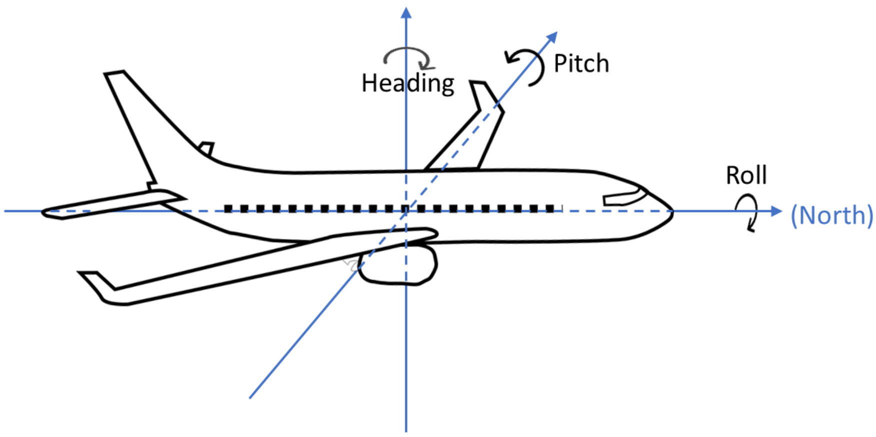

Figure A.1: Attitude parameters and their relation to the axes of the aircraft.

They can be described as follows:

- **Heading**: also referred to as yaw, it indicates the direction in which the aircraft's nose is pointing with respect to a reference point, usually expressed in degrees. It represents the horizontal angle between the aircraft's longitudinal axis (from the nose to the tail) and a reference direction, generally, true north. The heading can be easily measured with instruments such as a magnetic compass or an inertial navigation system.

- **Pitch**: it refers to the up-and-down rotation of the aircraft's longitudinal axis. It indicates the angle between the aircraft's longitudinal axis and the horizon. Positive pitch values indicate the nose is pointing above the horizon, while negative values indicate the nose is pointing below the horizon. Pitch mainly affects the aircraft's ability to climb or descent.
- **Roll**: also known as bank, it refers to the rotation of the aircraft around its longitudinal axis, causing one wing to move upward and the other wing to move downward. It indicates the angle between the aircraft's wings and the horizon. Positive roll values indicate the aircraft is banking to the right, while negative roll values indicate banking to the left. Roll is most prevalent when the aircraft is performing horizontal turns.

Because attitude parameters represent an angle of rotation, they are typically expressed in degrees. Table A.1 shows the valid ranges of these angles.

Attitude	
Heading	[0, 360°]
Pitch	[-90°, 90°]
Roll	[-90°, 90°]

Table A.1: Attitude parameters valid angle range.

B. Conclusiones y Propuestas Futuras

Este capítulo está dedicado a resumir los principales logros de este trabajo fin de máster y a presentar las conclusiones principales derivadas de los resultados obtenidos. Finalmente, la última sección ofrece propuestas futuras posibles para continuar con esta línea de trabajo.

B.1 Logros

Antes de exponer los logros de esta tesis, es importante destacar de nuevo todas las contribuciones de investigación desarrolladas por otras personas y que han servido como base de este trabajo:

- **Formato de los datos originales**: los datos GNSS de cada vuelo fueron preprocesados por DLR para que tuvieran un formato de archivo MATLAB (Sección 6.1.1).
- **Modelo del AGDV**: fue desarrollado en [38][32] y nos permitió corregir el error asociado al AGDV de la antena JAVAD AIRANT (Sección 6.2).
- **Modelo de σ_{mp}**: fue desarrollado en [2] e hizo posible que normalizaramos el error multicamino suavizado 100 segundos para las bandas L1, E1, L5 and E5a (Sección 2.5.2).
- **Teoría de delimitación**: el criterio de delimitación en el dominio de la frecuencia fue demostrado en [3][25] para modelos de error de alta integridad correlacionados en el tiempo (Sección 3.2 y Sección 3.3).

La siguiente lista incluye todos los logros conseguidos como resultados de este trabajo:

1) **Aislamiento del error multicamino**: en este trabajo, hemos presentado una metodología para aislar el error multicamino junto con el ruido térmico pero excluyendo el error asociado a la antena del receptor (Capítulo 4). Esta metodología se utilizó posteriormente para procesar los datos de vuelo y extraer el error multicamino.

2) **Modelo de $\boldsymbol{\sigma_{raw\ mp}}$**: combinando los datos del error multicamino extraídos de todos los vuelos, desarrollamos un modelo de desviación estándar del error multicamino sin suavizar para las bandas L1 y L5 de GPS y las bandas E1 y E5a de Galielo. Dicho modelo ($\sigma_{raw\ mp}$) depende de la elevación del satélite con respecto a la aeronave en el sistema de coordenadas NED (Sección 5.3.2).

3) **Modelado del error multicamino**: se procesó todo el error multicamino resultante (bandas L1, E1, L5 y E5a) para obtener también el error de multicamino con suavizado de 100 segundos. A continuación, tanto el multicamino sin suavizar como el multicamino suavizado se normalizaron con sus respectivos modelos de desviación típica ($\sigma_{raw\ mp}$ y σ_{mp}). Por último, se calcularon la función de autocorrelación y la densidad espectral de potencia para los segmentos continuos de las 16 opciones de procesamiento del error multicamino de todos los vuelos (Capítulo 5).

4) **Modelo de delimitación**: se presentó un modelo para delimitar el error multicamino aéreo en el dominio de la frecuencia. Este modelo se basa en un Proceso Gauss Markov de Primer Orden con un nivel constante de ruido blanco añadido. La combinación final de parámetros del modelo para cada tipo de multicamino también se presenta en este trabajo (Sección 7.2).

B.2 Conclusiones

Por primera vez y como resultado de este trabajo, se ha caracterizado el error multicamino aéreo del código de GNSS (y el ruido térmico) utilizando un modelo de error de alta integridad correlacionado en el tiempo. Este modelo se obtuvo a partir de vuelos de prueba reales e incluye el multicamino sin suavizar y suavizado de 100 s (sin normalizar y normalizado) para las bandas L1 y L5 de GPS, así como para las bandas E1 y E5a de Galileo.

Esperamos que este trabajo contribuya a proporcionar una perspectiva útil para futuros esfuerzos de investigación y estandarización relacionados con el modelado dinámico de errores utilizando receptores GNSS multiconstelación multifrecuencia para aviación civil, los cuales prometen sustituir a los receptores monofrecuencia de una sola constelación actuales (banda L1 de GPS).

B.3 Líneas Futuras

Hay varios aspectos del estudio que no se pudieron incluir en el alcance de este trabajo debido a las limitaciones de tiempo. Los siguientes puntos destacan algunas líneas futuras posibles para continuar este trabajo.

- **Implementación de los modelos finales en un filtro de Kalman**: los modelos de delimitación finales (σ^2, τ y ruido blanco) pueden implementarse en un filtro de Kalman, como se muestra en [5]. Esto permitiría verificar la fidelidad del modelo dinámico propuesto para el error multicamino y comparar su funcionamiento con los modelos actuales.
- **Evaluación del efecto de no-estacionariedad en la delimitación**: en teoría, la delimitación en el dominio de la frecuencia sólo garantiza la delimitación en el dominio de la posición si el error es un proceso estacionario en sentido amplio. Aunque el error multicamino presenta rasgos no estacionarios, nuestra experiencia apunta a la posibilidad de que dicha no-estacionariedad no sea lo suficientemente grave como para afectar a la validez de la delimitación del error multicamino. No obstante, también se modeló el multicamino normalizado en caso de que esta suposición no fuera cierta, con el fin de minimizar su naturaleza no-estacionaria.
- **Modelo de delimitación diferente**: durante el desarrollo de este trabajo se experimentó con otros modelos de delimitación. Por ejemplo, la suma de dos Procesos Gauss Markov de Primer Orden diferentes prometía proporcionar una delimitación más ajustada del error multicamino, especialmente en el caso del multicamino no suavizado de las bandas L5 y E5a. No obstante, también resultó ser considerablemente más complejo de implementar.
- **Modelar el error de multicamino de la portadora**: obtener modelos de error correlados en el tiempo también para medidas de la portadora GNSS.

Bibliography

[1] "Minimum Operational Performance Standards (MOPS) for GNSS Aided Inertial Systems". DO-384. RTCA, 2020.

[2] Mihaela-Simona Cîrciu. *"Integrity Aspects for Dual-Frequency Dual-Constellation Ground Based Augmentation System (GBAS)"*. Phd thesis, RWTH Aachen University, 2020.

[3] E. Gallon, M. Joerger, and B. Pervan. "Robust Modeling of GNSS Tropospheric Delay Dynamics". *IEEE Transactions on Aerospace and Electronic Systems*, 57(5):2992–3003, 2021.

[4] E. Gallon, M. Joerger, and B. Pervan. "Robust Modeling of GNSS Orbit and Clock Error Dynamics". *NAVIGATION: Journal of the Institute of Navigation*, 69(4), 2022.

[5] S. Langel, O. García Crespillo, and M. Joerger. "A New Approach for Modeling Correlated Gaussian Errors Using Frequency Domain Overbounding". In *2020 IEEE/ION Position, Location and Navigation Symposium (PLANS)*, pages 868–876, 2020.

[6] P. Teunissen and O. Montenbruck. *"Springer Handbook of Global Navigation Satellite Systems"*. Springer International Publishing, 2017.

[7] J. Avila-Rodríguez, G. Hein, S. Wallner, J.Issler, L. Ries, L. Lestarquit, A. DeLatour, J. Godet, F. Bastide, T. Pratt, and J. Owen. "The MBOC Modulation: The Final Touch to the Galileo Frequency and Signal Plan". *Navigation*, 55(1):15–28, 2008.

[8] E. Lohan, H. Hurskainen, and J. Nurmi. *"GALILEO Positioning Technology"*. Springer Netherlands, 2014.

[9] J. Sanz Subirana, J. M. Juan Zornoza, and M. Hernández-Pajares. *"GNSS Data Processing"*, volume I: Fundamentals and Algorithms. ESA Communications, 2013.

[10] J. Avila-Rodríguez, S. Wallner, G. Hein, E. Rebeyrol, O. Julien, C. Macabiau, L. Ries, A. DeLatour, L. Lestarquit, and J. Issler. “CBOC- an implementation of MBOC". *Proceedings of 1rst CNES-ESA Workshop on Galileo Signals and Signal Processing*, 2006.

[11] M.-S. Circiu, S. Caizzone, M. Felux, C. Enneking, M. Rippl, and M. Meurer. “Development of the dual-frequency dual-constellation airborne multipath models". *NAVIGATION*, 67(1):61–81, 2020.

[12] R. Hatch. “The synergism of GPS code and carrier measurements". volume 2, pages 1213–1231. Proceedings of the 3rd International Geodetic Symposium on Satellite Doppler Positioning DMA/NOS, 1983.

[13] “Minimum Operational Performance Standards for Global Positioning System/Satellite-Based Augmentation System Airborne Equipment". DO-229E. RTCA, 2016.

[14] “Minimum Operational Performance Standards for GPS Local Area Augmentation System Airborne Equipment". DO-253D. RTCA, 2017.

[15] Omar García Crespillo. *“GNSS/INS Kalman Filter Integrity Monitoring with Uncertain Time Correlated Error Processes”*. PhD thesis, École Polytechnique Fédérale de Lausanne (EPFL), 2022.

[16] James D. Hamilton. *“Time series analysis"*. Princeton Univ. Press, 1994. Description based on publisher supplied metadata and other sources.

[17] S. M. Kay and S. L. Marple. “Spectrum analysis - A modern perspective". *Proceedings of the IEEE*, 69(11):1380–1419, 1981.

[18] M. S. Bartlett and J. Medhi. “On the Efficiency of Procedures for Smoothing Periodograms from Time Series with Continuous Spectra". *Biometrika*, 42:143, 1955.

[19] P. Welch. “The use of fast Fourier transform for the estimation of power spectra: A method based on time averaging over short, modified periodograms". *IEEE*, 15(2):70–73, 1967.

[20] Douglas Lyon. “The Discrete Fourier Transform, Part 4: Spectral Leakage". *The Journal of Object Technology*, 8(7):23, 2009.

[21] Chris A. Mack. “More systematic errors in the measurement of power spectral density”. *Micro/Nanolithography, MEMS, and MOEMS*, 14(3), 2015.

[22] B. DeCleene. “Defining Pseudorange Integrity - Overbounding". *Proceedings of the 13th International Technical Meeting of the Satellite Division of The Institute of Navigation (ION GPS 2000)*, pages 1916–1924, 2000.

[23] R. E. Kalman. “A New Approach to Linear Filtering and Prediction Problems". *Journal of Basic Engineering*, 82(1):35–45, 1960.

[24] O. García Crespillo, S. Langel, and M. Joerger. “Tight Bounds for Uncertain Time-Correlated Errors With Gauss–Markov Structure in Kalman Filtering". *IEEE Transactions on Aerospace and Electronic Systems*, 59(4):4347–4362, 2023.

[25] S. Langel, O. García Crespillo, and M. Joerger. “Overbounding the effect of uncertain Gauss-Markov noise in Kalman filtering". *NAVIGATION*, 68(2):259–276, 2021.

[26] R. G. Brown and P. Y. Hwang. *“Introduction to random signals and applied kalman filtering"*, volume 3. Wiley New York, 4th edition, 2012.

[27] N. Jeremy Kasdin. “Discrete Simulation of Colored Noise and Stochastic Processes and $1/f^{\alpha}$ Power Law Noise Generation". *Proceedings of the IEEE*, 83(5):802–827, 1995.

[28] M. Joerger, S. Jada, S. Langel, O. García Crespillo, E. Gallon, and B. Pervan. “Practical Considerations in PSD Upper Bounding of Experimental Data". *ION GNSS+*, 2023.

[29] M.-S. Circiu, S. Caizzone, M. Felux, C. Enneking, and M. Meurer. “Improved Airborne Multipath Modelling”. In *Proceedings of the 31st International Technical Meeting of The Satellite Division of the Institute of Navigation (ION GNSS+ 2018)*, pages 2195–2209. Institute of Navigation, 2018.

[30] Michael S. Brash. “Isolation of GPS Multipath and Receiver Tracking Errors”. *NAVIGATION*, 41(4):415–434, 1994.

[31] L. Wanninger, H. DUmaya, and S. Beer. “Group delay variations of GPS transmitting and receiving antennas". *Journal of Geodesy*, 91(9):1099–1116, 2017.

[32] S. Caizzone, M.-S. Circiu, W. Elmarissi, C. Enneking, M. Felux, and K. Yinusa. “Antenna influence on Global Navigation Satellite System pseudorange performance for future aeronautics multifrequency standardization”. *NAVIGATION*, 66(99–116), 2019.

[33] Paul Groves. *“Principles of GNSS, Inertial, and Multisensor Integrated Navigation Systems"*. Second edition, 2013.

[34] B. Park, K. Sohn, and C. Kee. “Optimal Hatch Filter with an Adaptive Smoothing Window Width". *Journal of Navigation*, 61(3):435–454, 2008.

[35] V. Wullschleger. “FAA Performance Type 1 LAAS Specification: Performance, Operations, and ATC Requirements". *Proceedings of the 2000 National Technical Meeting of The Institute of Navigation*, pages 194–199, 2000.

[36] “Minimum Operational Performance Specification for Global Navigation Satellite Ground Based Augmentation System Ground Equipment to Support Category I Operations". ED-114A. Eurocae, 2013.

[37] O. García Crespillo, M. Joerger, and S. Langel. “Overbounding GNSS/INS Integration with Uncertain GNSS Gauss-Markov Error Parameters. In *2020 IEEE/ION Position, Location and Navigation Symposium (PLANS)*, pages 481–489, 2020.

[38] S. Caizzone, M.-S. Circiu, W. Elmarissi, C. Enneking, M. Felux, and K. Yinusa. “Effect of Antenna Pattern Uniformity on the Pseudorange Tracking Error". 2017.

[39] D. Prochniewicz and M. Grzymala. “Analysis of the Impact of Multipath on Galileo System Measurements”. *Remote Sensing*, 13(12):2295, 2021.